Experimental Study on Wall Heat Transfer of Diesel Spray Flame in Two-Dimensional Combustion Chamber Operated with Rapid Compression and Expansion Machine

(急速圧縮膨張装置を用いた二次元燃焼室内ディーゼル噴霧火炎の壁面熱伝達に関する実験的研究)

HERRY SUFYAN HADI

Mechanical Engineering Program

Graduate School of Advance Science and Engineering

Hiroshima University

September 2024

Experimental Study on Wall Heat Transfer of Diesel Spray Flame in Two-Dimensional Combustion Chamber Operated with Rapid Compression and Expansion Machine

(急速圧縮膨張装置を用いた二次元燃焼室内ディーゼル噴霧火炎の壁面熱伝達に関する実験的研究)

by

HERRY SUFYAN HADI

Dissertation

Submitted to the Graduate School of Advanced Science and Engineering

Hiroshima University

In Partial Fulfillment of the Requirements

For the Degree of

Doctor of Engineering

Hiroshima University

September 2024

ABSTRACT

Reducing heat transfer during the spray combustion of diesel engines remains a challenging task. The thermal efficiency can be enhanced by minimizing heat transfer in the combustion chamber. Increasing common rail pressure can improve lean mixture formation before combustion. Additionally, a lean mixture can be achieved using a split injection strategy.

This study investigated the effect of number of holes injector on spray flame behavior, wall heat flux, soot emissions, and heat transfer phenomena of diesel engines at varying common rail pressures. A rapid compression and expansion machine (RCEM) was employed to simulate a single cycle of diesel spray combustion using split injection sprays. The two-dimensional (2D) stepped piston cavity is a uniquely shaped model used to describe the spray flame behavior in the combustion chamber. To investigate the heat transfer phenomena, a local wall heat flux sensor was installed in the cylinder (head and liner) and piston cavity (upper lip, lip, and bottom) to measure the heat flux distribution, and a diffused backlight illumination method was used to visualize the spray and flame behavior in the combustion chamber and 2D piston cavity.

The results indicated that, for both two-hole and six-hole injectors, the impingement flame surrounding the cylinder head contributed to the highest magnitude and longest duration of heat flux on the cylinder side due to the spray flame velocity, impingement, and residence time. Additionally, the higher temperature difference at the cavity bottom resulted in greater heat flux on the cavity side compared to the squish side. Higher injection pressure increased spray momentum and spray tip penetration, which led to a better air-fuel mixture, improved evaporation rate, and reduced flame residence time, thereby decreasing accumulated heat loss in the combustion chamber. Furthermore, lower common rail pressure induced a greater difference in the accumulated heat flux ratio than higher common rail pressure, attributed to the longer flame residence time in the combustion chamber. The results also showed that higher common rail pressures reduced combustion duration and soot emissions. Higher common rail pressure increased spray velocity, enhancing turbulence levels and resulting in higher peak values of wall heat flux. The highest peak value of wall heat flux was observed at the cylinder head due to the

intense combustion region, followed by the cavity bottom due to the highest flame temperature occurring around this location. Additionally, the effect of the number of injector holes was examined in this study. The findings revealed that luminous flame appeared only at the cavity side wall with a two-hole injector, while with a six-hole injector, it was observed at the cavity side wall and near the injector holes. In the main result, common rail pressures 125 MPa and 120 MPa becomes the optimum for reducing the heat transfer which contributes to the increase the thermal efficiency for two-holes and six-holes injector, respectively. Moreover, the heat transfer phenomena in diesel engines were effectively represented by local $Nu - Re$ correlations to confirm the heat transfer phenomena in diesel combustion chamber using RCEM. These results contribute to the increase the thermal efficiency of diesel combustion engines.

TABLE OF CONTENTS

NOMENCLATURES

1D	One-Dimensional
2D	Two-Dimensional
AHRR	Apparent Heat Release Rate
APV	Average Pixel Value
ASOI	After Start of Injection
ATDC	After Top Dead Center
ATPR	After Trigger Pulse Rising
Cav Upper Lip	Cavity Upper Lip
Cav Lip	Cavity Lip
Cav Bottom	Cavity Bottom
CFD	Computational Fluid Dynamic
CI	Compression Ignition
C_p	Specific heat
CVCC	Constant Combustion Volume Chamber
Cyl Head	Cylinder Head
Cyl Liner	Cyliner Liner
DBI	Diffused Backlight Illumination
DP	Direct Photography
HCCI	Homogeneous Charge Compression Ignition
ICEs	Internal Combustion Engines
fps	Frames per second
KL factor	Knudsen-Langmuir factor
LAS	Laser absorption-scattering
NDV	Non-Dimensional Pixel Value

NFL	Natural Flame Luminosity
N_2	Nitrogen
NO	Nitrogen Oxide
NOx	Nitrogen Oxides
Nu	Nusselt Number
O_2	Oxygen
PCCI	Premixed Charge Compression Ignition
PIV	Particle Image Velocimetry
P_r	Prandtl
Pre-	Preceding
RCEM	Rapid Compression and Expansion Machine
RCM	Rapid Compression Machine
Re	Reynolds Number
RGB	Red Green Blue
TDC	Top Dead Center

CHAPTER 1 INTRODUCTION

1.1 BACKGROUND AND MOTIVATIONS

Nowadays, fossil fuels continue to be the world's primary energy source. Despite the discovery of numerous renewable alternatives, fossil fuels remain the most frequently used energy source, particularly for meeting living standards. As illustrated in Figure 1.1, oil and gas are anticipated to continue supplying more than half of the world's energy needs. By 2040, oil demand is expected to increase by 20%. [1]. The largest user of oil is the transportation sector. It is anticipated that oil use will decrease with the introduction of electric vehicles. In the interim, oil is expected to be used for heavy-duty transportation, including trucks, cargo ships, and other large equipment vehicles. If electric vehicles are widely adopted by 2035, oil demand in 2050 is still predicted to be 85 million barrels per day, the same as in 2010 [2].

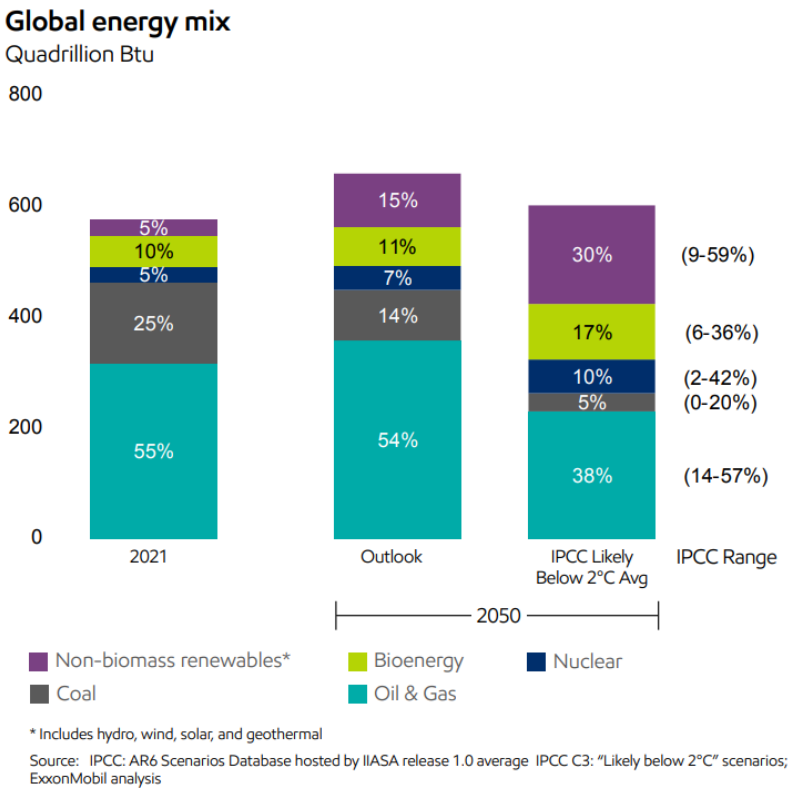

Figure 1.1 All energy types needed to obtain the living standards [2].

Over the past 20 years, global car ownership has increased by over 600 million vehicles, and road transport services have seen a nearly 65% rise. Additionally, compared to all other sectors combined, the road transport industry uses the most oil, accounting for around 45% of global oil consumption. The petrochemical industry is the second-largest user, accounting for 15% of oil consumption [3]. Although many private internal combustion engines (ICEs) cars are expected to transition to electric vehicles in the future, large vehicles such as diesel passenger vehicles and trucks are predicted to continue using oil, as depicted in Figure 1.2. In conclusion, diesel engine vehicles persist due to their economical fuel usage [4] [5] [6].

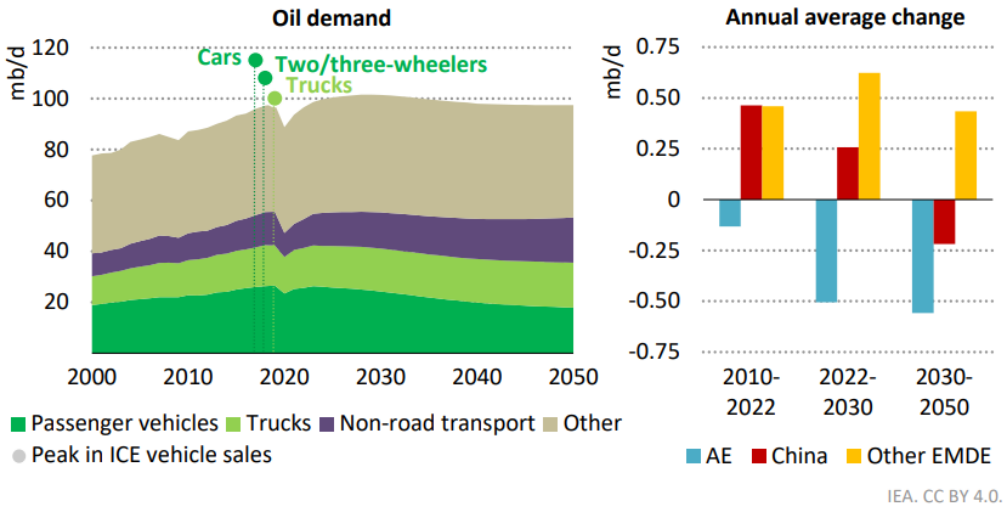

Sales of gasoline and diesel passenger vehicles and trucks have already peaked, leading to a peak in oil demand before 2030

Note: mb/d = million barrels per day; AE = advanced economies; EMDE = emerging market and developing economies.

Figure 1.2 An analysis of global oil demand by sector and the annual average change by region from 2000 to 2050 [3].

Due to their excellent performance, high efficiency, and cost-effectiveness, diesel engines are widely used in various industries, including transportation, heavy industry, power generation, and maritime [7] [8] [9] [10] [11]. It used fuel combustion to obtain the mechanical energy. In diesel engine, the heat balance refers to the distribution of

energy generated from the combustion of fuel. When diesel fuel combusts in the combustion chamber, the energy released is divided into several components. The heat balance is an essential tool for evaluating the efficiency of the engine and identifying areas where energy losses occur. It helps in understanding how much of the fuel's energy is converted into useful work and how much is dissipated in other forms [12].

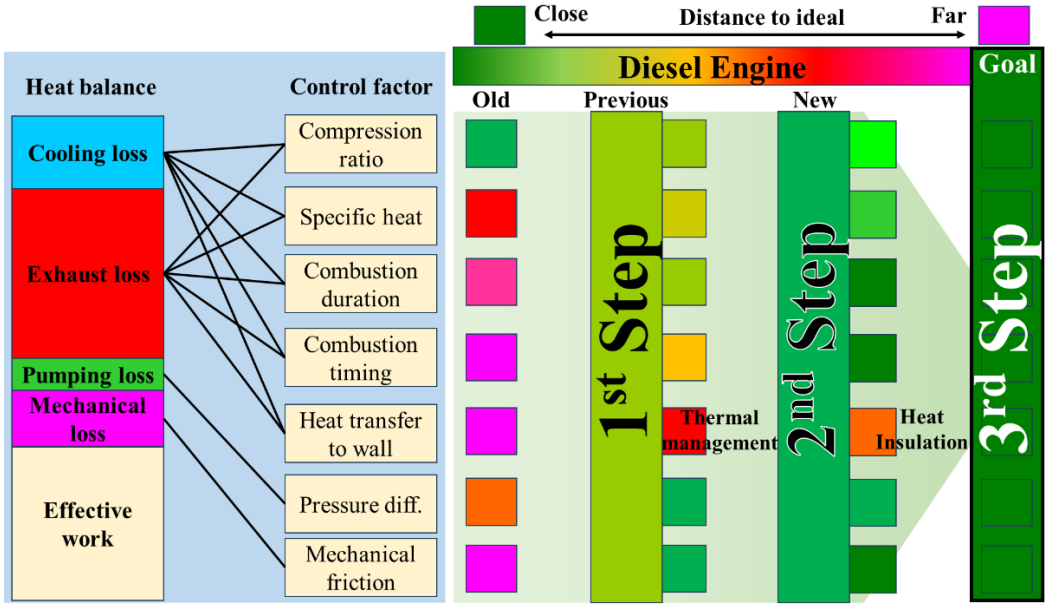

Figure 1.3 Enhancing thermal efficiency for ideal diesel engines.

The energy intake from the fuel serves as the foundation for the heat balance. Diesel fuel burns with high energy density, producing a substantial amount of thermal energy. The total energy input is commonly calculated using the calorific value of the fuel, which represents the quantity of heat generated during complete combustion. In the combustion chamber, the fuel-air mixture burns, creating high-temperature and high-pressure conditions that drive the piston. This energy is harnessed within the chamber. The heat balance of a diesel engine provides a thorough understanding of how fuel energy is distributed inside the engine. By examining various channels for energy dissipation and transformation, technicians can identify opportunities to improve engine effectiveness and efficiency. Technological breakthroughs and a deeper understanding of heat transfer

have driven the continuous evolution of the diesel engine, making it more efficient and environmentally friendly. The heat balance: cooling loss, exhaust loss, pumping loss, mechanical loss, and effective work should be enhanced to optimize the efficiency [13]. Here, we can control compression ratio, specific heat ratio, combustion duration, combustion timing, heat transfer to wall, pressure differential, and mechanical friction.

In this study, we investigate the heat transfer to the wall to improve thermal efficiency in diesel spray combustion, as shown in Figure 1.3. The enhancing the thermal efficiency is obtained by reducing the heat transfer. One solution to reduce heat transfer is by increasing common rail pressure and using multiple injection strategy to enhance the formation of a lean mixture [14]. Nishida and co-workers [15] discussed the effect of common rail pressure on improving efficiency. Using image processing and measurements, this study examined combustion flames, wall interactions, and high-temperature ignition. It was discovered that common rail pressure had minimal effect on the injection delay; nevertheless, high common rail pressure increased the maximum in-cylinder pressure and apparent heat release rate while also improving spray stability. Furthermore, increasing the common rail pressure to 300 MPa resulted in a considerable decrease in soot formation. The longer combustion and ignition delays were reduced by the rising high injection pressure, which also shortened the flame residence time. Meanwhile, the apparent heat release rate and maximum in-cylinder pressure decreased as engine speed increased [16]. Additional studies have demonstrated that increasing the common rail pressure at higher fuel mass flow rates can decrease the flame area, natural flame luminance, and ignition delay [24]. Higher injection pressure also results in a decrease in the adhesion residence time of liquid fuel, which increases the vaporization ratio.

Large variants of direct injection engines and the development of engines with increased efficiency have been the focus of advanced research on various common rail pressure schemes. In one study, this technique worked well to reduce the engine's exhaust pollutants [17]. "The results demonstrated reduced pollutant emissions, an enhanced heat release rate, improved thermal efficiency, higher knock limits, sustained torque, and combustion stability. Subsequently, split diesel injection was employed to achieve maximum thermal efficiency and reduce emissions by as much as 12%, a reduction superior to that achieved by previous diesel engines using the split injection strategy [18]. The study demonstrated that a split injection of 3.4% at 30ms after the start of injection (ASOI) reduced the ratio of adhered mass under non-evaporation conditions. It investigated how split injection influenced fuel adhesion properties in scenarios involving both evaporation and non-evaporation [19]. “Splashing” and “suction” were used to establish this condition. The ambient gases induced stronger wall adhesion despite the split injection method promoting evaporation, thereby limiting the time available for fuel adhesion to transfer heat to the hot wall. Additionally, generalized flameless equations were employed to identify the various combustion modes involved in the ignition process [20]. The results indicated that the process of generating the fuel-air mixture is crucial for the interactions during ignition development but insignificant during the auto-ignition process. In other words, the study demonstrated that thermal efficiency can be enhanced through multiple injections. Furthermore, variations in common rail pressure were utilized to investigate heat transfer to the wall, aiming to optimize thermal efficiency in diesel spray combustion.

1.2 OBJECTIVES AND APPROACHES

This study aims to elucidate heat transfer phenomena to the wall under diesel engine-

like conditions using a rapid compression and expansion machine. It examines the influence of common rail pressure on spray flame behavior and wall heat transfer through a triple injection strategy. The primary goals of this investigation are as follows:

1. Clarify the effect of early pilot injection using a triple injection strategy on spray and flame behavior, as well as wall heat transfer under baseline conditions.
2. Investigate the effect of common rail pressure on main combustion flame, wall heat flux, accumulated wall heat flux, and the total accumulated wall heat fluxes.
3. Observe the effect of a two-hole injector on spray flame behavior in relation to wall heat flux.
4. Analyze the effect of a six-hole injector on spray flame near the injector and cavity wall, correlated with wall heat flux.
5. Investigate characteristic length, characteristic velocity, and flame temperature to determine Nusselt and Reynolds numbers.
6. Study heat transfer phenomena during the combustion process using Nusselt and Reynolds number correlations.
7. Confirm the Nusselt and Reynolds number correlations through comparison with other research studies.

Furthermore, we employed a two-dimensional piston cavity specifically designed for the Mazda Skyactiv-D engine [21] [22] [23]. To simulate single-cycle diesel engines, we utilized a rapid compression and expansion mechanism. High-speed video cameras captured spray/wall interactions, air-fuel mixture formation, and flame propagation by recording spray and flame behavior within the combustion chamber. Spray/vapor development, spray wall impingement, autoignition, and flame development were visualized using diffused backlight illumination techniques. Concurrently, flame

development and distribution in the combustion chamber were examined through direct photography without additional lighting. Additionally, two-color pyrometry analysis was employed to determine flame temperature and the KL factor. Essential data on wall heat flux were gathered using sensors mounted on the cylinder side and cavity. Furthermore, in-cylinder pressure was measured using a pressure transducer, while piston movement was tracked with a laser sensor. The accumulator was connected to the compressor to achieve the target engine speed of 525 rpm. This procedure was repeated to confirm the engine speed target under different conditions.

1.3 OUTLINES

To present this work, the dissertation is organized as follows: a review of the previous study on improving the diesel engine utilization, improving the engine performance, and the effort to enhance the thermal efficiency are discussed in Chapter 1. Detailed of the experimental apparatus of rapid compression and expansion machine using two-dimensional (2D) combustion chamber, wall heat flux sensor locations, optical arrangement of diffused backlight illumination, detailed of wall heat flux sensor, and experimental condition are presented in Chapter 2. Chapter 3 describes the correlation between wall heat flux characteristics and spray flame behavior under baseline common rail pressure. In addition, the accumulated wall heat flux and sum of accumulated wall heat flux distribution are also presented in this chapter. Chapter 4 shows the effect of common rail pressure on wall heat flus characteristics, spray flame behavior, and two-color pyrometry results. Also, the spray flame image processing method is described to investigate the luminous flame distribution in the combustion chamber. Chapter 5 discusses the effect of number of holes injector on wall heat flux characteristic, spray flame behavior, two-color pyrometry results, direct photography, injection rate result, and

spray flame tip penetration result. The wall heat transfer phenomenon in the combustion chamber is presented in chapter 6 using Nusselt and Reynolds number analyses. The local characteristic length, characteristic velocity, and flame temperature were also discussed in this chapter. In addition, we compared our result of Nusselt and Reynolds number to the other researchers. Chapter 7 concludes with a summary of the general findings on spray flame behavior using two-holes and six-holes injectors, analysis of Nusselt and Reynolds numbers, and suggestions for future research.

1.4 REVIEW OF PREVIOUS WORKS

1.4.1 Heat Transfer in Diesel Combustion Chamber

Heat transfer of diesel combustion engine is the main factor of energy losses which reduce the thermal efficiency. Thermal efficiency is a critical parameter in diesel combustion chambers, directly influencing the overall performance, fuel economy, and emissions of diesel engines [24]. It reflects the engine's ability to convert the chemical energy of diesel fuel into useful mechanical work. Enhancing thermal efficiency in diesel combustion chambers is a multifaceted challenge, involving the optimization of fuel injection, combustion processes, heat transfer, and engine design [25].

Figure 1.5 shows the process of heat transfer high temperature gas inside the cylinder to through the combustion chamber wall and coolant. Temperature profile of hot gas (T_g), mean gas temperature $(\overline{T_g})$, cooling temperature (T_c), and mean cooling temperature $(\overline{T_c})$ are presented. Also, surface wall temperature of hot gas $(T_{w,g})$, surface wall temperature of cooling oil (T_2), and cooling oil temperature $(T_{w,c})$ are discussed. The convection $(\dot{q}_{CV})$ and radiation $(\dot{q}_R)$ heat transfer occurs within the cylinder where the conduction heat transfer applies in the chamber wall. Then, the convection heat transfer flows in the coolant. The convection and radiation heat transfer in the combustion

chamber gives rise to a wall heat flux that is transferred into the cooler [26]. Furthermore, the heat transfer which through piston wall was more than cylinder head and block wall [27].

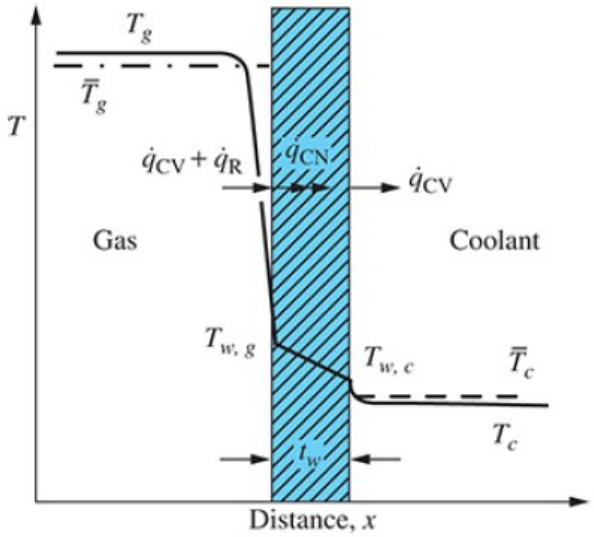

Figure 1.5 Schematic of heat flow and temperature distribution process across the combustion chamber wall [26].

1.4.2 Free Spray Flame Combustion Development

Figure 1.4 shows the processes of ignition, soot formation, and oxidation in diesel spray combustion. In the ignition process, ignition occurs when the mixture reaches a critical state, leading to spontaneous combustion initiated by the presence of reactive species like formaldehyde and hydroxyl radicals. This rapid combustion generates a high-pressure explosion that drives the piston down, converting chemical energy into mechanical work. Soot formation begins in fuel-rich areas but is countered by oxidation processes that break down soot particles. The combustion cycle completes with the expulsion of exhaust gases, preparing the engine for the next intake of air and fuel injection [28] [29]. Ultra-high injection pressure significantly reduced soot formation

with the conventional nozzle, while the micro-hole nozzle led to very minimal or undetectable soot at higher pressures. Impinging spray flames with the micro-hole nozzle were smaller and had lower soot formation. Comparatively, flat wall impingement increased soot formation with the conventional nozzle, but not with the micro-hole nozzle. Liquid length differences contributed to the varying soot levels between impinging and free spray flames [30] [31] [32].

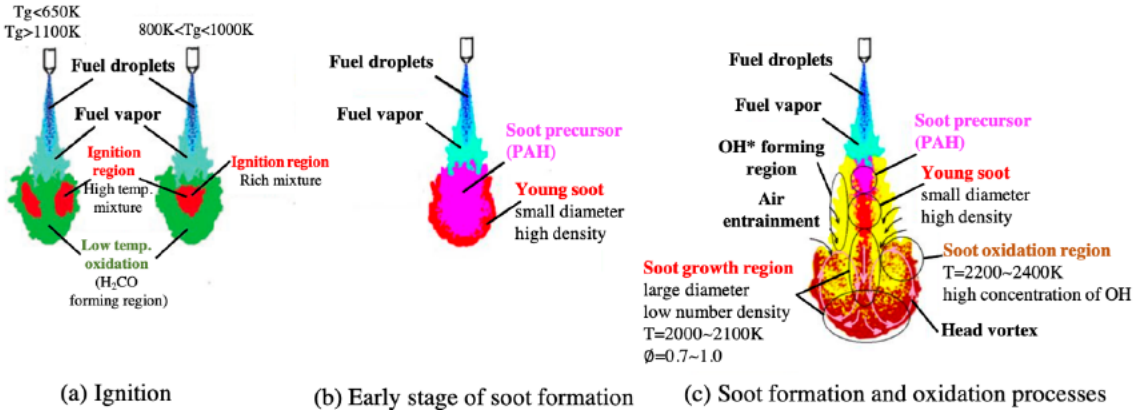

Figure 1.4 Schematic diagram of ignition, soot formation, and oxidation processes in diesel spray combustion [33].

1.4.3 Optical Diagnostic Technique for Analyzing Impinging Diesel Spray

In other studies, the ignition process was examined using a rapid compression and expansion machine [34] [35] [36] [37]. The experiment was conducted using two modes of ignition governed by the temperature of the surface and depth of the heating element as the input, at a common rail pressure 40 MPa [38]. The optimal position was obtained when the tip of the heating element was set up on the surrounding liquid spray in the vapor cone. The results, based on these configurations, indicated that the critical temperature on the surface was approximately 1250 K, and short ignition delays were consistently achieved using the spray ignition mode. Limited researchers presented experimental imaging of spray and flame behavior in diesel engine. Yang et. al [39]

investigated effect of increasing injection pressure and splitting the injection stage using 2D piston cavity, as shown in Figure 1.6. It discussed spray and flame behavior in diesel engine by using LAS technique to observe spray mixture formation. Next study, it used constant volume split injection strategy under common rail pressure 100 and 160 MPa. The result showed that the interaction between the spray and the wall in a 2D cavity leads to reduced spray tip penetration and a lower evaporation rate. Pre-injection combustion enhances the effectiveness of the main injection. Split injection can decrease soot formation and speed up its oxidation. Extending the interval between split injections is an effective approach to further reduce soot. Other researchers used 2D piston cavity in vertically which spray flowed to the bowl and squish regions. The play role of vertical vortex enhances the mixture formation which promotes the combustion [40] [41] [42]. In the previous study, the flame characteristics of wall-impinging diesel fuel spray, under both single and split injection strategies, were studied in a high-temperature, high-pressure constant volume combustion vessel [23]. A 2D piston cavity was utilized to form the impingement spray flame, and the two-color method was employed to analyze the flame process. The result suggested that the ignition position is further away for single injections compared to split injections. The second ignition delay is defined within specific ranges of first injection proportions from 25% to 75%. A 50% first injection proportion creates two optimal ignition areas, while 75% is most favorable for ignition. The initial flame temperature changes slightly and decreases earlier at 50% proportion, with minimal interaction between the first and second injections at this proportion. Regardless of whether split or single injections are used, the ratio of high-temperature areas shows multiple peaks. Single injections experience an earlier decline in temperature. In single injections, the KL factor and range of flame temperatures are smaller compared to split injections. Soot formation is strongly linked to the ratio of high-temperature areas

rather than the total flame area. As the proportion of the first injection increases in split injections, the total flame area decreases.

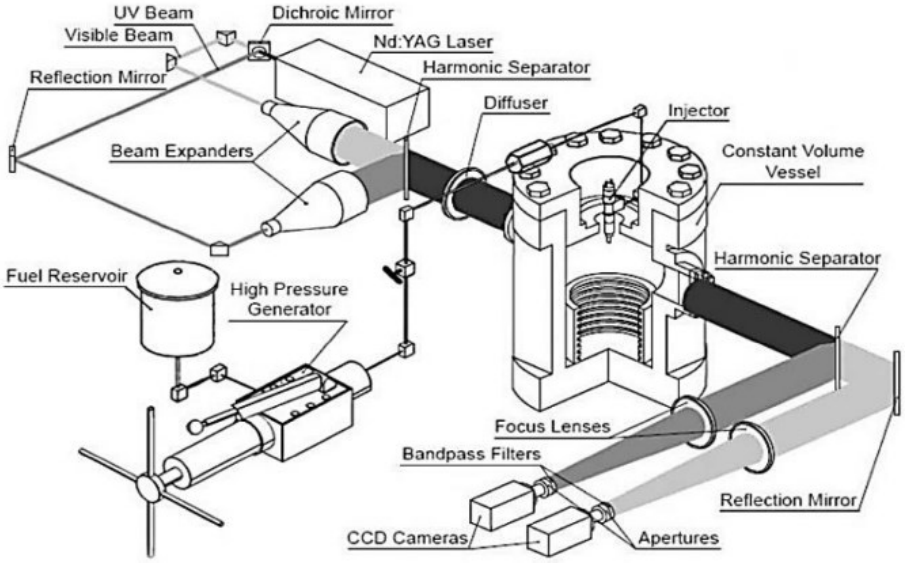

(a) Schematic of LAS method

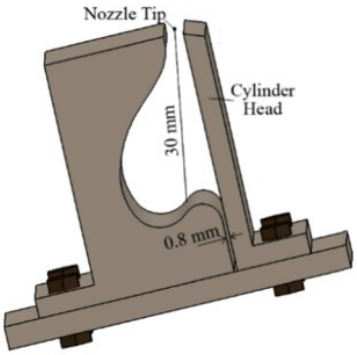

(b) Model of 2D piston cavity

Figure 1.6 Experimental apparatus of 2D piston cavity impinging [21] [22] [23] [39].

Other researchers, Fan et. al [43] investigated diesel spray combustion using 2D piston cavity in rapid compression and expansion machine. The experimental apparatus was shown in Figure 1.7. The study examined how spray and wall interaction in a rapid compression and expansion machine affects mixture formation, ignition location, and soot generation. The research was conducted with a common rail pressure 120 MPa under both single and split injection strategies, in an environment with 15% oxygen

concentration. A shadow method was employed to observe the interaction between the fuel spray and the piston cavity, while natural flame luminosity was captured by a high-speed color video camera to study the impinging spray and combustion process. The findings revealed that split injection strategies softened the heat release profile and facilitated the onset of main combustion. The camera captured cool-flame phenomena, and intense ignition occurred when the pilot spray impinged on the lower lip of the piston rim. Extending the mixing process of the pilot spray was shown to promote a homogeneous mixture, aiding low-temperature combustion and reducing soot generation. This research offers a detailed investigation into the spray and combustion process, emphasizing the significant impact of spray and wall interaction on subsequent combustion stages.

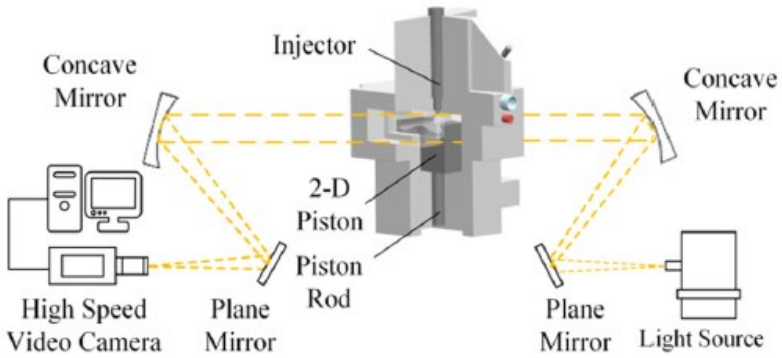

(a) Shadow optical arrangements

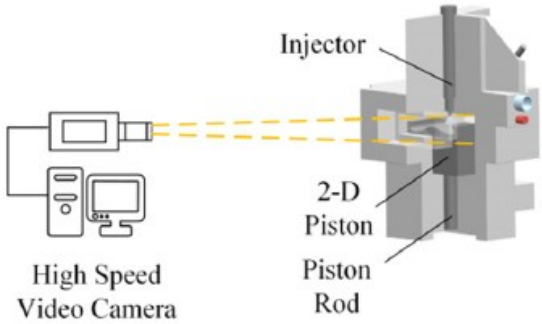

(b) Natural luminescence optical arrangement

Figure 1.7 Schematic of experimental apparatus using two-dimensional combustion chamber [43] [15].

In other researches, the diffused back illumination was used to investigate spray flame behavior in diesel engines [44] [45] [46] [47] [48] [49]. This study examined the characteristics of diesel spray combustion using three imaging methods under various injection pressures (100–300 MPa) and hole diameters (0.07–0.133 mm) [50]. It found that, beyond a certain point, the turbulent mixing in the spray diminishes without bright flames due to a cool flame combustion process. Ignition timing was determined through a method that was validated by another imaging technique. Using a micro-hole injector and very high injection pressure can significantly reduce ignition delay. Significant oxidation was seen both upstream and downstream in the micro-hole injector. However, this study was conducted using control volume combustion chamber (CVCC), as shown in Figure 1.8. The result showed that increasing the injection pressure and reducing the hole diameter can lead to a shorter ignition delay. Notably, the use of a micro-hole diameter injector combined with ultra-high injection pressure effectively diminishes the droplet diameter during fuel atomization and results in a lower average equivalence ratio. These factors play a crucial role in significantly reducing the ignition delay

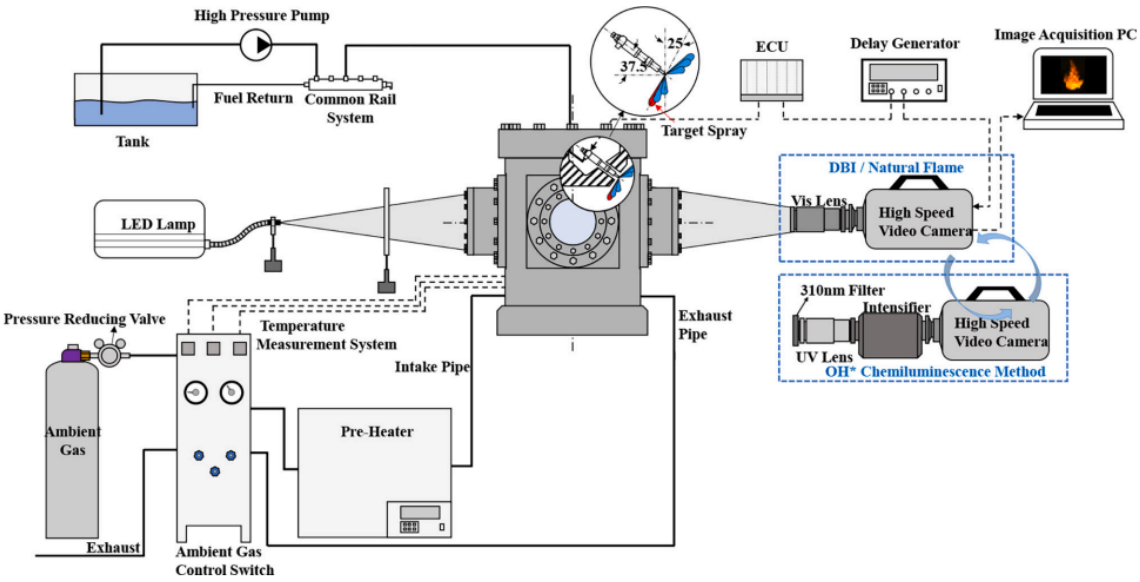

Figure 1.8 Optical arrangement of diffused back illumination [50]

1.4.4 Effect of Multiple Injection Strategy and Common Rail Pressure Variation on Wall Heat Transfer and Flame Behavior

To comply with environmental regulations and reduce emissions, split injection sprays have been adopted to enhance engine performance, efficiency, and mitigate wall heat transfer and emissions in diesel engines [51] [52] [53] [54] [55]. A recent study compared single and split injection sprays to examine spray flame behavior in a combustion chamber. It was found that the single-injection strategy achieved the highest natural flame luminosity and apparent heat release compared to split injection sprays [56]. Pilot injection tends to elevate gas temperatures in the combustion chamber, thereby accelerating ignition of the main spray. Additionally, a longer interval between split injection sprays tended to reduce the maximum apparent heat release rate and natural flame luminosity. Despite numerous studies on split injection sprays, there remains a strong demand for further investigations into the combustion process of sprays in diesel engines [57] [58]. Also, several studies have been conducted on spray interaction, mixture formation, ignition location, emissions, and combustion visualization using RCEMs [59] [60] [61] [62]. High common rail pressure enhances spray atomization and fuel evaporation, resulting in a more homogeneous mixture that improves engine efficiency and reduces soot emissions [63] [64] [65] [66] [67]. Furthermore, improved air entrainment enhances air-fuel mixture formation and reduces soot residence time [68] [69] [70]. Moreover, the effect of nozzle geometry, temperature of ambient gas and piston wall also influence to the auto ignition, flame temperature and soot generated [71] [72] [73].

Researchers are increasingly attempting to develop methods to minimize heat loss in Internal Combustion Engines (ICEs) to address the problem of fossil fuel shortage.

Multiple injection is one potential solution to reduce heat loss [74]. Multiple injections under a high common rail pressure not only improves engine efficiency, but also reduces exhaust emissions [75] [76] [77]. Although several studies have been conducted on the effect of multiple injections at high common rail pressure, further investigation is required to optimize the efficiency, emissions, and heat transfer in diesel engines [78] [79]. To maximize thermal efficiency, the mechanism of heat transfer from the combustion gas to cylinder must be fully understood. Thus, this study focuses on analyzing the heat transfer process during internal combustion.

To understand the thermal efficiency in more, the effect of spray interaction was investigated using a rapid compression and expansion machine [43]. Mixture formation, ignition location, and soot generation were visualized using a high-speed video camera [80] [81] [82] [83] [84]. A common rail pressure of 120 MPa was defined as the standard condition for implementing fractional injection strategies with a concentration of 15% O_2 as the ambient gas. The apparent heat release rate was reduced using split injection strategies, and the onset of main combustion was recommended. Furthermore, the air-fuel mixing process, combustion, and emissions were effectively controlled using fuel split injection [85]. Kuboyama et. al [86] investigated relationship between heat transfer through cylinder wall. It used 100 MPa common rail pressure with swirl ratio and nozzle orifice diameter variation. The results show that the flame and distribution temperature give dominant effect to the heat flux. Since the nozzle orifice diameter is increased, the average flame temperature also increased and the local heat flux on the cavity bottom decreased. The increasing swirl ratio affected to increase average flame temperature and changed temperature distribution which contributes to the local heat flux.

In diesel engines, enhancing thermal efficiency can be achieved by increasing

common rail pressure and reducing injector hole diameter [87]. Variations in injector hole diameter and common rail pressure were studied to determine their effects on spray characteristics. Increasing common rail pressure did not significantly alter spray penetration or injection delay. However, to effectively reduce soot emissions and ignition delay, common rail pressures between 100-300 MPa are recommended. The use of smaller injector holes and higher common rail pressures promotes strong oxidation on both upstream and downstream flame sides [88]. Mahmud et al. [89] investigated wall heat transfer phenomena using a constant vessel setup to elucidate its correlation with local flame proximity to the wall. They found that increasing common rail pressure increases the wall heat transfer coefficient [90]. Notably, the local wall heat flux exerted a more pronounced influence than the distribution of local flame temperature on wall heat transfer.

Other investigation was conducted to examine the impact of split injection on fuel spray and combustion processes [15]. Experiments were conducted at common rail pressures 80 MPa, 120 MPa, and 180 MPa, with an oxygen concentration of 15%. The interaction between the fuel spray and the piston wall, as well as mixture distribution and ignition location, were analyzed using the shadow method and natural flame luminescence. The study revealed that higher injection pressures and split injection with longer intervals significantly enhanced combustion performance. Additionally, advancing the pilot injection reduced soot generation, while the influence of high injection pressure on heat release diminished. Flame separation was observed at high injection pressures, which helped reduce soot by increasing the fuel-air interaction area, as shown in Figure 1.9. In comparison to shorter injection intervals, longer intervals gradually reduced high-temperature flames, which were eventually obscured by a soot cloud. This slower heat

release suggests that longer intervals could effectively mitigate combustion noise and soot particle formation.

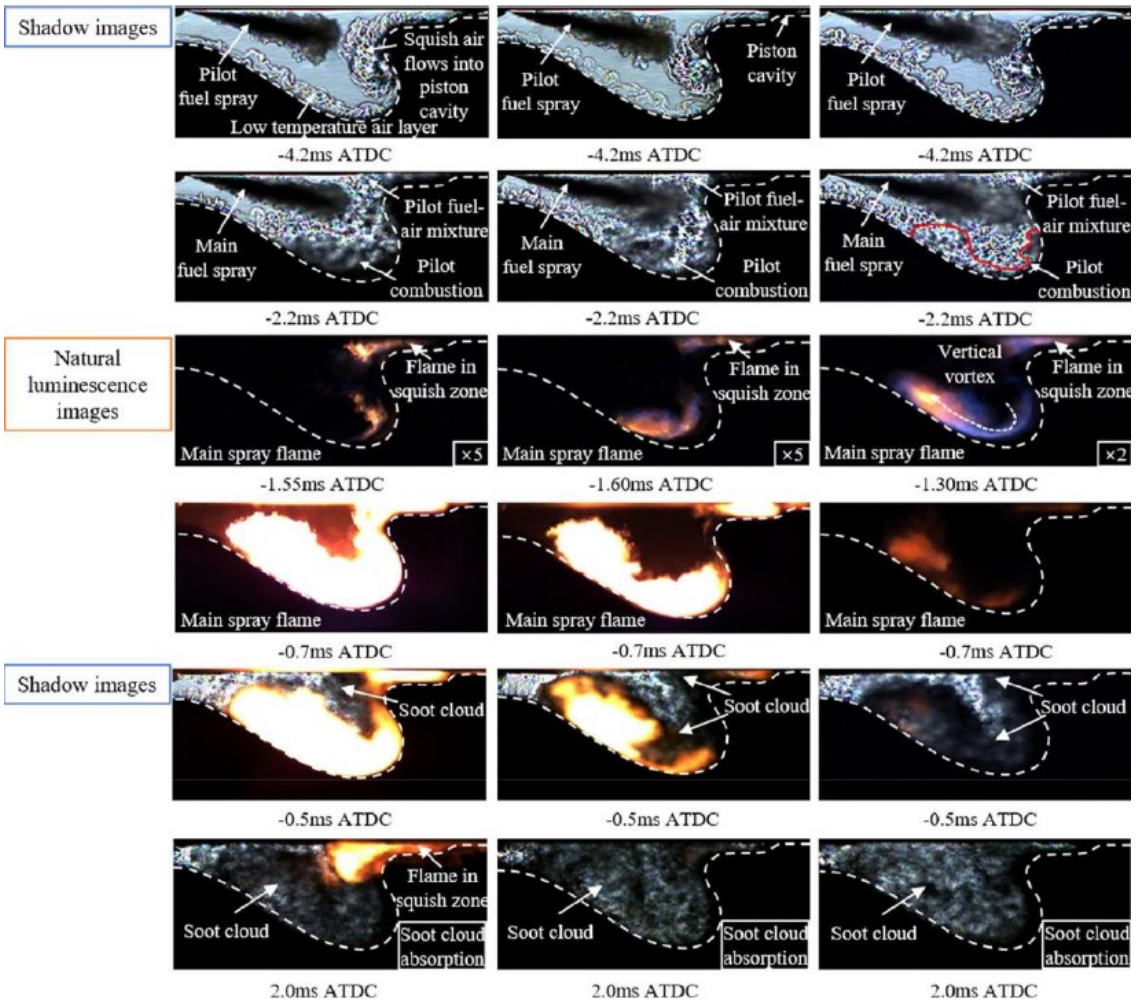

(a) 80 MPa (b) 120 MPa (c) 180 MPa

Figure 1.9 Spray flame behavior under double injection strategy using common rail pressures variation [15].

1.4.5 Heat Transfer Correlation

According to the previous studies on heat transfer phenomena [91], the Nusselt and Reynolds number correlations can be used to investigate the heat transfer. In 1923, Nusselt correlated the pressure and temperature as a relationship of free convection [92]. By the other researchers, the heat transfer correlations between gas and wall in ICE and

others correlations were also proposed to calculate the heat transfer coefficient [93] [94] [95] [96] [97] [98].

There are many predictions of correlation of heat transfer coefficient in ICE by another researchers [99]. The most equations which were used for heat transfer correlations was derived by Annand [100] and Wochni [101]. These equations are depending on the turbulence flow analysis correlating the Nusselt (Nu), Reynolds (Re), and Prandtl (Pr) numbers. The correlation between Nu, Re, and Pr numbers is used for calculating the heat transfer phenomena on internal pipe flow and flat plates [102]. Kuboyama et. al. [103] was also correlating the heat transfer of diesel engines in the combustion chamber. The Quasi-steady momentum theory and Woschni's equations were used to obtain characteristic velocity during the injection duration and after injection duration, respectively. The bore diameter and average gas temperature was used as the characteristic length and flame temperature, respectively. The results showed that the Nusselt number had proportion to the 0.8^{th} power of the Reynolds number.

1.5 SUMMARY

To investigate the heat loss occurring during the heat transfer from combustion inside the cylinder to the wall, the heat transfer mechanism should be understood to optimize the thermal efficiency of diesel engines. This study clarifies the effect of common rail pressure and multiple injection strategy on the two-holes and six-holes injector. In addition, the heat transfer phenomena would be represented using the Nusselt and Reynolds number correlations. Moreover, the previous study was presented in this chapter which has the results that this study is correlated with the enhancing thermal efficiency in diesel spray combustion.

CHAPTER 2 EXPERIMENTAL APPARATUS AND MEASUREMENT METHODS

2.1 RAPID COMPRESSION AND EXPANSION MACHINE

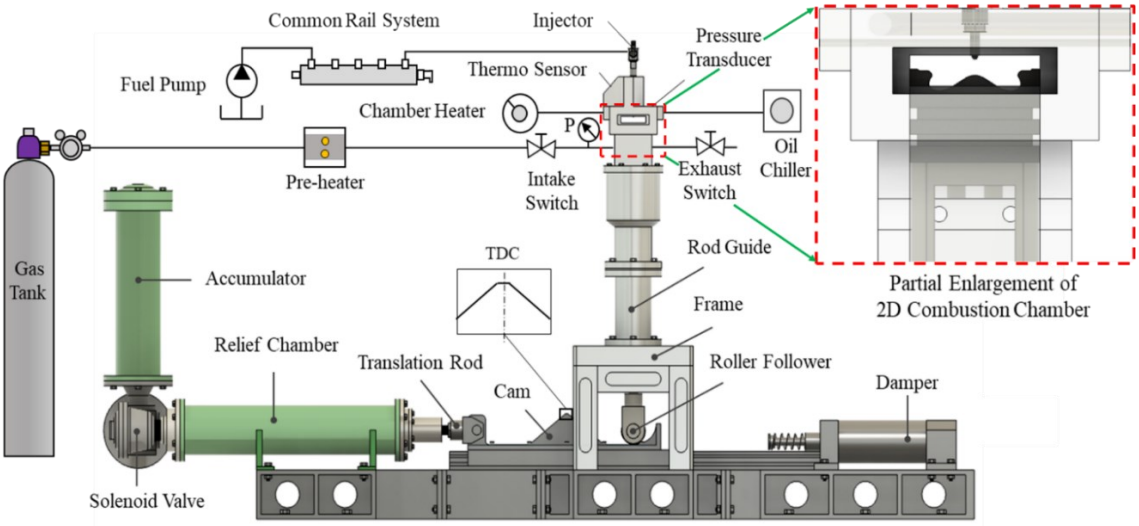

(a) Entire apparatus

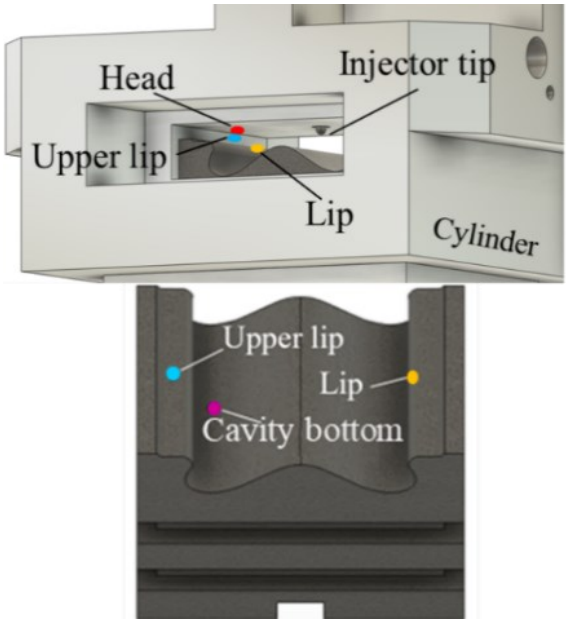

(b) 2D cylinder head and piston,

Color dots denote heat flux sensor locations.

Figure 2.1 Schematic of Rapid Compression and Expansion Machine apparatus.

Table 2.1 RCEM specifications and operating conditions.

Parameters	Values
Chamber length × width [mm]	84 × 61
Stroke [mm]	94
Displaced volume [L]	0.54
Piston top land clearance [mm]	1.0
Piston-wall crevice [mm]	0.2
Piston-window crevice [mm]	0.2
Piston cavity material	S45C
Chamber wall material	S45C

This study focused on investigating the spray and flame behaviour using an RCEM to simulate a single-cycle diesel engine. To obtain the actual operating conditions of the diesel engine, the oil chiller was channelled to the cylinder side, the heater was operated under the measurement conditions, the intake gas (18% O_2 + 82% N_2) was channelled to the chamber, and the accumulator flow was determined based on the operating target. The experiment was initiated by operating the solenoid valve, which caused high-pressure air to flow from the accumulator into the relief chamber. Furthermore, the translation rod moved the cam to the horizontal position. The compression stroke was achieved when the roller follower was elevated by the cam. The fuel was injected into the combustion chamber, and the roller follower was driven down to the lowest position to simulate the expansion stroke. The cam was fixed in place by a damper. A schematic of the RCEM apparatus is shown in Figure 2.1 (a). To provide comprehensive information on the wall heat transfer during the combustion process, wall heat flux sensors were installed on the cylinder (cyl) and cavity (cav) side, as shown in Figure 2.1

(b). On the cavity side, two measurements cavity upper lip and bottom (Cav Upper Lip and Cav Bottom) were performed on one spray, whereas the other cavity lip (Cav Lip) was measured on the other side. On the other side, two wall heat flux sensors were placed in the cylinder head and liner (Cyl head and Cyl liner). The specifications and operating conditions of the experimental apparatus are listed in Table 2.1. The results are reported as the average of three separate experiments.

2.2 STEPPED PISTON CAVITY

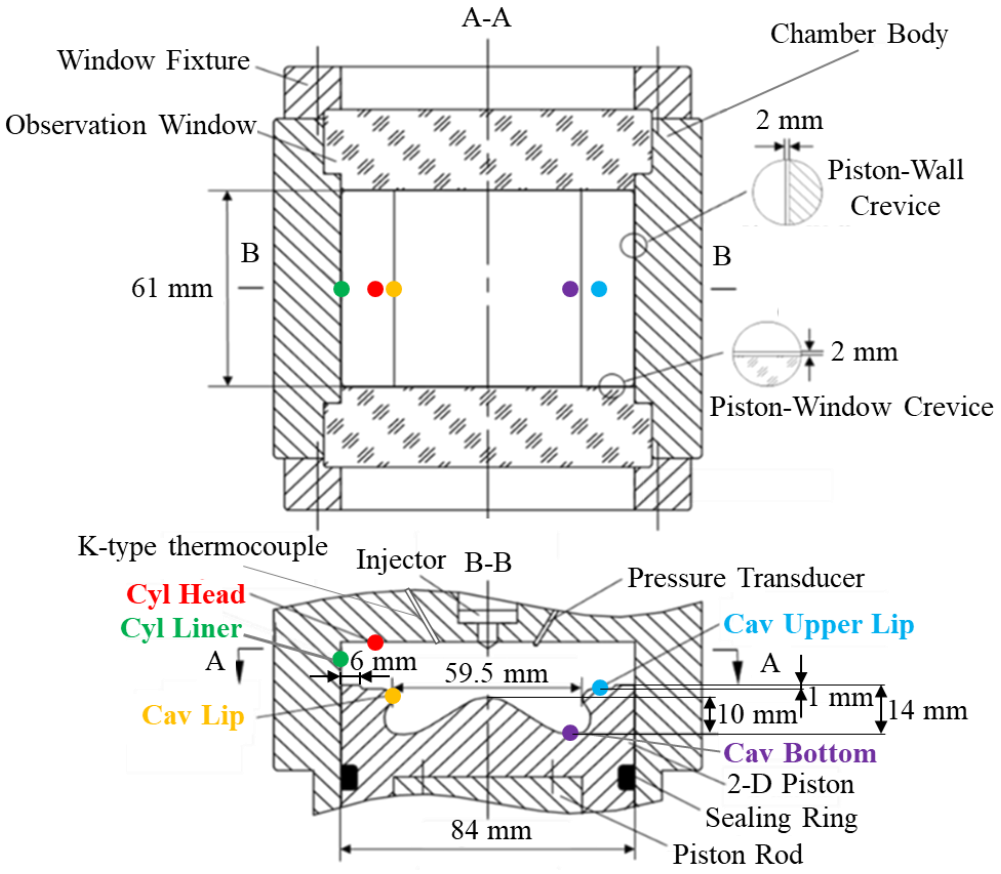

Figure 2.2 2D combustion chamber (stepped piston cavity, cylinder head and liner) and heat flux sensor locations.

In this study, we adopted a two-dimensional piston cavity to fully visualize the spray and flame behaviour during the combustion process. The piston cavity was sealed using

a rectangular piston rubber ring adjusted to the piston size. A pressure transducer and K-type thermocouple were employed to record the pressure and temperature distribution on the top surface of the cylinder. The injector was installed vertically at the centre of the combustion chamber. The piston cavity was bolted to a piston rod connected to the roller follower. Details of the 2D combustion chamber are shown in Figure 2.2.

2.3 OPTICAL ARRANGEMENT

The diffused backlight illumination (DBI) method was used to investigate the spray and combustion processes, as shown in Figure 2.3. The DBI method has been used by other researchers to present the characteristics of the spray and combustion processes [104] [105] [106]. The visualization was performed using a high-speed video camera (Photron FASTCAM SA-Z) connected to a 200 mm focal length lens and set to 20,000 frames per second (fps). The captured results were processed using an image acquisition PC. The injector had one hole in the left direction and another hole in the right direction. Glass windows with a length and width of 86 mm and 30 mm, respectively, were used to fully observe the combustion chamber. A pinhole with a diameter of 1 mm was employed as a light source to illuminate the spray, exothermic, and combustion processes. Strong light from the light source was spread using a diffuser. To comprehensively analyse the flame distribution during the combustion process, a direct photography (DP) without a light source was also employed. The local flame temperature was obtained by applying using the two-colour analysis method to the captured images. In addition, the normalized image could be obtained using image processing to fully investigate the luminous flame distribution during the combustion processes.

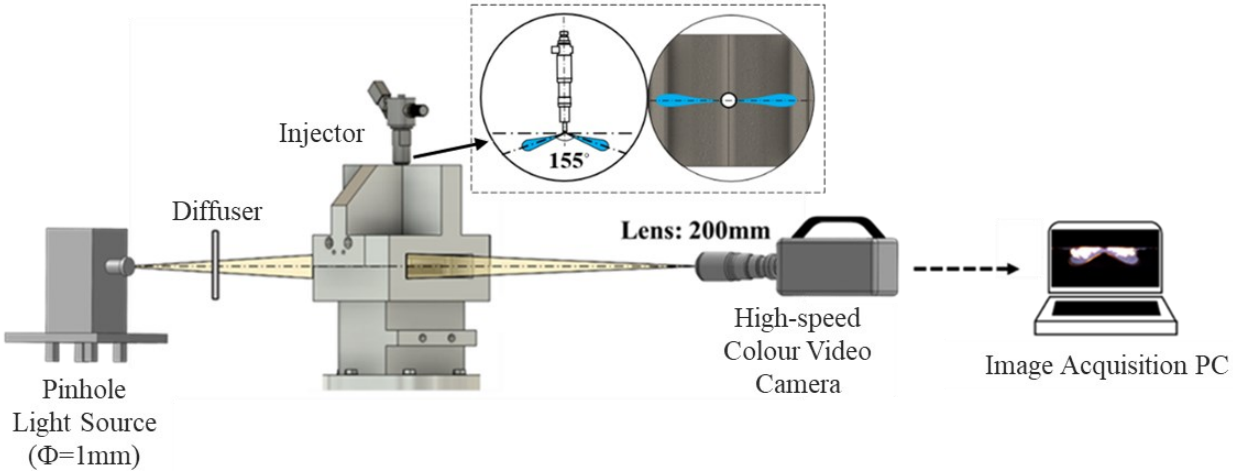

Figure 2.3 Diffused backlight illumination (DBI) optical arrangement.

2.4 WALL HEAT FLUX MEASUREMENT

In this study, the wall heat flux sensor (Medtherm 10702 B) was equipped with two thermocouples: a K-type and J-type thermocouple. The K-type thermocouple-equipped sensor was placed in the piston cavity, composed of chromel and alumel. Meanwhile, the J-type thermocouple-equipped sensor was positioned in the cylinder, constructed from iron and constantan, as illustrated in Figure 2.4. These materials were connected to the positive and negative wires, respectively. The outer thermoelement serves as the positive leg, while the in-depth thermocouple acts as the negative leg, with its negative wire securely cemented in the groove. The wall heat flux sensor has a 1-2 µm thick surface and a 1 µs response time. The heat in the combustion chamber was converted to a frequency signal using a cold junction reference. This sensor is produced by Techno Office Co., Ltd. An amplifier was used to obtain the signal, which was presented using an oscilloscope. The visual basic was used to calculate the wall heat fluxes, as presented in the results.

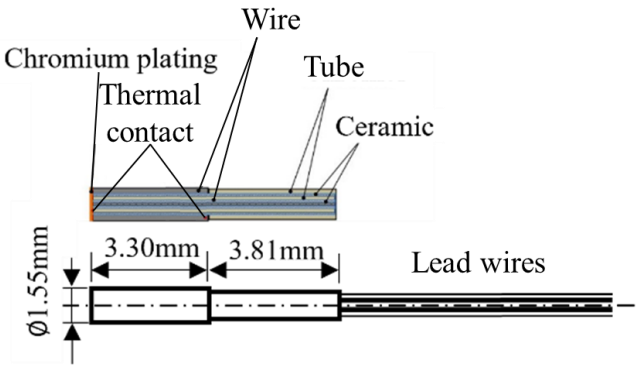

Measuring Location	Part. No.	Thermocouple	
		Type	Material
Piston cavity: upper lip, lip, and bottom	TCS-K(KN)-10702B	K	Chromel (tube) Alumel (wire)
Cylinder: head and liner	TCS-J(JN)-10702B	J	Iron (tube) Constantan (wire)

Figure 2.4 Heat flux sensor configuration and specifications.

To calculate the wall heat flux on the surface of the cylinder and cavity, we applied a one-dimensional (1D) and non-steady-state heat conduction equation to acquire the surface and inner wall temperatures. This method was previously reported by Tatsumi et al. [107]. The second-order partial differential equation was used as the basic equation, given by Eq. (2.1).

$$\frac{\partial T}{\partial \tau} = \alpha \frac{\partial^2 T}{\partial x^2} = \frac{\lambda}{c_p . \rho} \frac{\partial^2 T}{\partial x^2}, \tag{2.1}$$

where T denotes the temperature $[K]$, τ the time $[s]$, x the thickness direction location $[m]$, α the thermal diffusivity $[m^2/s]$, λ the thermal conductivity $[W/(m \cdot K)]$, c_p the specific heat $[J/(Kg.K)]$, and ρ the density $[Kg/m^3]$. To calculate Eq. (1), the finite element method was applied. Eq. (2) was derived using the wall surface and inner wall temperature dimensions of the cylinder and cavity.

$$T(i, k+1) = T(i, k) + \Theta x\{T(i+1, k) + T(i-1, k) - 2T(i, k)\} \tag{2.2}$$

where i indicates the direction step in the wall surface (for the wall surface and inner wall surface, $i = 0$ and $i = n$, respectively), k denotes the direction step in time,

$T\ (i,k)$ refers to the wall surface temperature for i at time k, and $\Theta x = \alpha \frac{\Delta\tau}{\Delta x^2} \leq \frac{1}{2}$. Stability criteria were used to derive Eq. (3) and the inner wall surface temperature was used to calculate the unsteady surface heat flux component.

$$q(k) = h\left(T_{flame} - T_{wall}\right)$$
$$= \frac{\lambda}{\Delta x}\{T(0,k) - T(1,k)\} + C_p \rho \frac{\Delta x}{2} \frac{T(0,k+1) - T(0,k)}{\Delta\tau} \quad (2.3)$$

where q indicates the wall heat flux, h denotes the heat transfer coefficient, and Δx refers to the width of division in the time and step direction ($\Delta x = 20\ \mu m$ and $\Delta\tau = 10$ μs).

2.5 EXPERIMENTAL CONDITIONS

This experiment was conducted by using a triple injection: pilot, pre-(preceding), and main injection strategy and applying a two-dimensional stepped piston cavity with a total injected fuel mass of 3.5 mg. The pilot, pre-, and main injection were injected at timing of -13ms, -5ms, and -4ms ATDC, respectively. The injection timings (pilot, pre-, and main) were injected before top dead center (TDC), resulting in an increased concentration of the rich mixture in the cavity upper lip space. The oil chiller flowed to the inside of the cylinder to maintain a head temperature of 330 K.

To obtain the piston movement, a Keyence laser sensor was installed in the near cam. The engine speed was maintained at 525 rpm with a compression ratio of 14.5 from the motoring test. The motoring test conditions and results were previously reported in [43] [15]. The accumulated pressure in the accumulator was set as 0.225 MPa. The polytrope index was 1.27, which was calculated based on the relationship between ambient pressure and volume. A pressure transducer was installed on the head of the cylinder to

measure the ambient pressure. In addition, the volume was calculated based on the piston movement. To obtain comprehensive results, we applied common rail pressures 75, 100, 125, and 150 MPa in the experiments. In this report, a common rail pressure 125 MPa was used as the baseline. The experimental conditions are listed in Table 2.2.

Table 2.2 Experimental conditions.

Parameters	Values			
Fuel Injection				
Fuel	JIS#2 Diesel			
Common rail pressure P_{rail} [MPa]	75, 100, 125 (baseline), 150			
Injector hole diameter [mm]	0.106			
Number of injector holes	1x2 (1 left and 1 right)			
Umbrella angle [deg.]	155			
Split injection stage	Total	Pilot	Pre-	Main
Injection timing [ms ATDC]		-13	-5	-4
Injection amount [mg]	3.50	1.20	0.30	2.0
Injection amount per hole [mg]	1.75	0.60	0.15	1.00
Combustion Chamber				
Piston cavity	Stepped piston cavity			
Compression ratio	14.5			
Intake gas	18% O_2 + 82% N_2			
Initial ambient temperature [K]	330			
Oil chiller temperature [K]	333			
RCEM Operation				
Simulated engine speed [rpm]	525			
Accumulated pressure [MPa]	0.225			
Polytrope index	n = 1.27			

This study focused on wall heat transfer and emissions analysis during the combustion process. We employed split injection sprays with varying common rail pressures to investigate the relationship between spray flame behavior and wall heat

transfer. Additionally, a soot emissions analysis was conducted. We used an early pilot injection under low in-cylinder pressure to enhance air-fuel mixture formation in the upper lip space. The main injection spray was introduced later than the pre-injection spray, filling the cavity bottom space. A schematic of the split injection spray in this experiment is shown in Fig. 1. This experiment is novel because few researchers have utilized a two-dimensional (2D) piston cavity to thoroughly investigate the combustion process in diesel engines. Previously, a constant-volume vessel with a 2D piston cavity was employed to study spray flame behaviour and soot emissions in the combustion chamber by varying the common rail pressure and applying split injections using the LAS technique [21] [22] [23] [39]. In addition, a 2D piston cavity was also used to investigate the performance of spark-ignition engines [108] [109] and diesel engine [110].

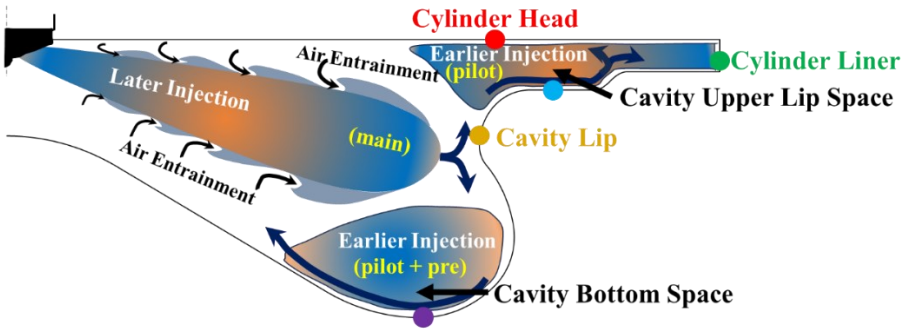

Figure 2.5 Schematic of split injection sprays in stepped piston cavity,

Color dots denote heat flux sensor locations.

2.6 SUMMARY

In this study, a single cycle diesel engine was simulated using a rapid compression and expansion machine (RCEM). The 2-dimensional piston cavity was used to investigate the spray and combustion process in the combustion chamber. Also, five heat flux sensors were installed in the cylinder head, cylinder liner, cavity upper lip, cavity lip, and cavity bottom to understand the heat transfer phenomena in the cylinder and cavity side. The

Diffused Back Illumination with light and without light source were performed. The in-cylinder pressure, in-cylinder temperature, apparent heat release rate, wall heat flux, and spray flame behavior were obtained using this experimental apparatus. We used a two-hole injector to properly visualize spray and flame behavior during the combustion process in the combustion chamber. A stepped piston cavity was employed as a new model in this experiment. An early pilot injection was set up to increase the formation of a rich mixture in the cavity's upper lip space. Additionally, variations in common rail pressure were used to investigate their effect on wall heat transfer and spray flame behavior in the combustion chamber.

CHAPTER 3 CORRELATION BETWEEN WALL HEAT FLUX CHARACTERISTICS AND SPRAY FLAME BEHAVIOR UNDER BASELINE CONDITION P_{RAIL} = 125 MPa

3.1 OVERALL RESULTS OF WALL HEAT FLUX CHARACTERISTICS AND SPRAY FLAME BEAVIOR

In this study, a common rail pressure 125 MPa was used as the baseline for comparison with other common rail pressures 75, 100, and 150 MPa. The spray, combustion process, and heat transfer in the combustion chamber were observed and correlated between the measurements and visualizations, as shown in Figure 3.1. The air-fuel mixture formation filled the combustion chamber at a high temperature before the combustion process, as the fuel spray spread, and wall impingement effectively promoted fuel evaporation and air-fuel mixture formation. During the compression stroke, the in-cylinder pressure and temperature increased gradually. Meanwhile, the expansion stroke decreased the in-cylinder pressure and temperature. The pilot injection spray was introduced first, which contributed to the rich mixture formation staying in the upper lip space with a lower in-cylinder pressure. During the compression stroke, the volume of the combustion chamber decreased gradually, which increased the rate of in-cylinder pressure and temperature. The pre-injection spray flowed 1ms earlier than the main injection spray under the high-pressure and high-temperature conditions. Furthermore, natural flame combustion first occurred at -3.15ms ATDC around the upper lip space owing to the rich mixture and then developed into the cavity bottom space.

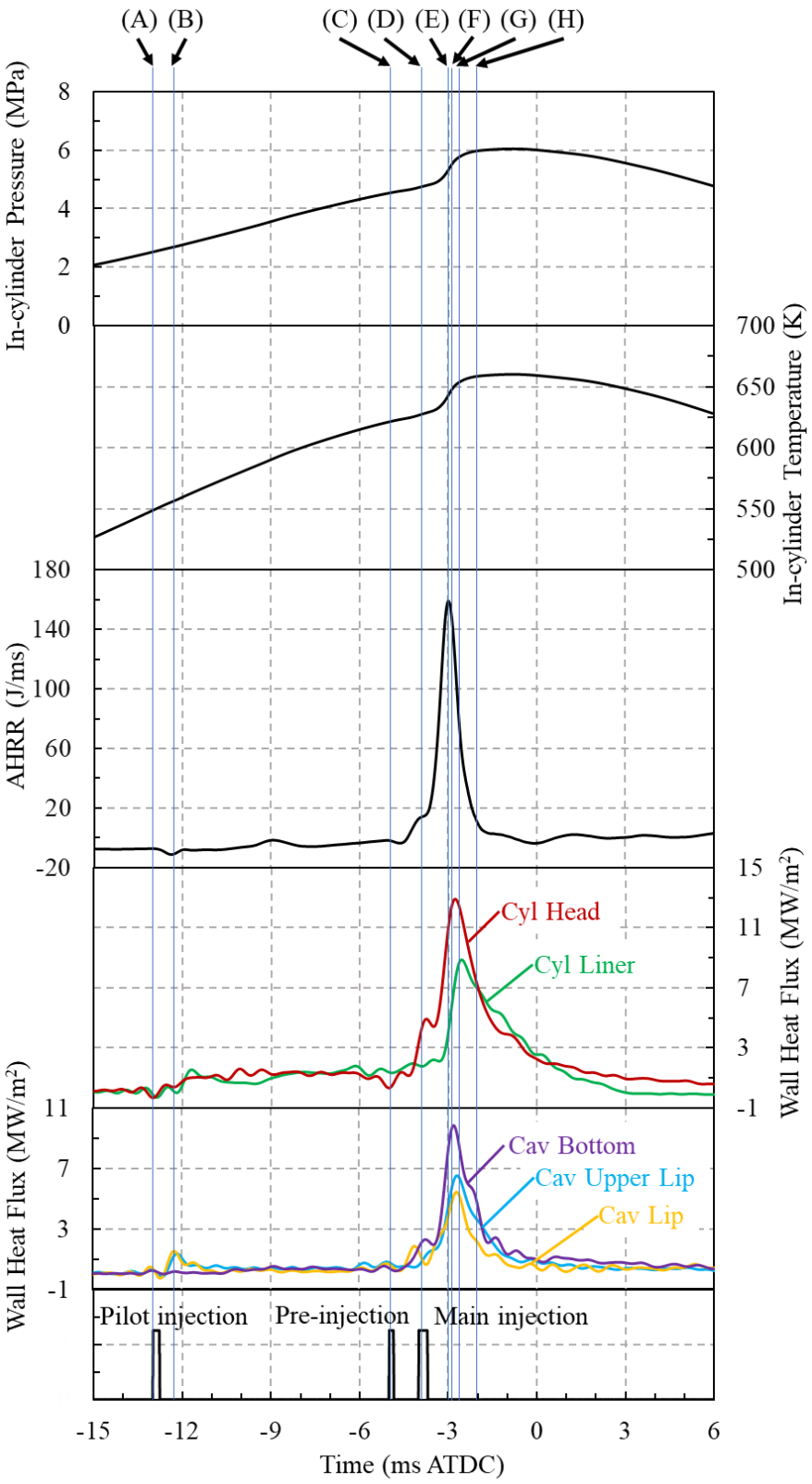

Figure 3.1 In-cylinder pressure, in-cylinder temperature, apparent heat release rate, and wall heat fluxes under common rail pressure P_{rail} = 125 MPa.

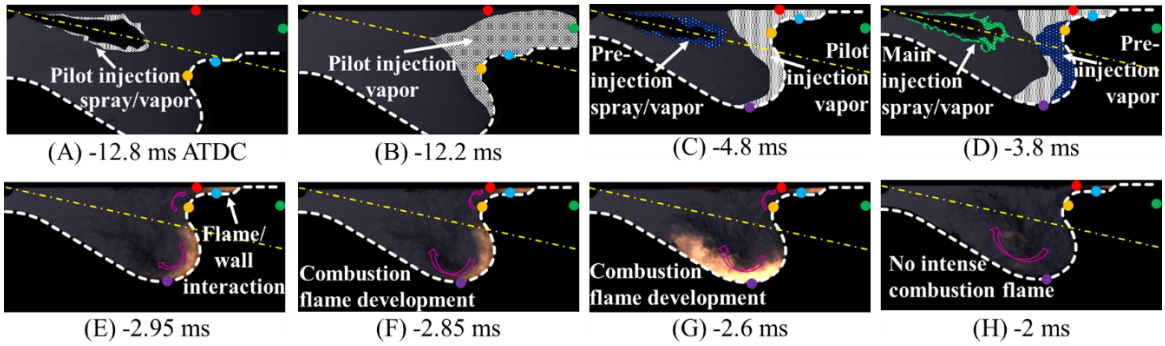

Figure 3.2 Temporal variation of spray/ vapor/ flame distribution common rail pressure P_{rail} = 125 MPa.

White dashed line denotes piston cavity boundary and color dots denote heat flux sensor locations.

In conclusion, the in-cylinder pressure and temperature increased significantly during combustion, which significantly increased the apparent heat release rate (AHRR). The pre-injection spray contributed to increasing the AHRR first because of the hot evaporation spray/vapor, which resulted in impingement. The fuel evaporation absorbed the high energy in the combustion chamber, which decreased the AHRR during the fuel injection spray; however, a more significant increase in the AHRR occurred during combustion.

Figure 3.2 presented the temporal variation of spray/vapor/ flame behavior distribution at common rail pressure 125 MPa. The result shows that the ignition was not reached after the pilot and pre-injection, as shown in Figures 3.2 (a) - (c). In addition, the ignition only did not appear during the main injection duration, as shown in Figure 3.2 (d). A high common rail pressure 125 MPa enhances the lean mixture formation which reduce the luminous flame and combustion duration during the combustion processes. Furthermore, the low luminous flame appears to the combustion chamber after main

injection, as shown in Figures 3.2 (e)-(h).

To further describe the wall heat transfer in the cylinder and piston cavity wall, Eqs. (2.1) - (2.3) were applied to obtain comprehensive information on the wall heat flux. During the pilot injection spray, an adequate fuel mixture tended to remain around the cavity lip and cavity upper lip. This affected the evaporation process and led to an ignition delay in these regions. Then, the wall heat flux increased in the cavity lip and cavity upper lip (yellow and blue lines, respectively) owing to the hot evaporation spray penetrating to these regions. Meanwhile, the wall heat flux at the bottom of the cavity tended to remain constant during the pilot injection spray. This clearly shows that the wall heat flux in the cylinder head and liner tended to increase during the pilot injection spray. These higher wall heat flux regions correspond to the first contact between the hot evaporation spray and the relatively cold wall surface, resulting in a larger temperature difference and enhanced heat transfer. All injection sprays arrived initially in the cavity lip, which contributed to the location of the first increasing wall heat flux, followed by an increase in the cavity upper lip and cavity bottom on the cavity side. The pre-injection spray improved the lean mixture formation and reduced the combustion duration. During the main injection spray, the wall heat flux decreased for a short time owing to the high latent heat, and then increased significantly during the period of the intense combustion flame. The highest wall heat flux peak was found in the cylinder head region because of the longer flame residence time in this region and the high-temperature surface contributed by the hot oil chiller flowing inside the cylinder side. On the cavity side, the wall heat flux at the bottom of the cavity had the highest peak value owing to the strong combustion flame that occurred in this region. In summary, the injection spray increased the wall heat flux during the intense combustion flame and decreased gradually during the weak combustion flame.

The wall heat flux in the cylinder head has a more significant impact on wall heat transfer compared to the cylinder liner. Additionally, the current location of the wall heat flux sensor, installed on the cylinder side, plays a more crucial role in reducing wall heat transfer, thereby enhancing thermal efficiency. We assume that in the cylinder side, the current location of the wall heat flux is the most critical in the cylinder head due to the extended flame residence time in that region. In addition, studying the local wall heat transfer helps in understanding the heat transfer dynamics in real diesel engines.

3.2 ACCUMULATED WALL HEAT FLUX

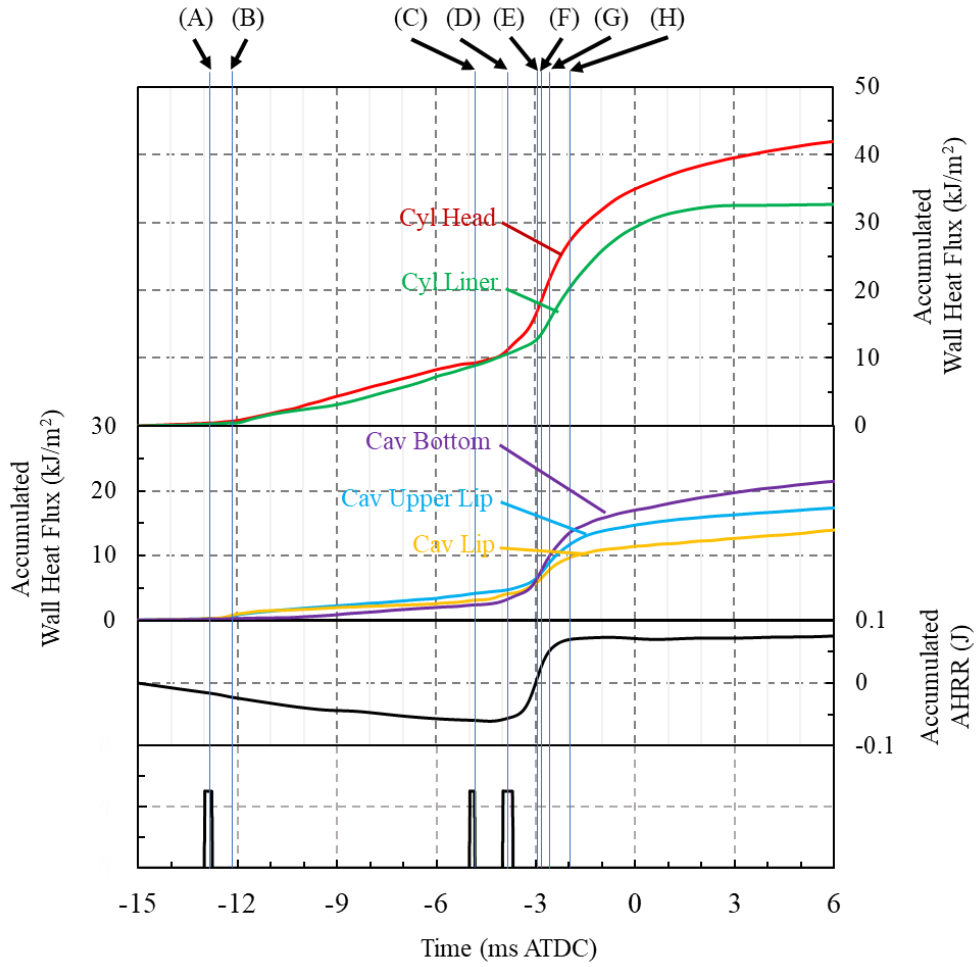

Figure 3.3 Accumulated heat flux of each measured position under common rail pressure 125 MPa.

To investigate the heat transfer in the wall, the accumulated wall heat flux was presented in this study. The accumulated wall heat flux was calculated based on the wall heat flux value and time, whereas the accumulated apparent heat release rate (Accumulated AHRR) was calculated using the AHRR value and time. The distributions are shown in Figure 3.3. Initially, the total heat value increased gradually; however, after injection, the total heat decreased significantly. In particular, the cylinder head exhibited the highest accumulated wall heat flux compared with the other locations because a large amount of fuel ignites near the cylinder head, necessitating a longer time to complete combustion. In contrast, the squish zone has space to accommodate the fuel mixture. Hence, the combustion flame in the squish zone is the least significant, which influences the accumulated wall heat flux in the cylinder liner. The accumulated wall heat flux difference on the cylinder wall (cylinder head and cylinder liner) is approximately 12.11 kJ/m^2 while that obtained from the piston cavity (cavity bottom and cavity lip) is approximately 7.27 kJ/m^2. The difference in the accumulated wall heat flux between the different locations is caused by the location of the heat and a lack of oxygen. In addition, the accumulated AHRR tend to decrease before the combustion processes appearing due to the latent heat and gradually increasing following the start of the ignition.

3.3 SUM OF ACCUMULATED WALL HEAT FLUXES

In this chapter, we calculated the sum of the accumulated wall heat fluxes to investigate the effect of common rail pressure on the total heat transfer at the measuring locations. A summary of the effect of the common rail pressure on the total heat transfer is presented in the next chapter. The results show that the sum of the accumulated wall heat fluxes at a common rail pressure 125 MPa slightly increases compared to the accumulated wall heat flux, as shown in Figures 3.3 and 3.4. This increase is more

significant during the main combustion processes.

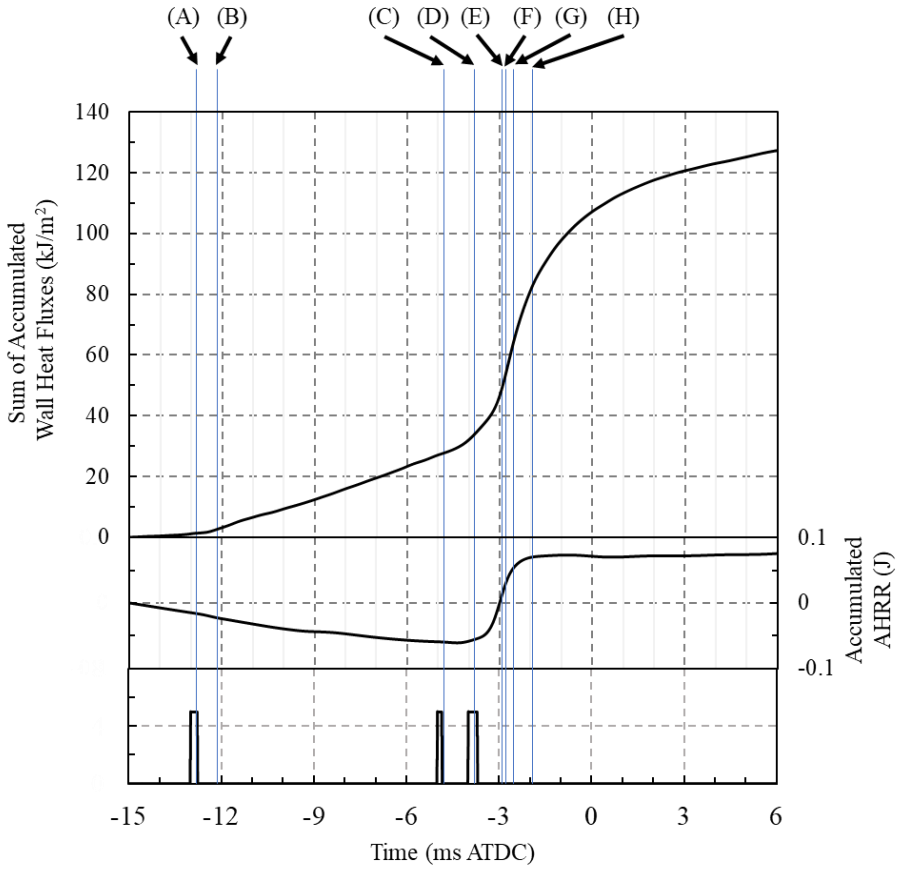

Figure 3.4 Sum of accumulated wall heat fluxes under common rail pressure 125 MPa.

3.4 SUMMARY

In this chapter, we presented the correlation between in-cylinder pressure, in-cylinder temperature, apparent heat release rate (AHRR), wall heat flux, and the spray and flame behavior during the pilot, pre, main injection, and combustion processes. In addition, we calculated the accumulated wall heat flux based on the wall heat flux values and time. Furthermore, the accumulated wall heat fluxes were summed up for each heat flux measuring location: cylinder head, cylinder liner, cavity upper lip, cavity lip, and cavity bottom, as the sum of accumulated wall heat fluxes.

The early pilot injection at -13ms ATDC contributed to distribute the spray/vapor on

cavity upper lip space than cavity bottom space. Then, the homogeneous mixture formation was achieved, resulting in the increasing in-cylinder temperature. In-cylinder pressure and temperature increased significantly after main injection spray which increased the peak value of apparent heat release rate to the maximum value. Additionally, the pre-injection spray improved the mixture formation, thereby accelerating the main combustion process. Moreover, the small wall heat flux increase started at all locations with the pilot injection spray/vapor arrival excluding the cavity bottom. The large wall heat flux increase started with pre- and main injection spray flame arrival at all locations.

CHAPTER 4 EFFECT OF COMMON RAIL PRESSURE ON WALL HEAT FLUX CHARACTERISTICS AND SPRAY FLAME BEHAVIOR

4.1 SPRAY FLAME IMAGE PROCESSING

Normalizing a spray flame image using an average flame image is a critical step in ensuring consistent and comparable data for further analysis. The process involves calculating average pixel values, normalizing pixel intensities, and adjusting the range to standardize the images. This normalization helps in mitigating the effects of varying lighting conditions and improves the accuracy of the image analysis. In this study, the spray flame image processing is used to investigate the local luminous flame distribution in the combustion chamber. The raw image, obtained without backlight illumination (direct photography), is used to reduce saturation from the light source. The first step involves extracting the flame area. The second step is calculating the average pixel values, which are used to normalize the non-dimensional flame pixel values. The final step is creating contour figures.

4.1.1. Extract the Flame Area

The entire flame image is used to obtain the average pixel value of the flame image. The first step involves removing the background image from the raw image, as shown in Figure 4.1(a). The background image in this experiment is black, which simplifies the process because the pixel value of black is zero. Furthermore, the flame image without the background is shown in Figure 4.1(b). The grayscale image of the entire flame is used to simplify image processing. The steps for extracting the entire flame area from the raw image are shown in Figure 4.1.

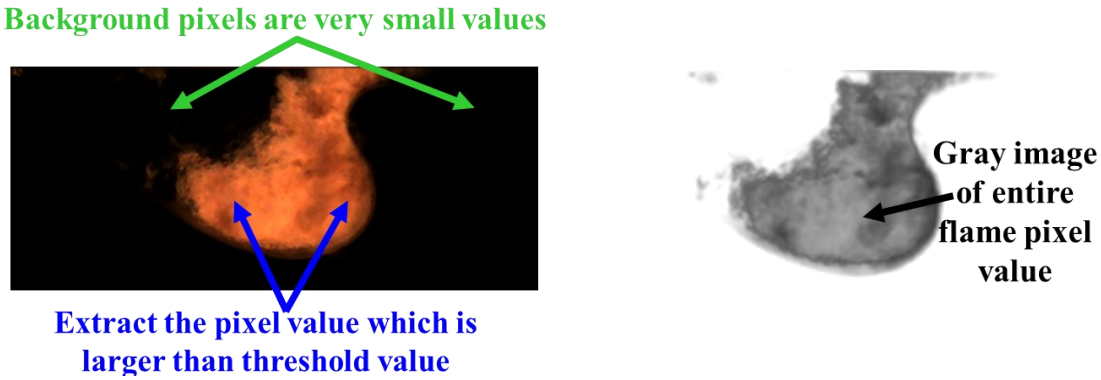

(a) Spray flame image (raw image) (b) Entire flame image without background

Figure 4.1 Extracting of the entire flame area from raw image.

4.1.2 Take the Average of the Entire Flame Pixels Values

The average of the entire flame pixel values is used to normalize the pixel values in the next step. This average refers to the mean intensity value of all the pixels that make up the flame in an image. It represents the average brightness or intensity of the flame and is calculated by summing the pixel values and then dividing by the total number of flame pixels. The average of entire flame pixels values (APV) is given by equation (4.1).

$$APV = \frac{\sum_{i,j} Pixel\ value\ (i,j)}{Number\ of\ pixels} \tag{4.1}$$

4.1.3 Calculate Non-dimensional (Normalized) Pixel Value

Non-dimensional pixel values using the average pixel value involve scaling the pixel intensities relative to the mean intensity of the image. This normalization method provides a means to express pixel values as proportions of the average intensity, facilitating analysis of variations within the image. The non-dimensional pixel value is employed for presenting the luminous flame distribution using a contour figure. The non-dimensional pixel value (NDV) is determined by the equation (4.2).

$$NDV\ (i,j) = \frac{Pixel\ value\ (i,j)}{APV} \tag{4.2}$$

4.1.4 Make Contour Pixel Value Figure

The non-dimensional pixel values are depicted via contour plots, elucidating the distribution of pixel intensities across the image. A consistent color scale ranging from low to high values is employed for visual clarity. The contour pixel values aid in a clearer comprehension of the local luminous flame distribution. We utilized MATLAB code to generate the contour plot, employing the 'linspace' function to interpolate 500 evenly spaced normalized values from low to high. The example result of contour pixel value figure is shown in Figure 4.2.

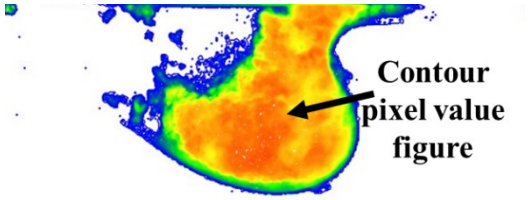

Figure 4.2 Result of image processing using contour pixel value figure.

4.2 MAIN COMBUSTION PERIOD RESULTS

To provide comprehensive information on the wall heat transfer in the cylinder and cavity wall, we report the results of four common rail pressure settings (75, 100, 125, and 150 MPa) in this section. The luminosity, ignition delay, and flame residence time were lower for higher common rail pressure values. Early pilot injection effectively decreased the soot flame luminosity and improved–the air-fuel mixture formation on the upper lip side. Consequently, the uniformity of the air-fuel mixture was effectively improved in the combustion chamber, which reduced the combustion duration and flame residence time in the combustion chamber. Higher common rail pressures increased the spray tip penetration, momentum, and velocity. In addition, air entrainment, spray atomization, fuel

evaporation, and air-fuel mixture formation were enhanced, which reduced the ignition delay. Consequently, increasing the common rail pressure significantly increased the peak value of the wall heat flux after the pre-injection spray in the cylinder head. Enhancing lean mixture formation reduced the ignition delay and shortened the combustion duration during the combustion process. This experiment was set up using an earlier pilot injection spray, which created a richer mixture at the cavity upper lip space compared to the cavity bottom. Meanwhile, the pre- and main injection spray/vapor produced a richer mixture at the cavity bottom space compared to the cavity upper lip space. In this section, we present only the main combustion period results, as no luminous flame appeared after the pilot and pre-injection sprays.

In the same location of wall heat flux measurement, the different common rail pressure provided no significant peak value of the wall heat flux in comparison, as shown in Figure 4.3. Flame combustion occurred only after the main injection spray at the four common rail pressures. The strongest luminous flame and longest flame residence time were observed at a common rail pressure 75 MPa, as shown in Figure 4.3 (a). The flame was distributed along the cavity side, extending from the cavity lip to the bottom space. Additionally, the luminous flame intensity in the cavity bottom space had increased significantly. Conversely, the luminous flame intensity at the cavity lip had decreased proportionally. In contrast, the highest common rail pressure 150 MPa successfully reduced the luminous flame, as shown in Figure 4.3 (d). Furthermore, regardless of the common rail pressure, the highest peak value of the wall heat flux was acquired by the cylinder head owing to the intense flame combustion occurring in this region and the effect of maintaining the surface temperature at all common rail pressures. The second highest peak value was obtained at the bottom of the cavity owing to the strong flame luminosity and largest contact area of the flame wall interaction.

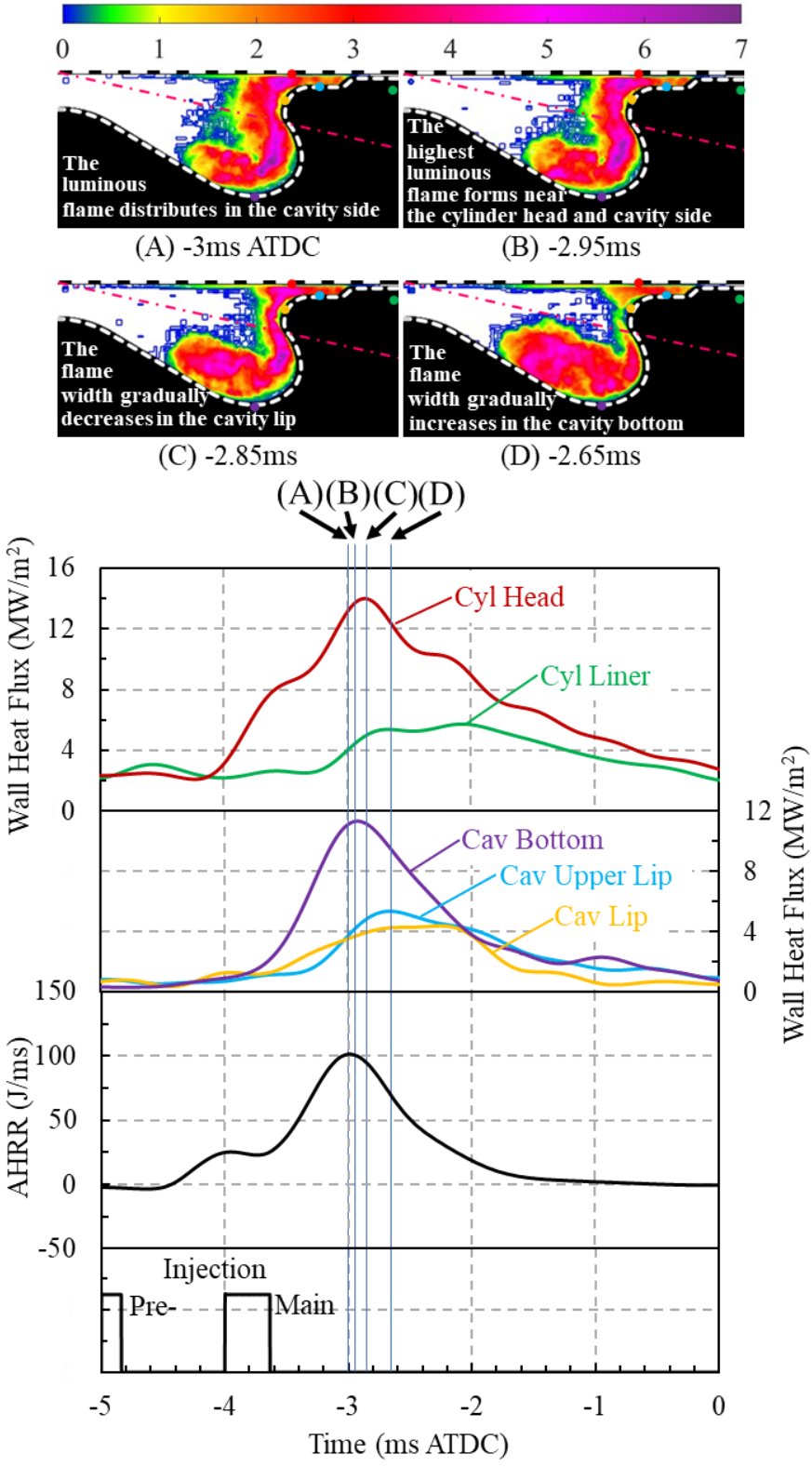

(a) Common rail pressure 75 MPa

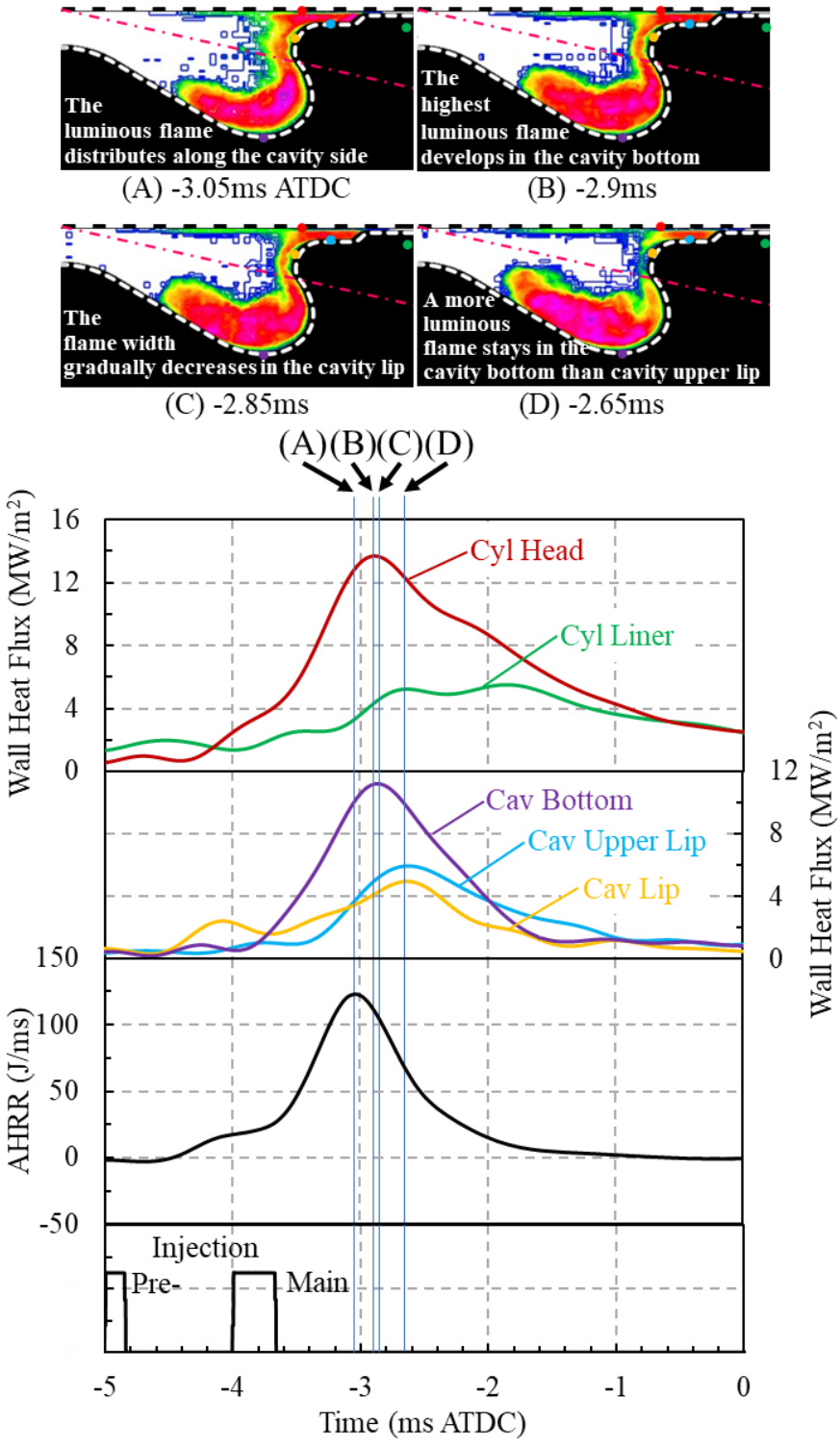
The luminous flame distributes along the cavity side
(A) -3.05ms ATDC
The highest luminous flame develops in the cavity bottom
(B) -2.9ms
The flame width gradually decreases in the cavity lip
(C) -2.85ms
A more luminous flame stays in the cavity bottom than cavity upper lip
(D) -2.65ms
(A)(B)(C)(D)
Wall Heat Flux (MW/m²)
Cyl Head
Cyl Liner
Cav Bottom
Cav Upper Lip
Cav Lip
AHRR (J/ms)
Injection
Pre-
Main
Time (ms ATDC)

(b) 100 MPa

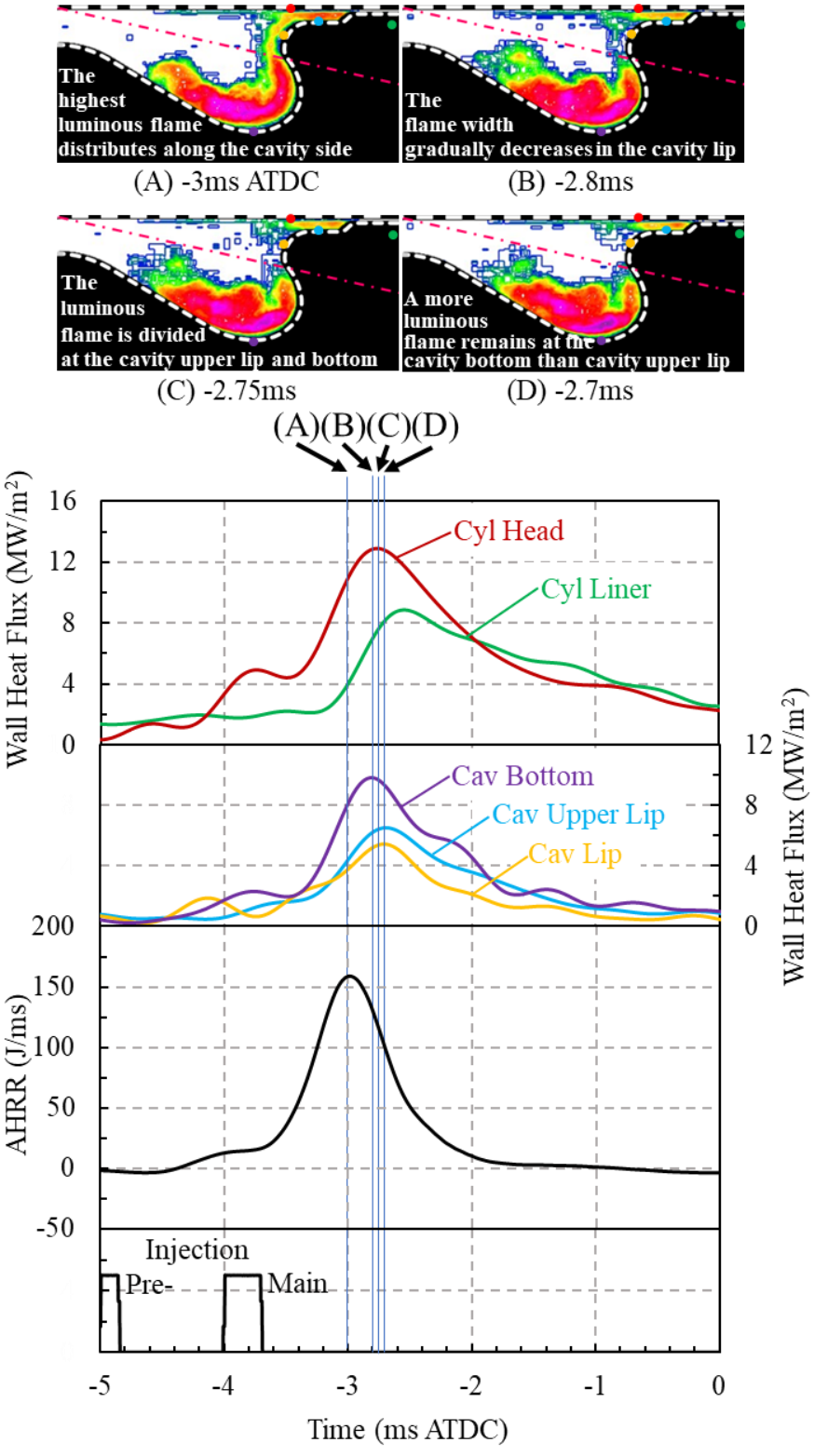
The highest luminous flame distributes along the cavity side
(A) -3ms ATDC
The flame width gradually decreases in the cavity lip
(B) -2.8ms
The luminous flame is divided at the cavity upper lip and bottom
(C) -2.75ms
A more luminous flame remains at the cavity bottom than cavity upper lip
(D) -2.7ms
(A)(B)(C)(D)
Wall Heat Flux (MW/m²)
Cyl Head
Cyl Liner
Cav Bottom
Cav Upper Lip
Cav Lip
AHRR (J/ms)
Injection
Pre-
Main
Time (ms ATDC)

(c) 125 MPa

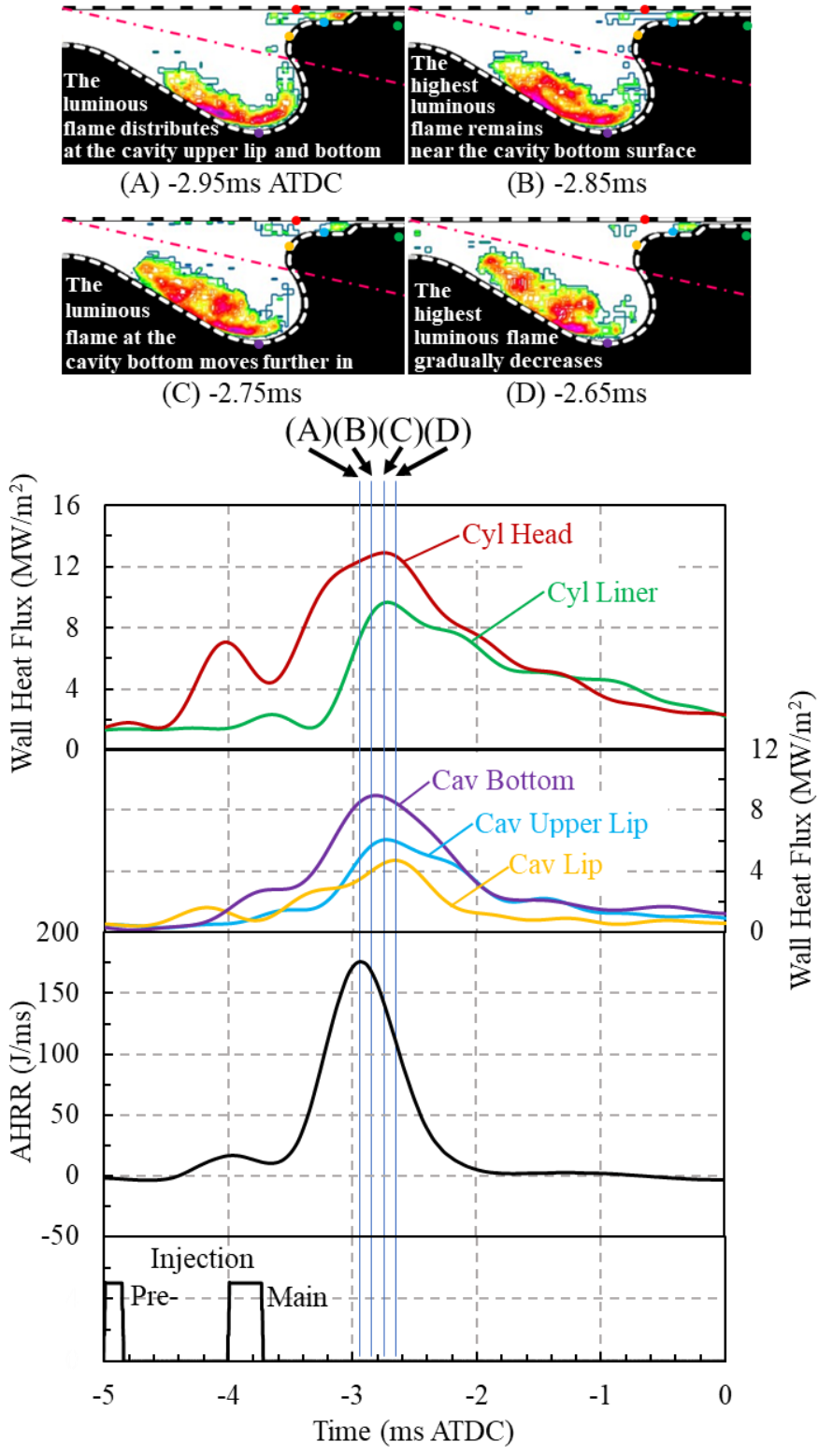

(d) 150 MPa

Figure 4.3 Temporal variations of flame distribution in combustion chamber, apparent heat release rate (AHRR), and wall heat fluxes under common rail pressure variation.

During the pre-injection spray, a high common rail pressure increases the impingement spray, which increases the wall heat flux faster than a low common rail pressure. The peak value of the AHRR is positively correlated with the common rail pressure, as shown in the four panels of Figure 4.3. The wall heat flux of the cavity lip increased significantly after the pre-injection spray at higher common rail pressures, as shown in Figures 4.3 (b), 4.3 (c), and 4.3 (d). The evaporation of the main injection fuel absorbs a significant amount of energy, which decreases the wall heat flux after the main injection spray, as shown in Figures 4.3 (c) and 4.3 (d). In addition, by increasing the common rail pressure, the peak value of the AHRR increased, and the duration of the AHRR peak value decreased. The injection spray arrived first at the cavity lip, which initially contributed to an increase in the wall heat flux in the cavity lip. Furthermore, after spray impingement, the fuel vapor was distributed in the cavity upper lip and cavity bottom spaces. In addition, the wall heat flux in the cavity lip was the lowest owing to the short flame residence time in this region. The wall heat flux of the cylinder liner was lower than that of the cylinder head owing to inadequate space to cover the combustion flame. The second lowest wall heat flux was observed at the cavity upper lip, as there was less space in this region compared to the cavity bottom.

In conclusion, the early pilot injection tended to increase the rich mixture in the cavity upper lip space, thereby increasing the flame residence time in this region. Meanwhile, the heat flux in the cavity upper lip did not significantly increase due to the limited space in this area. Furthermore, the flame appeared in the cavity bottom space with high luminosity, attributed to the adequate space available to accommodate it. Additionally, the normalized image processing was instrumental in investigating the local flame luminosity distribution within the combustion chamber, which appeared primarily along

the cavity side wall.

4.3 FLAME TEMPERATURE AND SOOT DISTRIBUTIONS

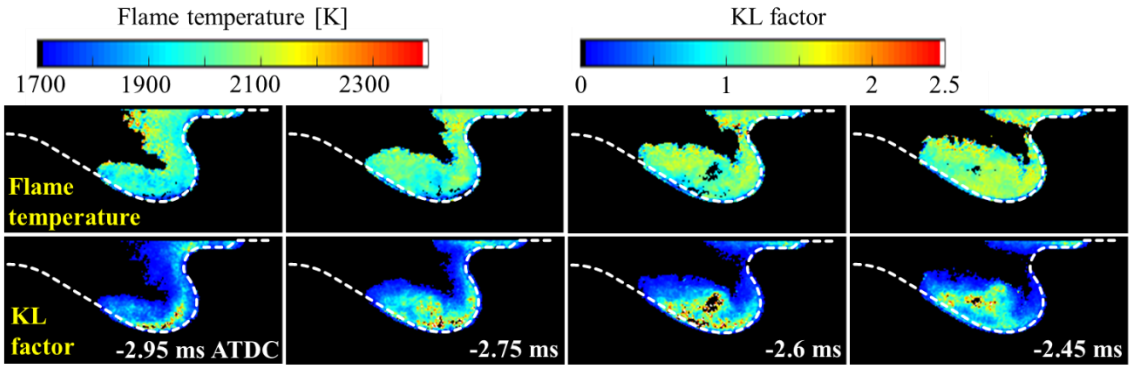

(a) Common rail pressure 75 MPa

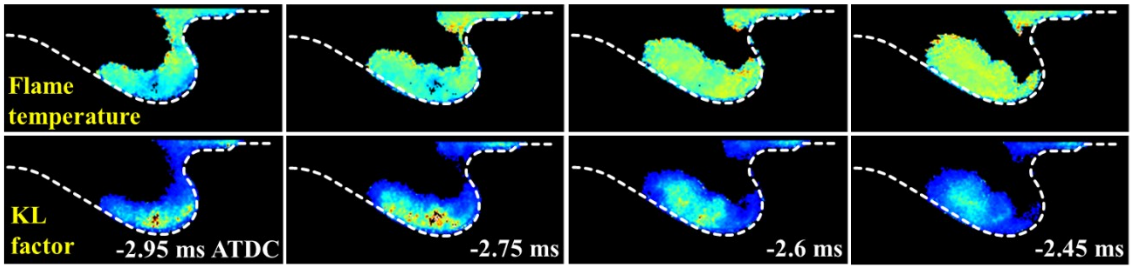

(b) 100 MPa

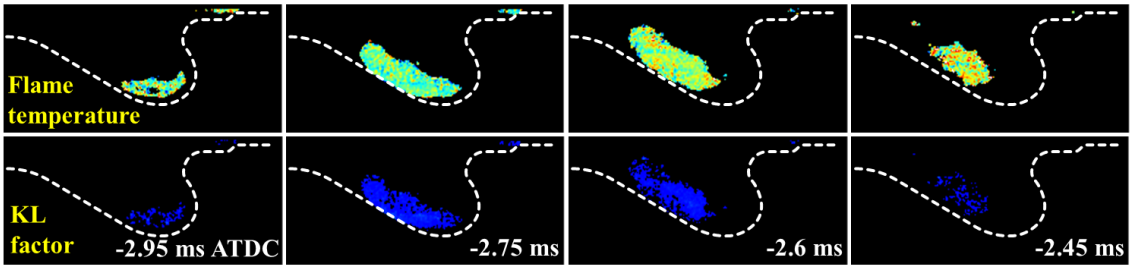

(c) 125 MPa

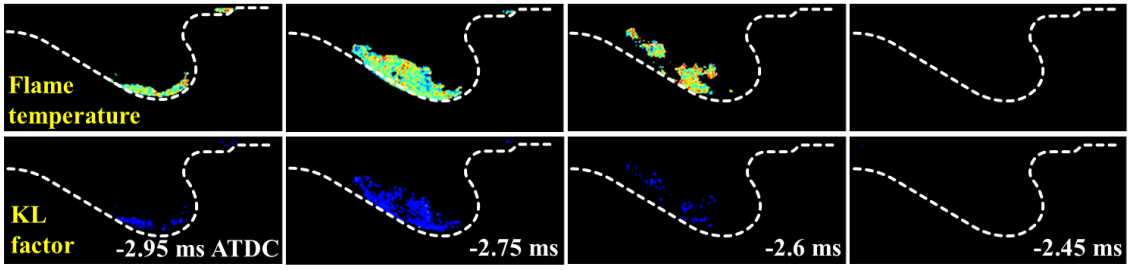

(d) 150 MPa

Figure 4.4 Flame temperature and KL factor distributions under common rail pressure variation.

In diesel combustion, black-body radiation theory is employed to extract radiative heat flow, enabling the determination of flame temperature and the KL factor. To obtain these parameters during the combustion process, a two-color analysis was conducted, as illustrated in Figure 8. The image results from direct photography without backlighting (direct photography) were generated using MATLAB to obtain the flame temperature and KL factor distribution.

Figure 4.4 shows the flame temperature and KL factor obtained at various common rail pressures. We compared the figures at timings ranging from -2.95ms to -2.45ms ATDC. The distributions and shapes of flame temperature and KL factor were similar across these timings, as they were derived from luminous flame images. Spray atomization and air entrainment can be enhanced by increasing the common rail pressure. At lower common rail pressures, the flame temperature and KL factor distribution were higher than those at higher common rail pressures. At lower common rail pressure, we noted an increase in natural luminosity of the flame, which correlates with temperature and soot dispersion. Under these conditions, soot distribution is notably higher due to decreased air entrainment, spray atomization, and fuel-air mixing, resulting in localized high equivalent ratios. This association between elevated temperature and localized high equivalent ratios is frequently linked to soot production. Conversely, natural flame intensity decreases at higher common rail pressure.

The increasing common rail pressure encourages greater air entrainment, improved spray atomization, and enhanced premixing of fuel and air, consequently reducing soot formation. The strongest flame temperature and KL factor distributions were obtained using a common rail pressure 75 MPa, followed by a common rail pressure 100 MPa; the weakest flame temperature and KL factor distributions were obtained using a common

rail pressure 150 MPa. The early pilot effect indicated that the flame remained in the upper lip space at low common rail pressure, as shown in Figures 4.4 (a) and 4.4 (b). A higher common rail pressure increases the spray tip penetration, impingement, and momentum, which enhances the spray atomization, air entrainment, and air-fuel mixture formation. Furthermore, the KL factor can be reduced using a higher common rail pressure. Consequently, the soot emissions were reduced by applying higher common rail pressures at 125 and 150 MPa, as shown in Figures 4.4 (c) and 4.4 (d), respectively.

4.4 ACCUMULATED WALL HEAT FLUX AND SUM OF ACCUMULATED WALL HEAT FLUXES

Figure 4.5 shows a summary of the accumulated wall heat flux from the start of the pilot injection to 6ms ATDC and the sum of the accumulated wall heat fluxes at all locations according to common rail pressure variations at different locations. The accumulated wall heat flux is affected by the wall point measurement location, wall heat flux peak value, flame residence time, and combustion duration. The wall heat flux first increased at different times, depending on the wall heat flux locations after the pre-injection spray. Flame combustion initially occurred after the main injection spray, which increased the wall heat flux. Variations in the common rail pressure significantly influenced the accumulated wall heat flux magnitude at each location. The higher accumulated wall heat flux values at the low common rail pressure can be attributed to the effect of multiple injections, which induce a substantial amount of wall heat flux before the main injection. The relative stability of wall heat flux at higher common rail pressure can be attributed to the fact that the air-fuel mixture possesses greater momentum. Consequently, the spray develops faster and exhibits better evaporation. Moreover, the longer spray tip penetration and wider spray cone angle at a higher common rail pressure,

results in fewer spatial variations in the equivalent ratio. Furthermore, a significant proportion of the total maximum wall heat flux is located at the cylinder head, considering that the ignition first and last ignition locations are nearer to the cylinder head than any other location.

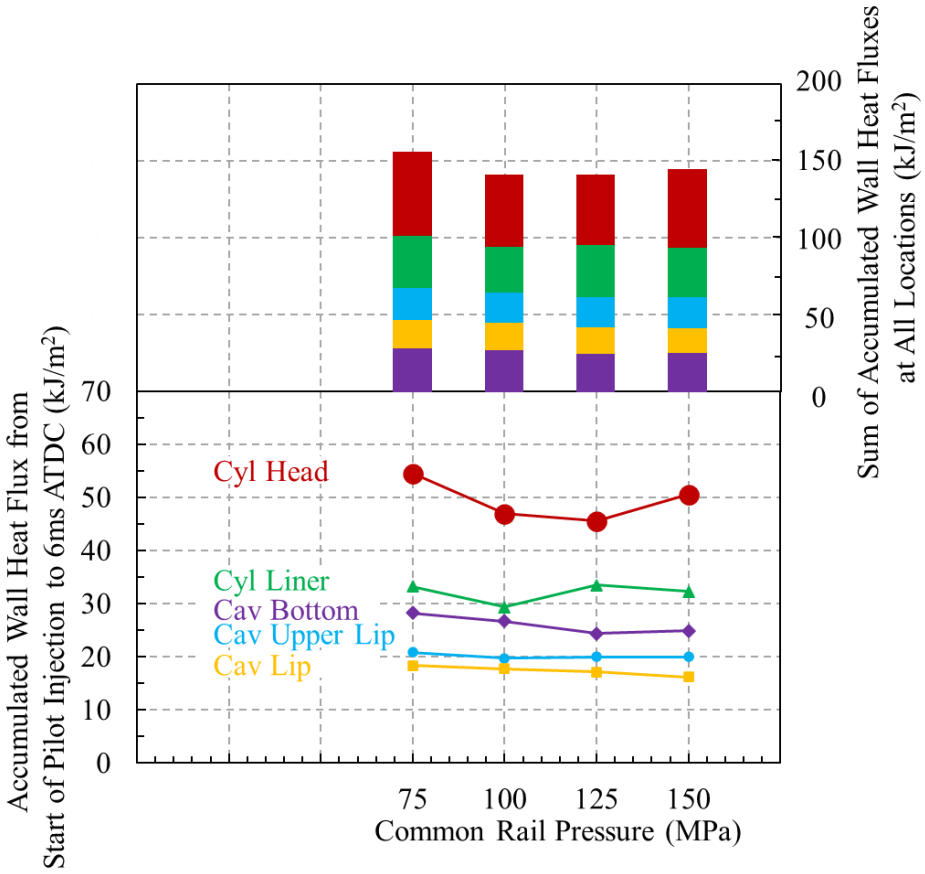

Figure 4.5 Accumulated wall heat flux and sum of accumulated wall heat fluxes under common rail pressures variation.

In addition, after the base condition of the temperature measurement and heat calculation at each location, the cylinder head was found to have the largest accumulated heat flux compared with the other locations. First, the combustion flame occurred along the centerline of the primary spray axis and impinged around the cavity lip and spread out to the combustion chamber. Subsequently, at normal impingement flame was formed after spreading. This condition led to a higher flame temperature and a longer residence time

at the cylinder head. At other locations, both normal and tangential impingements were formed around the cavity lip. Therefore, the cavity and squish zones received a flame spray distribution. Compared with other locations, the collected wall heat flux is the lowest in the squish zone which significantly affects the value of the wall heat flux at the cylinder liner. Typically, the inadequate amount of oxygen prevents the squish zone from receiving considerable heat flux. The squish zone is narrow in space, with insufficient air mixing, resulting in insufficient oxygen, insufficient combustion, and then incomplete heat release.

The accumulated wall heat flux (bottom panel) tended to decrease at higher common rail pressures at the cavity lip, cavity upper lip, and cavity bottom. At the cylinder head, the accumulated wall heat flux was lower at 100/125 MPa and higher at 75/150 MPa. This demonstrates that the accumulated wall heat flux is not only affected by the luminous flame but also by the impingement magnitude [111]. At the cylinder liner, a high common rail pressure tended to increase the accumulated wall heat flux owing to the higher velocity, increasing the amount of combustion flame flowing through the crevice. Furthermore, an increase in the common rail pressure from 75 to 125 MPa reduced the sum of the accumulated wall heat fluxes. Meanwhile, a common rail pressure 150 MPa provided a higher sum of accumulated heat fluxes than a common rail pressure 125 MPa owing to the higher impingement and turbulence, contributing to an increase in the accumulated wall heat flux. The sum of the accumulated wall heat flux ratios at common rail pressures 75, 100, and 150 MPa was approximately 10.43%, 0.01%, and 2.38% greater, respectively, than that at the common rail pressure 125 MPa. In addition, the accumulated wall heat flux ratios of the cylinder head at common rail pressures 75, 100, and 150 MPa were 19.53%, 2.96%, and 10.79% greater, respectively, than that at the

common rail pressure 125 MPa.

4.5 SUMMARY

In this chapter, we presented the effects of common rail pressures using a two-hole injector. We investigated common rail pressures 75, 100, 125, and 150 MPa to study their impact on wall heat flux characteristics and spray flame behavior in the combustion chamber. Normalized spray flame images were utilized to understand the local luminous flame distribution within the combustion chamber. The results show that the luminous flame appears only after the main injection spray. The early pilot injection tends to form a rich mixture in the cavity upper lip area. Consequently, the luminous flame is observed primarily on the cavity side wall, and the flame persists for the longest time in the cavity upper lip space due to the rich mixture formed by the pilot injection spray.

At low common rail pressures, a rich mixture tends to form, resulting in a stronger luminous flame compared to higher common rail pressures. The wall heat flux at the cylinder head is the highest among all locations because the high-intensity luminous flame persists in this region for a longer duration. Additionally, the high temperature of the oil chiller flowing through the interior of the cylinder head and liner further contributes to the increased wall heat flux in the cylinder head. Conversely, the wall heat flux of the cylinder liner is relatively low due to the limited space available for the luminous flame to propagate.

Additionally, flame temperature and KL factor distributions were analyzed using two-color pyrometry. The results indicated that a higher common rail pressures tend to increase the peak wall heat flux and reduce the luminous flame distribution within the combustion chamber. The KL factor was also reduced with higher common rail pressures, leading to lower soot generation. Furthermore, higher common rail pressures increased

the peak wall heat flux and combustion duration, which, in turn, affected the accumulated wall heat flux. As a result, the accumulated wall heat flux and the total sum of accumulated wall heat flux are lowest at a common rail pressure 125 MPa compared to other pressures. At a common rail pressure 150 MPa, the spray velocity is the highest, resulting in more turbulent flows. Consequently, the common rail pressure 150 MPa leads to a higher accumulated wall heat flux and a greater total sum of accumulated wall heat flux.

CHAPTER 5 EFFECT OF NUMBER OF HOLES INJECTOR ON WALL HEAT FLUX CHARACTERSITIC AND SPRAY FLAME BEHAVIOR

This study was conducted using three different injections: pilot, pre-, and main. Three variations of the common rail pressure were also used: 30, 120, and 180 MPa, and the movement of the piston and cam was measured using a laser sensor (LK-G405, Keyence). Furthermore, a piezoelectric pressure sensor was set up on the cylinder head to record the change in pressure, while the ambient temperature was measured using a K-type thermocouple. The engine speed was simulated to remain constant at 525 rpm, and the total injected fuel mass was 16 mg. The pilot injection spray was injected at early time -7.6ms ATDC to enhance the local homogeneous mixture formation [112] [113] [114]. The pre-injection spray was injected at -1.8ms ATDC to enhanced fuel atomization and air fuel mixture formation. Then, the main injection spray was injected at 0.7ms ATDC. Meanwhile, we used the compression ratio at 14.5, same as the two-holes case. The target speed engine in these experiments is 525 rpm. Furthermore, we obtained the accumulated pressure at 0.294 MPa using motoring test condition. The polytrope index is obtained at 1.27 from calculation after input the measurement result of experiment. To understand the injection rate in more detail, Figure 5.1 was used. we utilized the Zeuch method to measure the injection rate. Subsequently, the detailed size of the piston cavity and motoring test results were reported [43] [15], and the injection rate, which was based on the variation in common rail pressure conditions, is shown in Figure 5.1. The spray characteristics and combustion process were investigated using common rail pressures of 30, 120, and 180 MPa. Finally, the injection timing was determined to be shorter at a higher common rail pressure. Table 5.1 presents the details of the experimental conditions.

Table 5.1 Experimental conditions

Parameters	**Value**			
Fuel Injection				
Fuel	JIS#2 Diesel			
Common rail pressure P_{rail} [MPa]	30, 120, and 180			
Injector hole diameter [mm]	0.106			
Number of injector holes	3 x 2 (3 left and 3 right)			
Umbrella Angle [deg.]	155			
Split injection stage	Total	Pilot	Pre	Main
Injection timing [ms ATDC]		-7.6	-1.8	0.7
Injection amount [mg]	16.00	4.00	0.80	11.20
Injection amount per hole [mg]	2.67	0.67	0.13	1.87
Combustion Chamber				
Piston cavity	Stepped piston cavity			
Compression ratio	14.5			
Intake gas	18% O_2 + 82% N_2			
Ambient pressure at TDC [MPa]	6.44 (Motoring)			
Ambient temperature at TDC [K]	670 (Motoring)			
Oil chiller temperature [K]	363			
Cylinder head temperature [K]	400			
RCEM Operation				
Simulated engine speed [rpm]	525			
Accumulated pressure [MPa]	0.294			
Polytrope index	n = 1.27			

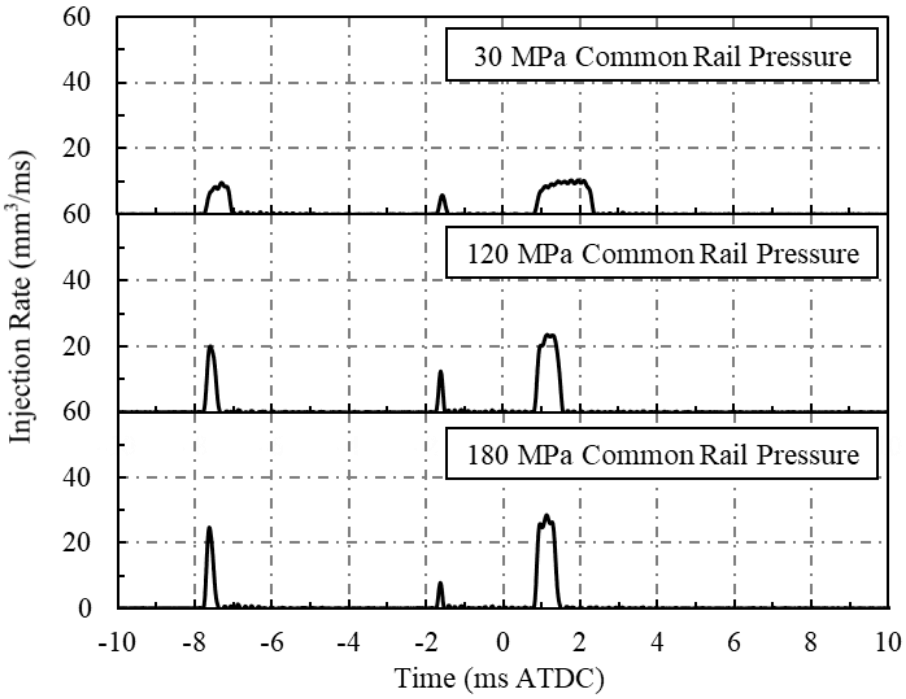

Figure 5.1 Injection rates under different common rails pressure

Spray and flame behavior during RCEM operation were visualized using a high-speed video camera equipped with a 200 mm focal length lens and capable of recording at 20,000 frames per second (fps). The camera had an exposure time of 5 μs and an image resolution of 1024×512 pixels. Direct photography was employed to accurately capture the flame behavior during the ignition process. The space windows on the combustion lateral side measured 86×30 mm (length×width). The high-speed video camera was connected to the image acquisition PC as presented in this study. The injector featured 3 holes angled to the left and another 3 holes to the right, simulating spray interaction in a 10-hole injector combustion system typical of actual diesel engines. Each hole had a diameter of 0.106 mm. In this experiment, we used the direct photography method to obtain flame images with minimal saturation, which served as raw images for subsequent image processing. In addition, the injector has three-holes with the neighboring angle in the left direction and other three-holes in the right direction to simulate the spray

interaction in the ten-holes injector combustion system in the actual diesel engine. The phenomena of spray interaction between the fuel from one hole to others was considered to apply this condition instead of 1-holes injector in the left and right side, respectively. In addition, the combustion process was captured using a high-speed color video camera, and the results were processed using an image acquisition PC. The capture results are presented in this study. The optical arrangement of direct photography is given in Figure 5.2.

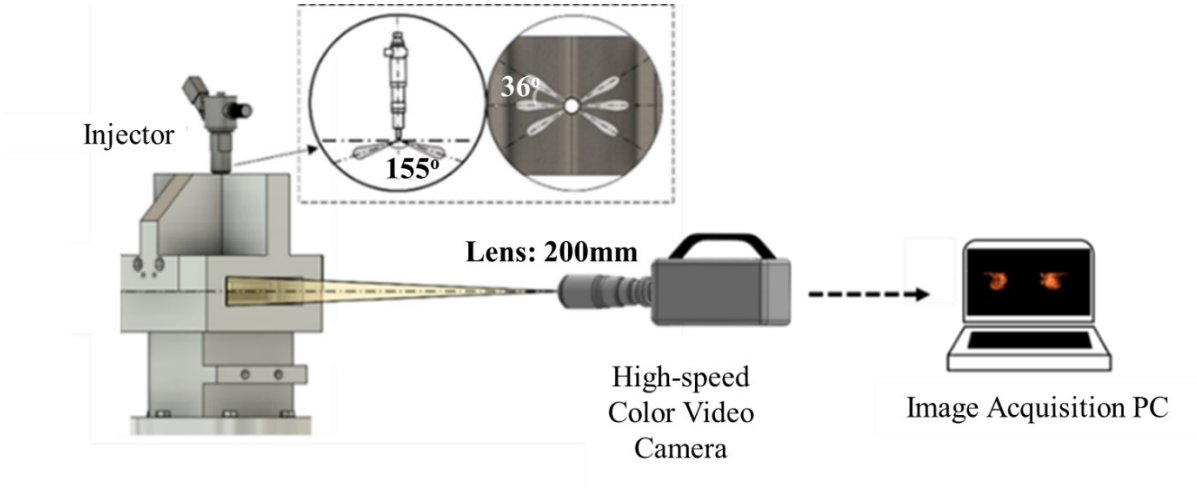

Figure 5.2 Optical arrangement of direct photograph (DP) method.

5.1 OVERALL RESULT UNDER COMMON RAIL PRESSURE CONDITION VARIATION

In this experiment, we used triple injection strategy: pilot, pre-, and main injection spray. The amounts of diesel fuel used in the pilot, pre-injection, and main injection sprays were 3.964, 0.747, and 11.205 mg, respectively. Variations in common rail pressure conditions (30, 120, and 180 MPa) were applied to properly investigate spray evaporation, air-fuel mixture formation, and heat transfer in the combustion chamber.

5.1.1 Characteristics of Combustion under Common Rail Pressure 30 MPa

The distribution of the Apparent Heat Release Rate, in-cylinder pressure, and ambient temperature were acquired, as shown in Figure 5.3, and the maximum value of the AHRR was obtained just after the end of the main injection. The measurements show that the AHRR exhibited an increasing trend during the main injection. As a result of the main flame that occurred after the pilot, pre-, and main combustion. The pilot injection spray/vapor forms a rich mixture near the injector and penetrates following the primary spray axis to the cavity lip regions. The pre-ignition flame appears for a short duration due to the small injection amount used in this experiment. The combustion duration during the pilot ignition flame is longer than that of the pre-ignition flame but shorter than the main ignition flame. The ignition flame appears after each injection spray at a common rail pressure 30 MPa. Low common rail pressure 30 MPa tends to result in lower velocity fuel spray penetration, which contributes to the formation of a rich mixture near the injector holes due to spray-to-spray interaction in this region. Additionally, the ignition flame appears after each spray: pilot, pre-, and main injection when using a common rail pressure 30 MPa. The fuel evaporation process absorbs high energy in ambient air, which decreases the AHRR; however, it increases during combustion. During the compression stroke, the in-cylinder pressure and ambient temperature increased before pre-injection and tended to remain constant between pre-injection and main injection. During the expansion stroke, the in-cylinder pressure and temperature increased significantly during the main injection. The AHRR increases owing to the relatively constant volume and higher in-cylinder pressure gradient after the TDC. However, the volume distribution tends to be constant during the AHRR, which does not significantly contribute to the AHRR distribution.

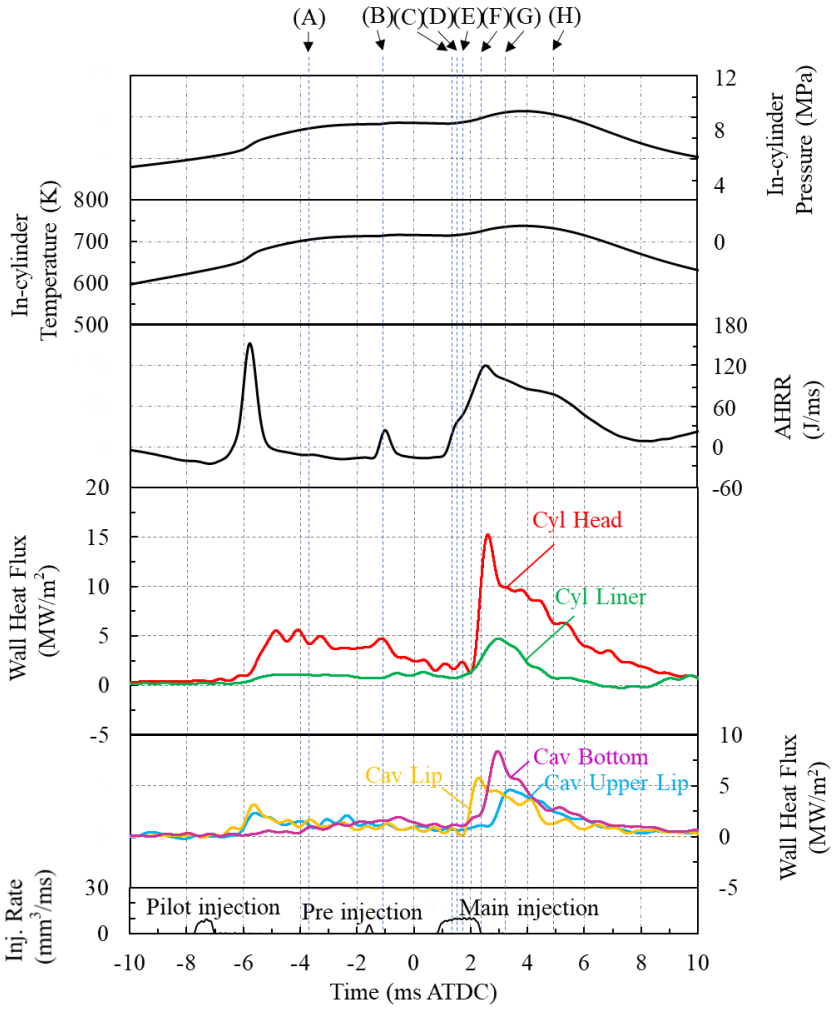

Figure 5.3 In-cylinder pressure, in-cylinder temperature, apparent heat release rate, and wall heat fluxes under common rail pressure 30 MPa.

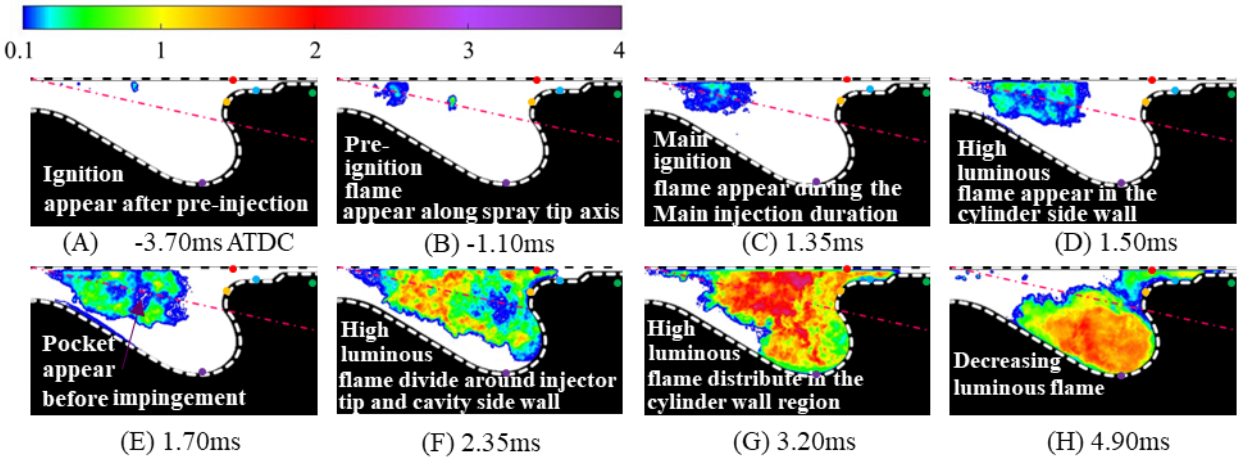

Figure 5.4 Temporal variations of normalizing flame distributions in combustion chamber under common rail pressure 30 MPa.

The heat flux at the piston cavity varies because the spray flame starts earlier in the cavity lip, in accordance with equations $(2.1) - (2.3)$. In other words, the heat flux in the piston cavity indicates that ignition flame initially arrives in the cavity lip region, and subsequently at the upper lip and bottom of the cavity owing to the convective effect. Meanwhile, the heat flux distribution values in the cylinder also varies, as shown in Figures 5.3. The maximum value of the heat flux in the cylinder is obtained at the cylinder head after the main injection because the combustion flame occurs along the centerline of the primary spray axis and then spreads around the cylinder head region. The cylinder head's temperature is, thus, at its highest, which is a result of the longer residence of the flame near the cylinder head than at other local heat flux locations. Furthermore, after impingement, fuel spray evaporation is distributed on the cavity and squish zones, which induces substantial heat in the cavity zone, while the squish zone has some space to accommodate the fuel mixture and combustion flame. The magnitudes of the heat flux at the cylinder liner and cylinder head are influenced by the squish zone and cavity zone, respectively. The overall heat flux is influenced by flame temperature, flame resident time, spray tip penetration, and impingement.

Figure 5.4 shows the characteristics of the spray and flame behavior on the wall heat flux in the cavity and cylinder sides at a common rail pressure 30 MPa. The strong air entrainment was observed to fill the combustion chamber at high temperatures. The pilot injection spray flows through the primary spray axis and first arrives at the cavity lip, which contributes to an increase in the heat flux. Subsequently, the flow continues on to the cavity upper lip and cylinder head. Natural flame combustion occurs at the beginning of the main injection and then develops by following the spray from the surrounding of injector to the cavity side wall. The pilot fuel injection penetrates the combustion chamber and forms rich mixtures. The pilot ignition flame then appears later, following an increase

in-cylinder temperature during the compression stroke. Furthermore, a low luminous flame appears near the cylinder head surface and increases the wall heat flux at cylinder head more than other locations, as shown in Figure 5.4 (A). Meanwhile, the wall heat flux at the cavity lip and upper lip also increases slightly. The pre-injection spray also contributes to the occurrence of the ignition flame, which increases the wall heat flux specifically at the cylinder head, as shown in Figure 5.4 (B). The high in-cylinder temperature of the combustion chamber, caused by previous ignitions, tends to increase, leading to higher overall temperatures. The pilot injection spray/vapor fills the combustion chamber and forms a rich mixture at a high temperature, resulting in a larger pre-ignition flame compared to the pilot ignition flame. The main injection spray occurs near TDC where the in-cylinder temperature is the highest. The main ignition flame appears near the injector tip and develops along the primary spray axis, as shown in Figures 5.4 (C)-(E). The high luminous flame is distributed near the injector tip and along the cavity side wall, as shown in Figure 5.4 (F). The ignition flame impinges on the cavity lip, splitting into the cavity upper lip and bottom space, which increases the wall heat flux in the cavity upper lip, lip, and bottom. The ignition flame also distributes to the cavity side wall, as shown in Figure 5.4 (G). Meanwhile, the high temperature of oil chiller flow on the cylinder head and liner surfaces contributes to the highest wall heat flux value on the cylinder head. In the cylinder liner, the wall heat flux is lower than in the cylinder head because the flame does not reach this location due to the limited space. Furthermore, the luminous flame decreases over time, as shown in Figure 5.4 (H). This mechanism improves the intake of unmixed air and rich mixtures and promotes the use of burning and unburning gases.

5.1.2 Characteristics of Combustion under Common Rail Pressure 120 MPa

In a higher common rail pressure 120 MPa, the luminous flame is reduced due to the better evaporation. The combustion duration, flame timing, and wall contact area are important factors influencing the heat transfer from the piston cavity and cylinder wall. The ignition delay and combustion duration are effectively shortened by increasing the common rail pressure for better spray evaporation and a uniform air-fuel mixture. Figure 5.5 presents the in-cylinder pressure, in-cylinder temperature, apparent heat release rate (AHRR), wall heat flux, and injection rate under a common rail pressure 120 MPa. The in-cylinder pressure and temperature slightly increase during the compression stroke and tend to stabilize near top dead center (TDC). After the main injection, both parameters significantly increase to their peak values and then gradually decrease.

Figure 5.6 shows the temporal variations of normalized flame distribution under a common rail pressure 120 MPa. The apparent heat release rate (AHRR) is reduced after pilot and pre-injection sprays at 120 MPa compared to 30 MPa, as illustrated in Figures 5.3 and 5.5. The luminous flame does not appear after the pilot injection spray due to the formation of an enhanced lean mixture, which reduces the likelihood of its occurrence. Meanwhile, the AHRR increases slightly after the pilot injection spray, even though no luminous flame is observed. Furthermore, the pre-injection spray is introduced into a region of higher in-cylinder temperature and pressure during the compression stroke, generating turbulent flow with a small amount of injected fuel which produced low luminous flame near the injector tip. This results in a small luminous flame near the injector tip, as shown in Figure 5.6 (A). An intense ignition flame occurs after the main injection spray, extending from the primary spray axis to the injector tip, as seen in Figure 5.6 (B).

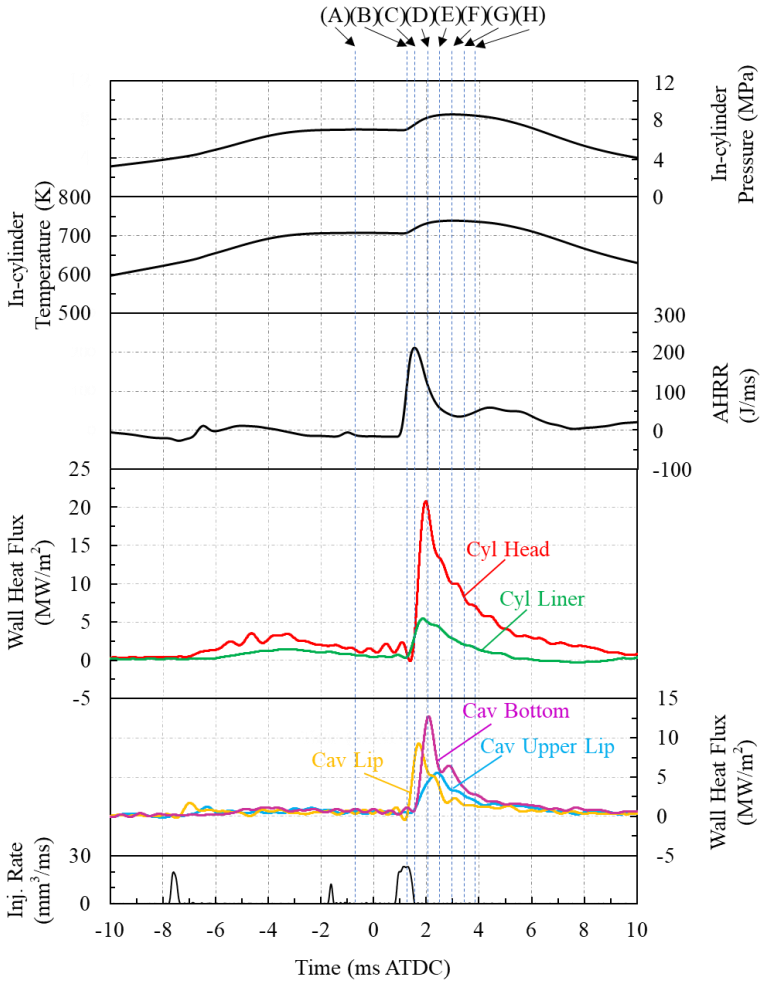

Figure 5.5 In-cylinder pressure, in-cylinder temperature, apparent heat release rate, and wall heat fluxes under common rail pressure 120 MPa.

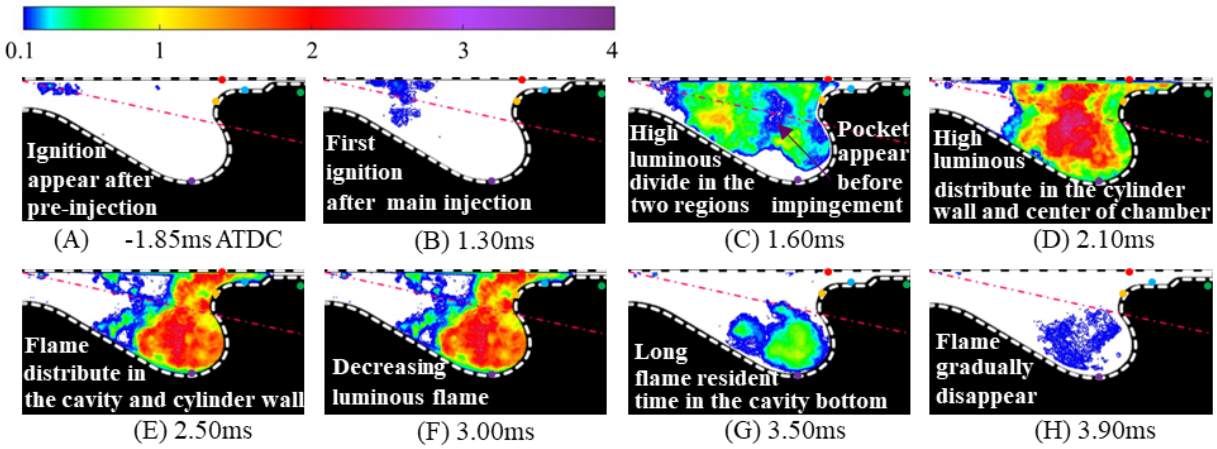

Figure 5.6 Temporal variations of normalizing flame distributions in combustion chamber under common rail pressure 120 MPa

At a common rail pressure 120 MPa, the AHRR increases significantly more than at 30 MPa, while the duration of the AHRR is reduced. The luminous flame first appears at the cavity lip and then spreads to the cavity side wall and near the injector tip, as depicted in Figure 5.6 (C). The luminous flame forms along the primary spray axis due to spray-to-spray interactions from each injector hole, creating a pocket in the center of the luminous flame before fuel impingement. This pocket gradually disappears after impingement, leading to the highest luminous flame on the cylinder head surface and at the center of the luminous flame, as illustrated in Figure 5.6 (D). Consequently, the peak wall heat flux in the cylinder head is the highest, as shown in Figure 5.5. Additionally, the high oil chiller temperature flowing inside the cylinder contributes to increasing the wall heat flux on the cylinder side. After impingement, the more luminous flame distributes to the cavity bottom space rather than the cavity upper lip space, where it remains for a prolonged period, as shown in Figures 5.6 (E)-(H). Furthermore, the peak wall heat flux in the cavity bottom is the second highest and the longest flame residence time, as depicted in Figure 5.5. The space at the cylinder liner is insufficient to effectively convey fuel at a common rail pressure 120 MPa, and the cylinder liner lacks adequate oxygen access, resulting in limited heat flux at this location. Additionally, the 120 MPa common rail pressure leads to a shorter combustion duration due to better lean mixture formation compared to 30 MPa, as shown in Figures 5.6 (A)-(H) and 5.4 (A)-(H).

5.1.3 Characteristics of Combustion under Common Rail Pressure 180 MPa

At the highest common rail pressure 180 MPa, the in-cylinder pressure and temperature do not significantly differ before the main injection spray. However, the gradient of in-cylinder pressure and temperature increases more due to better lean mixture formation compared to common rail pressures of 30 MPa and 120 MPa, as shown in

Figure 5.7. After the main injection spray, the peak value of the apparent heat release rate significantly increases, while the duration of the AHRR significantly decreases, indicating a reduced combustion duration with the highest common rail pressure. The luminous flame of the main combustion spray occurs after impingement spray. The highest common rail pressure enhances lean mixture formation and increases the ignition delay which starts the ignition before impingement. The air-fuel mixture becomes more homogeneous, leading to more complete combustion. Consequently, combustion efficiency is improved, and unburned hydrocarbons are reduced. The high velocity resulting from the high common rail pressure forms more turbulence and increases the peak value of the AHRR. Conversely, the peak value of the AHRR after pilot and pre-injection sprays is the lowest compared to the lower common rail pressures of 30 MPa and 120 MPa. The high common rail pressure effectively enhances lean mixture formation, thereby reducing the combustion duration. This condition affects the wall heat flux distribution at the cylinder and cavity sides, which exhibit higher peak values than at the lower common rail pressures of 30 MPa and 120 MPa, due to the higher velocities induced by increased common rail pressure, as shown in Figure 5.7. These higher velocities lead to an earlier flow of combustion gases toward the cavity side, which is evidenced by the earlier increase in local heat flux in the cavity region. Additionally, the heat flux distribution in the piston cavity varies, as indicated in Figure 5.7, and was calculated using equations (2.1) - (2.3). In the cylinder region, two heat flux sensors were installed to measure the temperature and obtain the heat flux distribution. The measurements indicate that the heat flux originates predominantly from the cylinder head rather than the cylinder liner, due to the combustion along the centerline of the primary spray axis that spreads out near the cylinder head region.

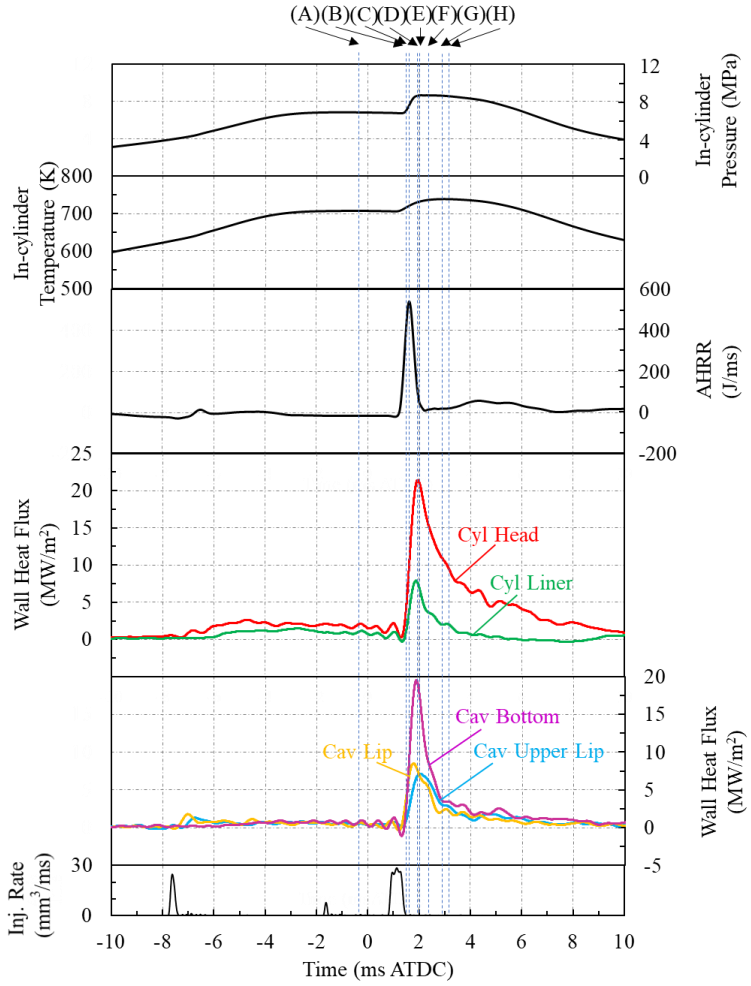

Figure 5.7 In-cylinder pressure, in-cylinder temperature, apparent heat release rate, and wall heat fluxes under common rail pressure 180 MPa.

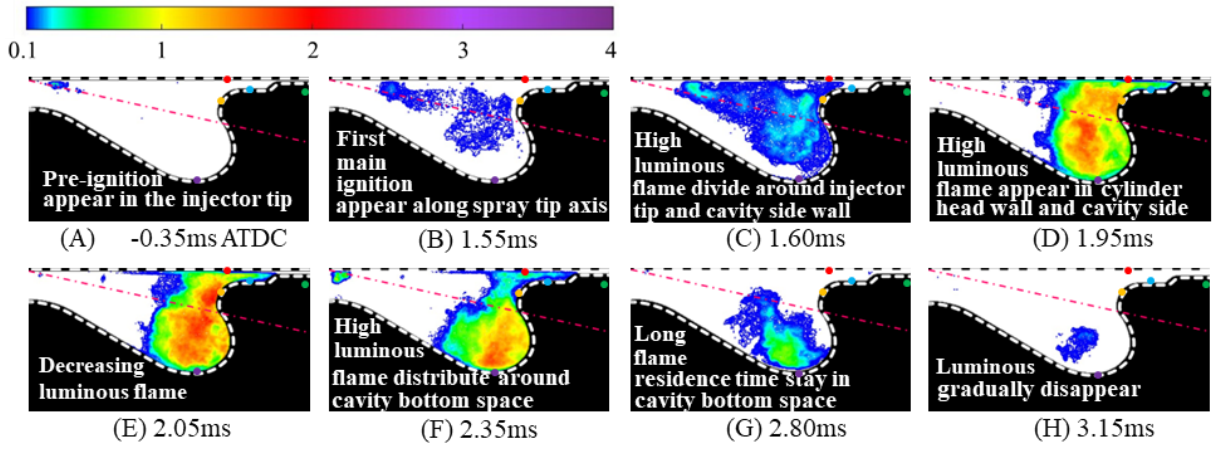

Figure 5.8 Temporal variations of normalizing flame distributions in combustion chamber under common rail pressure 180 MPa

Figure 5.8 shows the temporal variations of normalized flame distributions under a common rail pressure 180 MPa. The pilot injection spray does not result in a luminous flame. Meanwhile, the apparent heat release rate and wall heat flux increase after the pilot injection spray. This increase is lower than that observed at common rail pressures of 30 MPa and 120 MPa. After the pre-injection spray, a small luminous flame appears near the injector, as shown in Figure 5.8 (A). This causes an increase in the wall heat flux at the cylinder head. The luminous flame becomes more prominent after the main injection spray. The relative stability of wall heat flux at high common rail pressure can be attributed to the fact that the air-fuel mixture possesses greater momentum at higher common rail pressure. Consequently, the spray develops faster and exhibits better evaporation. Moreover, the longer spray tip penetration and wider spray cone angle result in fewer spatial variations in the equivalence ratio. Furthermore, a significant proportion of the total maximum wall heat flux is located at the cylinder head, considering that the initial and final ignition locations are nearer to the cylinder head than any other location. Meanwhile, this occurs after impingement, which indicates that the ignition delay increases, as shown in Figure 5.8 (B). Additionally, the combustion duration is reduced, and the peak values of the AHRR and wall heat flux increase. At the end of injection, the luminous flame distributes along the cavity side wall and near the injector tip, as shown in Figure 5.8 (C). Then, it flows to the cavity upper lip and bottom space after impinging on the cavity lip, as shown in Figures 5.8 (D) – (H). Furthermore, the main combustion duration is significantly reduced, as shown in Figures 5.8 (B) – (H).

5.1 FLAME TEMPERATURE AND KL DISTRIBUTIONS UNDER COMMON RAIL PRESSURE VARIATION

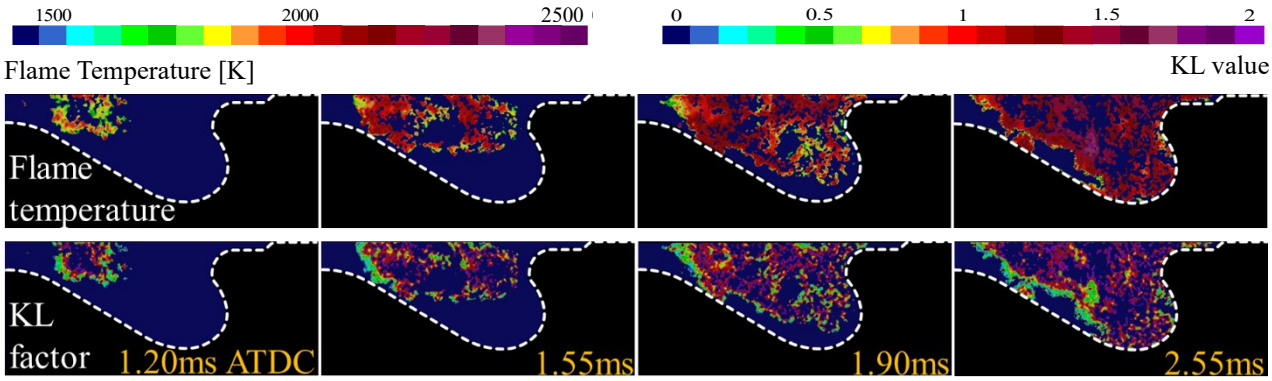

(a) 30 MPa

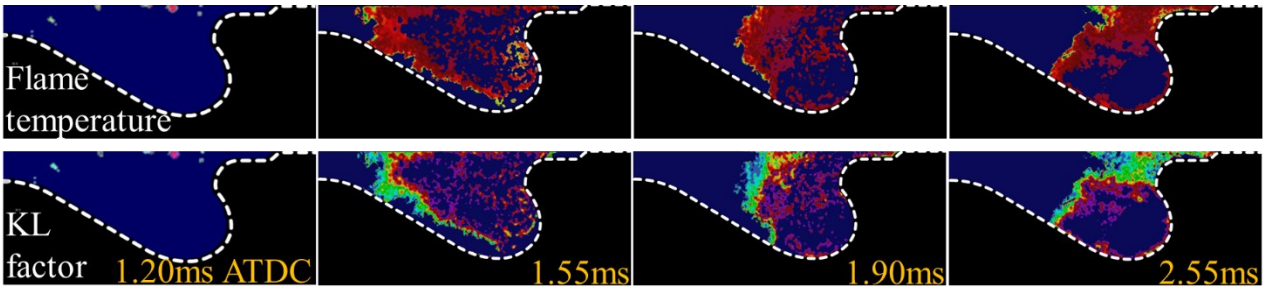

(b) 120 MPa

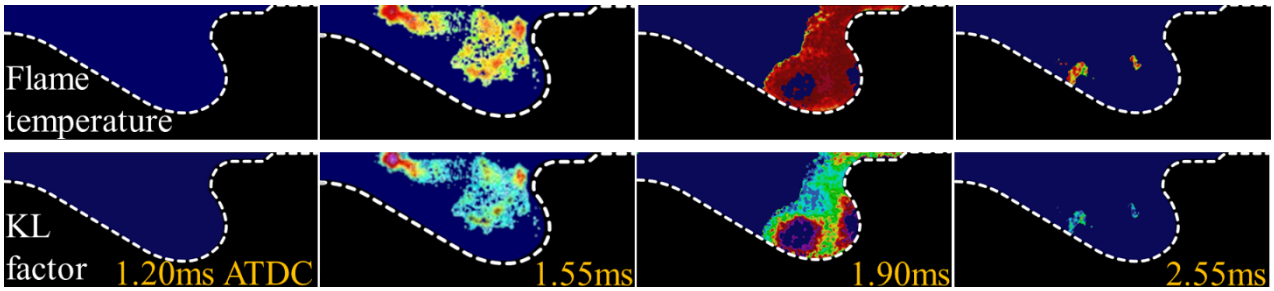

(c) 180 MPa

Figure 5.9 Flame temperature and KL factor distributions under common rail pressure variation.

To obtain the KL factor and local temperature in the combustion chamber, a two-color analysis was performed as shown in Figure 5.9. MATLAB code was used to analyze the raw images from direct photographs. At a low common rail pressure 30 MPa, the

luminous flame is present from 1.10 ms ATDC up to 9.40 ms ATDC. At a common rail pressure 120 MPa, the flame is present from 1.2 ms ATDC up to 5.2 ms ATDC. A higher common rail pressure enhances spray atomization, fuel evaporation, air entrainment, and air-fuel mixing, which decreases the ignition duration to a range of 1.35 ms ATDC up to 3.2 ms ATDC at a common rail pressure 180 MPa. The flame temperature ranges between 1600 K and 2500 K, and the KL factor varies between 0 and 2. From the image analysis, it is observed that the flame area at a common rail pressure 180 MPa is reduced compared to the common rail pressures 30 MPa and 120 MPa, as shown in Figures 5.9 (a), 5.9 (b), and 5.9 (c). Furthermore, the gas temperature and KL factor at a common rail pressure 180 MPa are lower than those at 30 MPa and 120 MPa, contributing to reduced soot generation after the main combustion. The flame temperature is used to obtain the correlation between the Nusselt number and the Reynolds number.

5.2 ACCUMULATED WALL HEAT FLUX AND SUM OF ACCUMULATED WALL HEAT FLUXES

Figure 5.10 shows the summary of the accumulated wall heat flux and sum of accumulated wall heat flux from start of -10ms to 10ms ATDC under common rail pressure variation. The intense spray and flame occurred from the beginning of pilot injection which increased the wall heat flux, and it finished around 10ms ATDC. It affects to the wall heat flux measurement which tends to be constant after 10ms ATDC. In this study, three common rail pressures were used: 30 MPa, 120 MPa, and 180 MPa. They represent measurement location at cylinder head, cylinder liner, cavity upper lip, cavity lip, and cavity bottom, which are marked in red, green, light blue, yellow, and purple, respectively. The accumulated wall heat flux was calculated based on the wall heat flux magnitude and the residence time of the flame at each location.

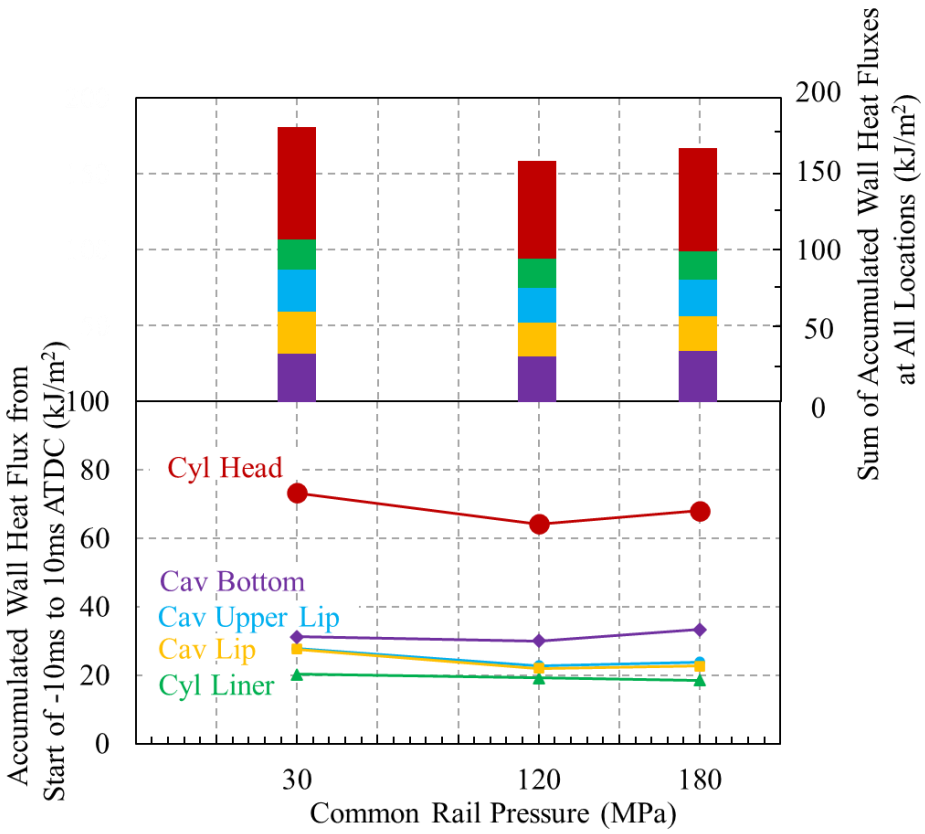

Figure 5.10 Accumulated wall heat flux and sum of accumulated wall heat fluxes under common rail pressures variation.

A higher common rail pressure enhanced spray atomization, fuel evaporation, air entrainment, and air-fuel mixture formation. It also increased the velocity momentum and spray tip penetration and reduced the ignition timing. Moreover, air entrainment significantly affects air–fuel mixture formation. When the entrainment was extremely high, a lean mixture was formed at a lower combustion temperature; however, a higher flame temperature was achieved when a strong air–fuel mixture was formed. In certain studies, a higher common rail pressure was reported to increase spray atomization, which contributed to the larger heat. In contrast, the lowest common rail pressure 30 MPa increased the accumulated wall heat flux at almost all the locations because the ignition occurred after pilot injection and the spray flame remained in the combustion chamber

for longer time.

As shown in Figure 5.10, the cavity bottom exhibits a relatively different behavior owing to the lower combustion duration and low magnitude of the spray flame, which has already been illustrated in Figures 5.3, 5.5, and 5.7. At a common rail pressure 120 MPa, the accumulated wall heat transfer was low at all locations, except for the cylinder liner, which receives inadequate oxygen. It means that the longer spray flame tip penetration affects better evaporation compared to the common rail pressure 30 MPa and has no significant spray flame tip penetration change compared to the common rail pressure 180 MPa. For common rail pressure 180 MPa case, the high common rail pressure tends to give high spray flame velocity and more turbulence flow that contributes to the higher magnitude of wall heat flux. This condition shows that accumulated heat flux not only depends on spreading flame, but also depends on the spray flame velocity. The cylinder head contributes more to the accumulated wall heat flux at the common rail pressures 30 and 180 MPa compared with the common rail pressure 120 MPa. The accumulated wall heat flux ration at the common rail pressure 30 and 180 MPa conditions were approximately 14% and 6% greater than that at the common rail pressure 120 MPa in the cylinder head, respectively as shown in Figure 5.10. The accumulated wall heat flux ratio is a comparison between common rail pressure 30 and 180 MPa to the common rail pressure 120 MPa. A high common rail pressure caused longer spray tip penetration after impingement. This condition shows that the accumulated heat transfer is not only caused by the spreading of the flame temperature but also by the spray flame velocity which results in more turbulence flow and increases the heat.

5.3 EFFECT OF NUMBER OF HOLES INJECTOR ON THE PEAK VALUE OF HEAT FLUX AND THE SPRAY FLAME TIP PENETRATION

The design and functionality of injector holes in diesel engines are pivotal to their performance, efficiency, and environmental impact. As technology advances, optimizing injector holes remains a critical area of research and development. Enhancing fuel atomization, improving combustion efficiency, and reducing emissions through injector hole design significantly contribute to the ongoing evolution of diesel engine technology, meeting the demands for higher performance and reduced environmental impact. In this section, we investigate the effect of the number of holes on the peak value of heat flux, which influences thermal efficiency.

In this part, we compare the maximum wall heat flux during the combustion process using two-hole and six-hole injectors, as shown in Figure 5.11. For the two-hole injector, the ignition flame appears later after the main injection spray, causing the wall heat flux to increase simultaneously at all locations. The earlier pilot injection spray continues to form a rich mixture at the cavity upper lip, resulting in the longest flame residence time in the cavity upper lip space. Consequently, the wall heat flux at the cavity upper lip using the two-hole injector is higher than with the six-hole injector. Additionally, at the cylinder liner, the wall heat flux is higher because it connects to the cavity upper lip space. In contrast, with the six-hole injector, the ignition flame appears first during the main injection spray along the primary spray axis, reaching the cavity lip early. Consequently, the wall heat flux at the cavity lip increases earlier than at other locations, followed sequentially by the cylinder head, cavity upper lip, and cavity bottom. The two-hole injector has one hole on each side, while the six-hole injector has three holes on each side. The total injection amount for the six-hole injector is 4.6 times that of the two-hole

injector. We then compare the maximum peak values of wall heat flux. The results show that the ratio of wall heat flux for the six-hole injector compared to the two-hole injector is 1.61, 0.62, 1.95, 1.72, and 2.11 at the cylinder head, cylinder liner, cavity upper lip, cavity lip, and cavity bottom, respectively. It can be concluded that increasing the total injection amount does not significantly increase the maximum wall heat flux that appears during the combustion process.

In the case of the two-hole injector, the earlier pilot injection into the combustion chamber resulted in a richer mixture formation, predominantly affecting the cavity upper lip area. In contrast, the pre- and main injections more dominantly formed the air-fuel mixture at the cavity bottom. Additionally, the flame residence time was longer at the cavity upper lip compared to the cavity bottom. Consequently, the wall heat flux at the cavity upper lip using the two-hole injector is higher than with the six-hole injector, as shown in Figures 5.11(a) and 5.11(b). Moreover, the wall heat flux at the cylinder liner is higher with the two-hole injector than with the six-hole injector, due to the connection between the cylinder liner space and the upper lip space.

Figure 5.12 shows the effect of the number of injector holes on the spray flame tip penetration using two-hole and six-hole injectors under varying common rail pressures. The results indicate that increasing the common rail pressure increases the spray flame tip penetration. The marks filled with white color indicate spray penetration. Meanwhile, the marks filled with red and blue colors represent the flame penetration of the two-hole and six-hole injectors, respectively.

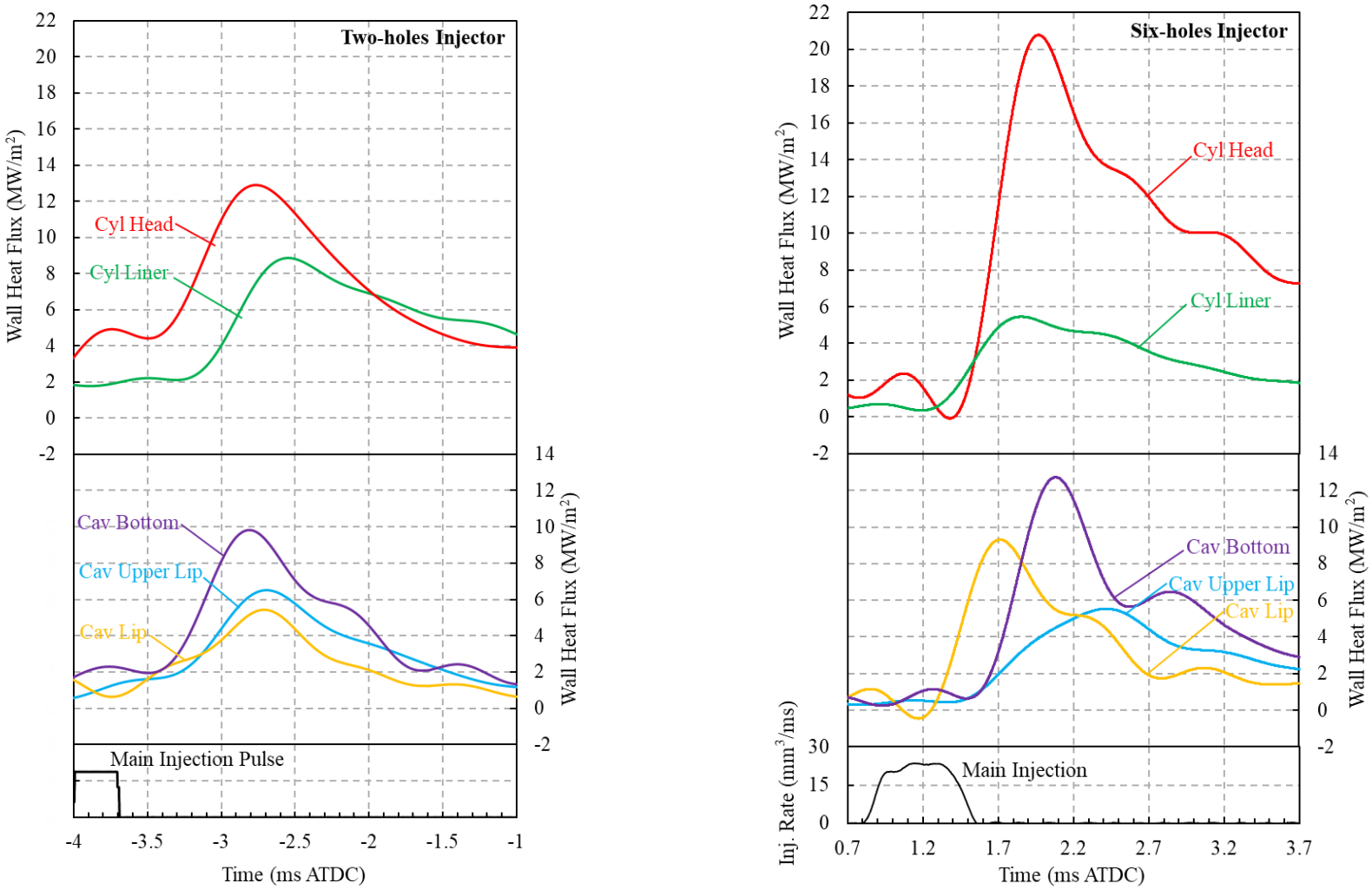

Figure 5.11 Heat flux peak value comparation between two-holes and six-holes injector.

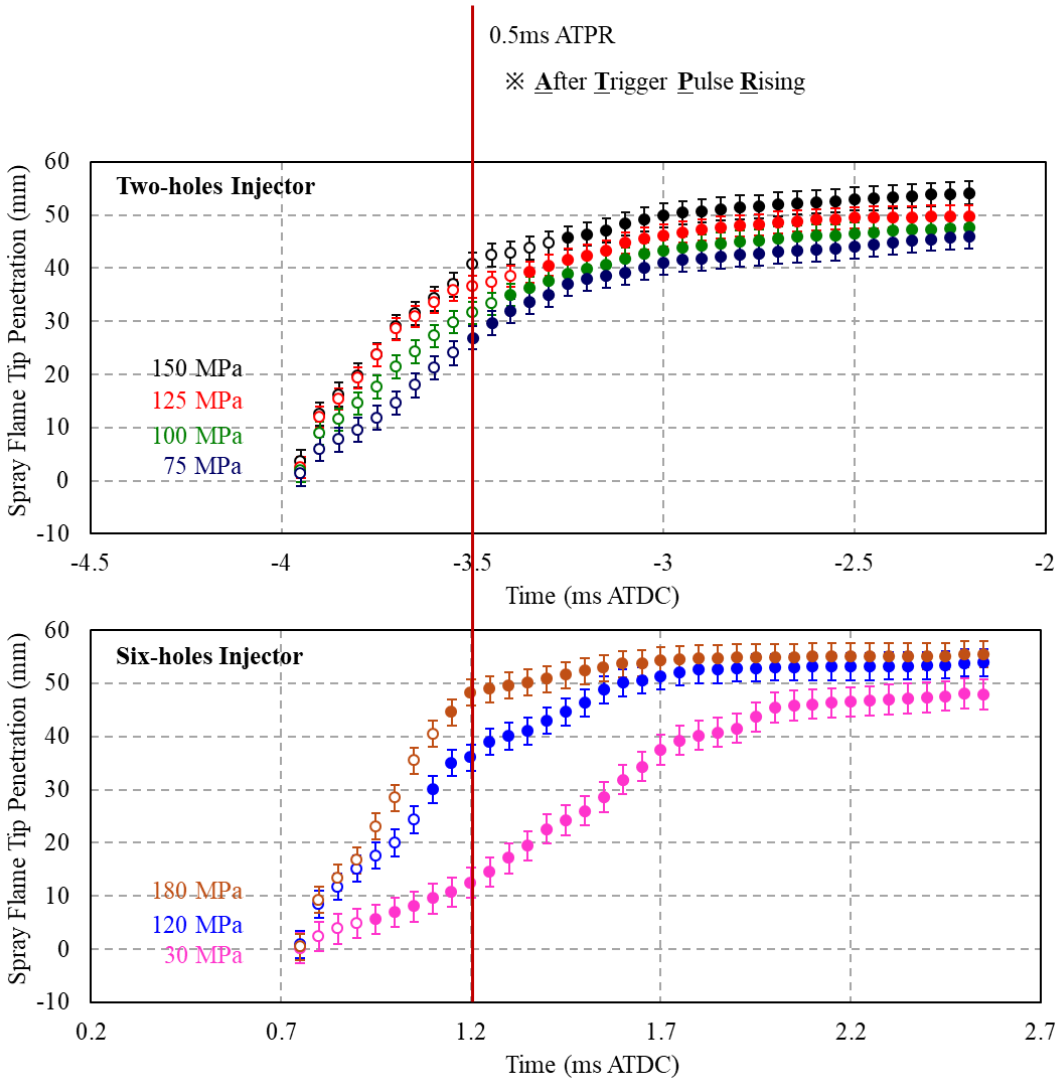

Figure 5.12 Spray flame tip penetration using two-holes and six-holes injector under common rail pressures variation.

For the two-hole injector, the ignition flame appears after the main injection duration. Additionally, increasing the common rail pressure lengthens the ignition delay, which enhances combustion efficiency. The ignition flame appears first at 3.50ms, 3.60ms, 3.65ms, and 3.75ms ATDC using common rail pressures 75, 100, 125, and 150 MPa, respectively. Similarly, for the six-hole injector, an increase in common rail pressure extends the ignition delay, thereby improving combustion efficiency. At a common rail

pressure 30 MPa, the spray flame tip penetration is significantly lower than at 120 and 180 MPa. However, it increases over time and eventually approaches the levels of the higher common rail pressures. With the six-hole injector, higher common rail pressures cause a rich mixture to form near the injector holes due to the spray-to-spray interaction between the three holes on each side of the combustion chamber (left and right). The lower common rail pressure 30 MPa results in a richer mixture near the injector holes compared to the higher pressures of 120 and 180 MPa. Consequently, the flame appears first at 0.90ms, 1.10ms, and 1.15ms ATDC with common rail pressures of 30, 120, and 180 MPa, respectively. Increasing the common rail pressure enhances the ignition delay, which in turn leads to better combustion efficiency.

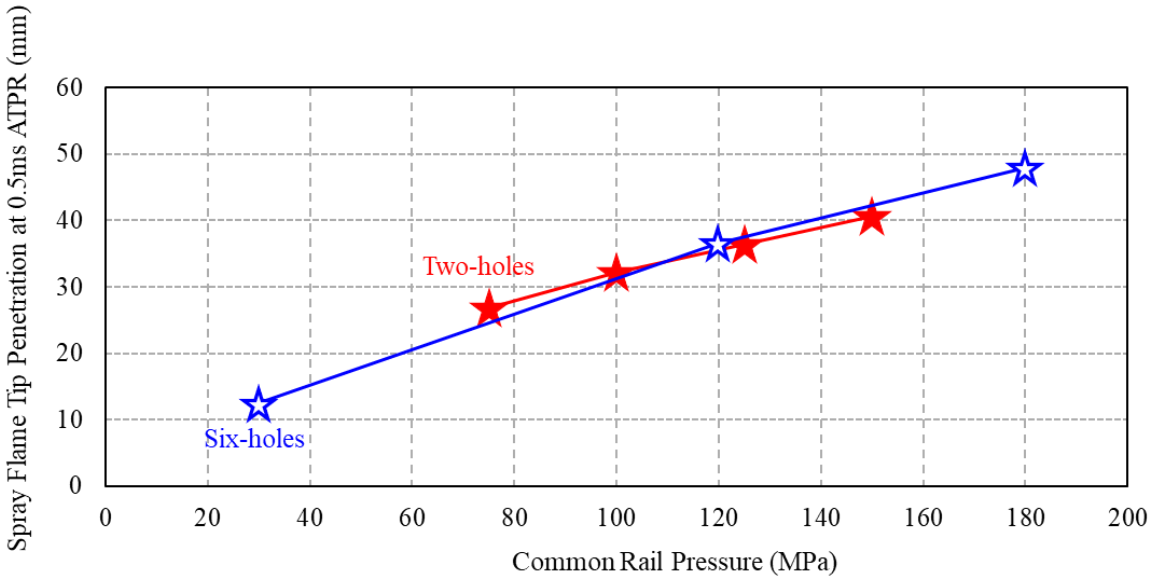

Figure 5.13 Spray flame tip penetration at 0.5ms APTR under two-holes and six-holes injector

To investigate the effect of the number of injector holes on spray flame tip penetration, we use a timing of 0.5ms ATPR (After Trigger Pulse Rising), as shown in Figure 5.13. The results show that increasing common rail pressures increase the spray flame tip penetration for both two-hole and six-hole injectors. In the case of the two-hole injector,

the spray flame tip penetration is initially higher at common rail pressures of 75 and 100 MPa compared to the six-hole injector. However, in subsequent measurements, the spray flame tip penetration with the two-hole injector becomes lower than that of the six-hole injector. Higher common rail pressures enhance the spray flame velocity, leading to a longer spray flame tip penetration. For the six-hole injector, spray-to-spray interaction is observed. After impingement, the spray flames from each hole converge vertically, increasing the velocity of the spray flame. This phenomenon was investigated by Nishida and co-authors [115] [116]. Further explanation of this case is provided in Figure 5.14.

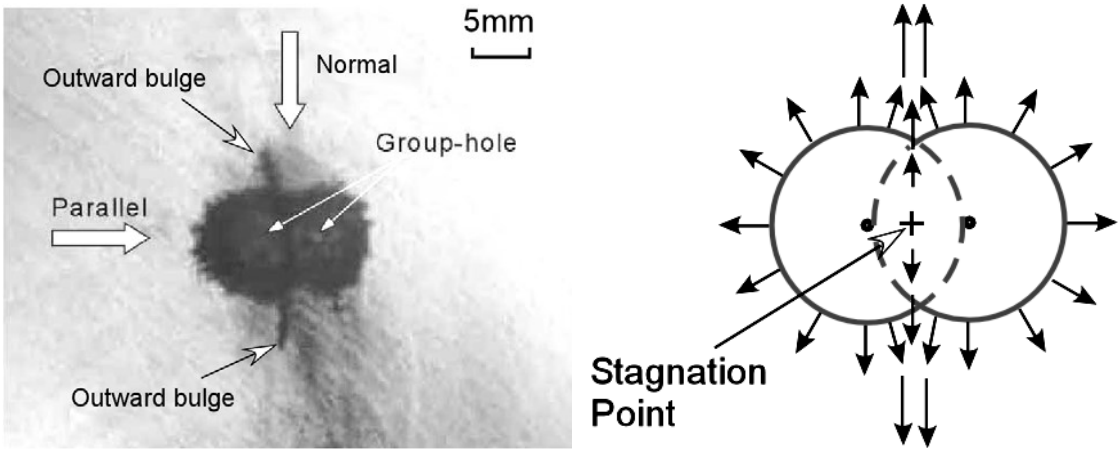

(a) Spray impingement on flat plate (b) Theoretical diagram of spray velocity

Figure 5.14 Spray flame behavior of group nozzle hole after impingement on velocity and penetration [115] [116].

Here, we also compared the effects of similar common rail pressures on spray flame tip penetration between the two-hole injector (125 MPa) and the six-hole injector (120 MPa), as shown in Figure 5.15. The results indicate that the spray flame tip penetration is initially higher for the two-hole injector compared to the six-hole injector, which can be attributed to its higher common rail pressure. However, after impingement, the spray

flame tip velocity of the six-hole injector increases because the spray flames from each hole converge vertically, enhancing the spray flame tip velocity, as shown in Figure 5.14. Consequently, the spray flame tip penetration for the six-hole injector exceeds that of the two-hole injector after 0.5ms ATPR. Additionally, the fuel injection for the two-hole injector occurs before TDC, while for the six-hole injector, it occurs after TDC.

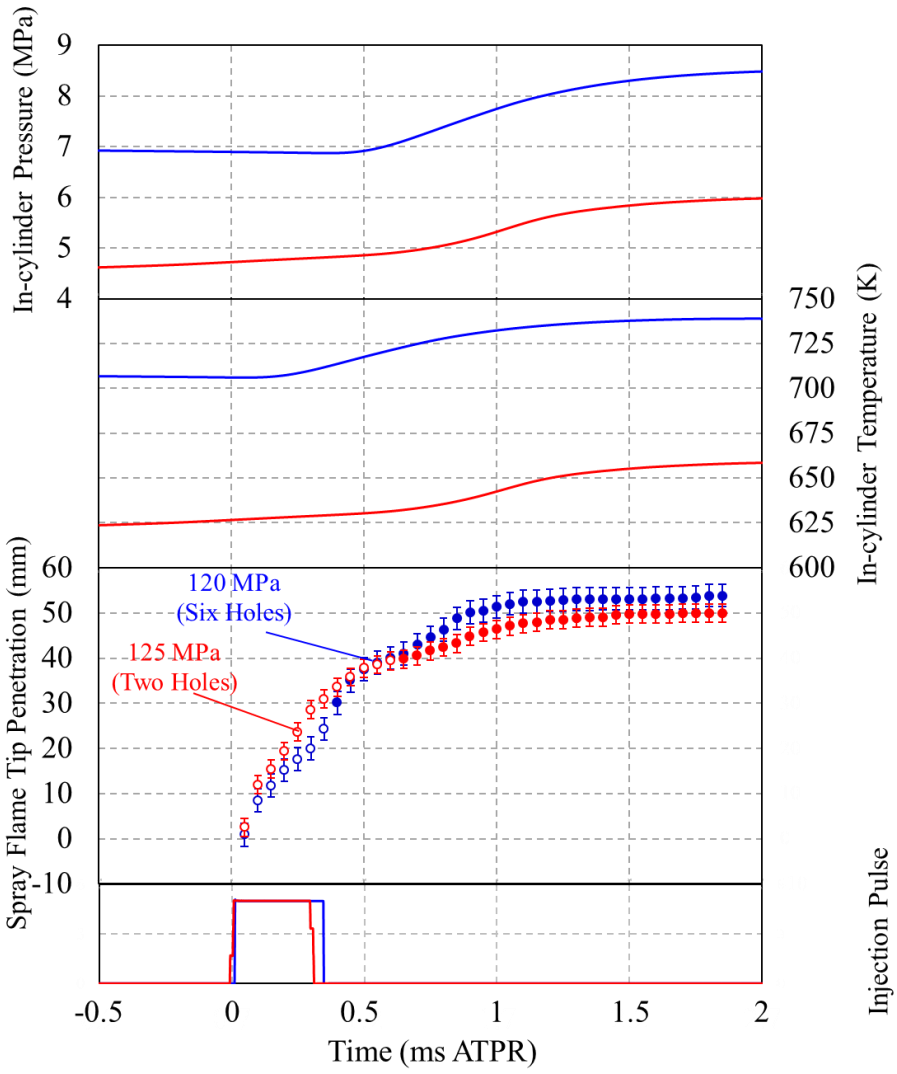

Figure 5.15 Spray flame tip penetration under different number of injector holes

5.4 SUMMARY

To understand the major effects of the number of holes on injector performance, a normalized spray flame distribution was successfully created to investigate flame

distribution in the combustion chamber and wall heat flux. In this experiment, we employed triple injection: pilot, pre-, and main injections using common rail pressures 30, 120, and 180 MPa. A six-hole injector was used to examine the spray-to-spray interaction within the combustion chamber. The results show that increasing the common rail pressure enhances the formation of a lean mixture, which reduces the combustion duration. Meanwhile, the peak value of heat flux increases due to the higher velocity at higher common rail pressures compared to lower pressures. As a result, the accumulated wall heat flux and the total accumulated wall heat flux are lowest at a common rail pressure 120 MPa. The combustion duration has a significant effect on the accumulated wall heat flux, with the highest values observed at a common rail pressure 30 MPa. The common rail pressure 180 MPa results in the highest spray flame velocity and more turbulent flow, leading to an increase in the accumulated wall heat flux. Additionally, the wall heat flux at the cylinder head is the highest due to the intense combustion flame, which produces a highly luminous flame in this region.

From the normalized flame distribution image, we can conclude that the highly luminous flame appears on the cavity side wall and near the injector tip. The spray from each hole contributes to the formation of a rich mixture in the region near the injector. Additionally, the ignition flame first appears along the primary spray axis and reaches the cavity lip, leading to an earlier increase in wall heat flux at this location compared to others. The ignition flame occurs during fuel injection sprays due to the rich mixture from the grouped injector holes. After impinging on the cavity lip, the spray flame spreads to the cavity upper lip and bottom space. The residence time at the cavity bottom is the shortest among all locations. Meanwhile, the flame remains for a longer period in the cavity bottom space, resulting in the highest wall heat flux in the cavity side wall.

The effect of the number of injector holes on spray flame tip penetration is also investigated in this section. Here, we compared the spray flame tip penetration using two-hole injectors with a common rail pressure 125 MPa and six-hole injectors with a common rail pressure 120 MPa. The results show that at the beginning of the injection process, the spray flame tip penetration for the two-hole injector is higher than that for the six-hole injector. However, the six-hole injector eventually overtakes the two-hole injector in spray flame tip penetration due to the higher spray velocity generated after impingement. The spray flames from each hole of the six-hole injector converge vertically, which enhances the spray flame tip velocity and increases overall spray flame penetration. This indicates that the number of injector holes significantly contributes to increasing spray flame tip penetration.

CHAPTER 6 Nu-Re ANALYSES

6.1 DEFINITION OF LOCAL CHARACTERISTIC LENGTH, LOCAL CHARACTERISTIC VELOCITY, AND NEAR-WALL FLAME TEMPERATURE

To investigate the heat transfer phenomena in the combustion chamber, correlation between $Nusselt$ and $Reynolds$ number is presented in this part. At the Nusselt number calculating, characteristic length dan flame temperature are the critical characteristic to be investigated. Meanwhile, the characteristic velocity is the main point to obtain the Reynolds number. Furthermore, local characteristic length, flame temperature, and characteristic velocity are investigated to obtain the $Nu - Re$ correlations.

6.1.1 Local Characteristic Length

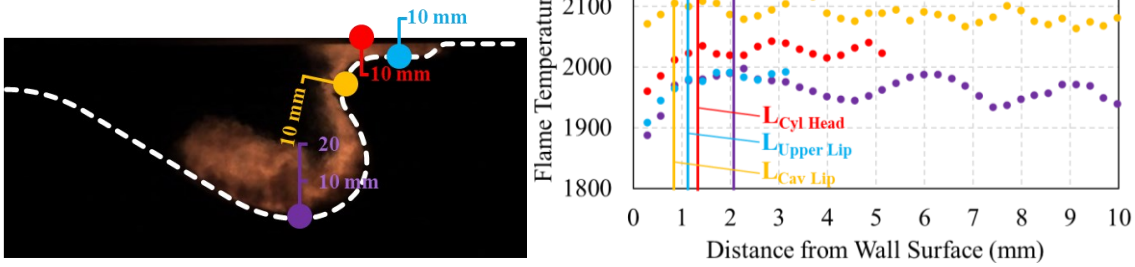

(a) Definition of distance from cavity wall surface.

(b) Definition of local characteristic length

Figure 6.1 Local characteristic lengths for local $Nu - Re$ correlations.

The local characteristic length for the local Nu – Re correlations in the combustion chamber is presented by location. The local characteristic length was measured as the thermal boundary layer thickness, as shown in Fig. 6.1. The flame temperature was measured using two-color pyrometry analysis. First, we measured the temperature along the distance from cavity wall surface, as shown in Figure 6.1 (a). Furthermore, we plotted

the thermal distribution to obtain the boundary layer thickness, as shown in Figure 6.2 (b). We used the same local characteristic length with various local characteristic velocities to calculate the local *Nu-Re* correlations. However, we could not create the luminous flame on the cylinder liner owing to the small space in this region. Furthermore, the local Nu-Re correlation of the cylinder liner is not presented in this study.

6.1.2 Local Characteristic Velocity from Flame Image and Heat Flux Waveform Correlations

The local characteristic velocity v was calculated using the impinging and wall jet velocities, as shown in Figure 6.2. The cylinder head and cavity lip were calculated using the impinging jet velocity because the dominant impinging flame occurred at these locations, as shown in Figures 12 (a) and 12 (c). Meanwhile, the injection flame arrived at the cavity upper lip and cavity bottom after the impinging spray was distributed to the piston cavity surface. Furthermore, the wall jet velocity was used to calculate the local velocity at the cavity upper lip and cavity bottom, as shown in Figures 12 (b) and 12 (d). The signal change in the high-speed luminosity was tracked to estimate the flame movements. The flame movement distance ΔL was calculated by using the distance of the centre of gravity of the flame block (RGB value changing) between two frames. The flame block boundary was obtained using image processing software (MATLAB). The times of each image, t_1 and t_2, were used to obtain the time difference. Eq. (6.1) was used to calculate the local characteristic velocity. Moreover, the local characteristic velocity at high common rail pressures of 125 and 150 MPa had a limited luminous flame, which contributed to the limited velocity obtained at high common rail pressures.

$$v = \frac{\Delta L}{t_2 - t_1} \tag{6.1}$$

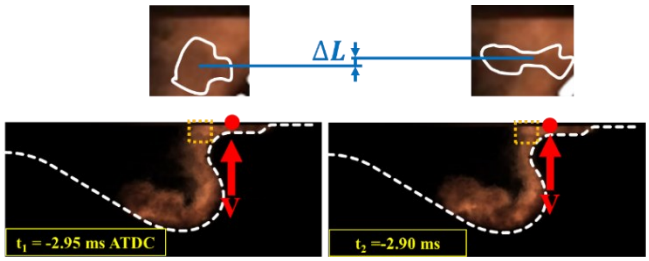

(a) Impinging jet velocity of cylinder head

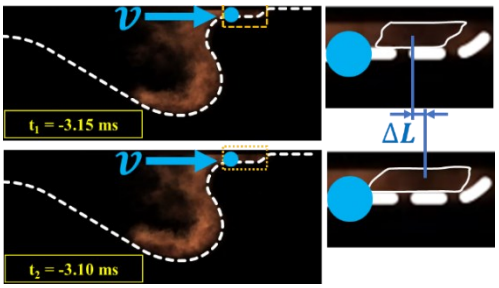

(b) Wall jet velocity of cavity upper lip

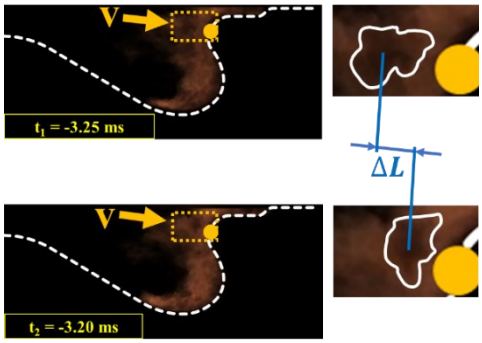

(c) Impinging jet velocity of cavity lip

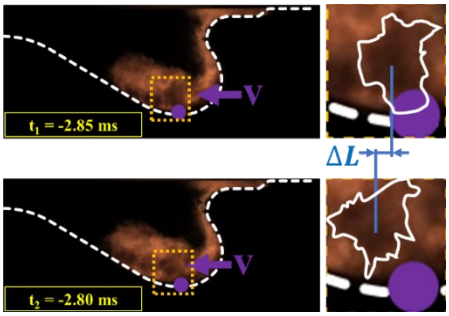

(d) Wall jet velocity of cavity bottom

Figure 6.2 Velocity estimation from flame image correlation.

The local characteristic velocity was obtained using the heat flux waveform correlation [90]. The peaks and troughs of the heat flux waveform correlation were used to determine the wall jet velocity of the flame [117]. The velocity was calculated using the peaks or troughs of the heat flux waveform correlation between the two locations, as shown in Figure 6.3. The flame movement from the cavity lip point to the cavity bottom/upper lip points is represented by the peak and trough of the heat flux waveform correlation. Furthermore, the distance between the two locations and the different peak/trough times of the heat flux sensors were used to calculate the local characteristic velocity. The combustion flame tended to flow in the cavity upper lip space and cavity bottom space after impinging on the cavity lip. Furthermore, the average velocity at the cavity upper lip and cavity bottom was defined as the wall jet velocity. This method was

only used to calculate the wall jet velocity. Additionally, this method was used to validate the local characteristic velocity obtained using the flame image correlation method.

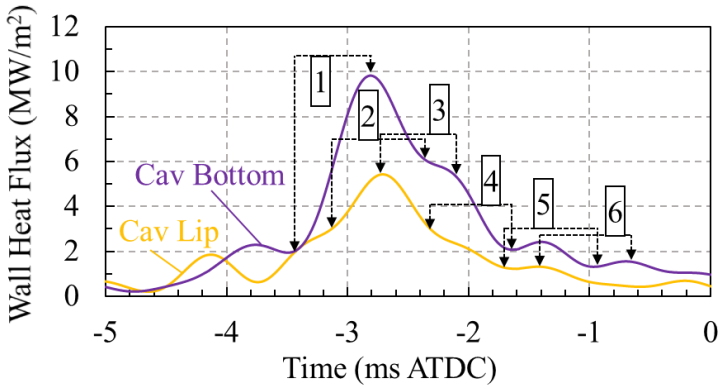

Figure 6.3 Heat flux waveform correlation between two locations.

6.1.3 Near-wall Flame Temperature

The near-wall flame temperature and velocity were obtained to determine heat transfer phenomena in the combustion chamber. Flame image correlation was performed as described in a previous study [117]. The near-wall flame temperature was obtained using two-colour pyrometry analysis. A distance of 1 mm from the wall surface was used to determine the local flame temperature, as shown in Figure 6.4. A plane perpendicular to the wall surface was used to obtain the near-flame temperature, as shown in Figure 6.1 (a). The flame temperature in the cylinder liner was not obtained because of the small space. The flame temperature distributions at different distances on the plane perpendicular to the wall surface are shown in Figure 6.4. The temperature tends to increase to its maximum value at the temperature boundary layer thickness. Furthermore, 1.0 mm from the wall surface as the boundary layer thickness was used as the boundary layer thickness to determine the flame temperature for $Nu - Re$ correlations. The flame temperature increased from the wall surface to a further location and tended to remain

constant at greater distances. The near-wall flame temperature was used to present $Nu - Re$ correlations with the local characteristic velocity from the flame image and heat flux waveform correlation.

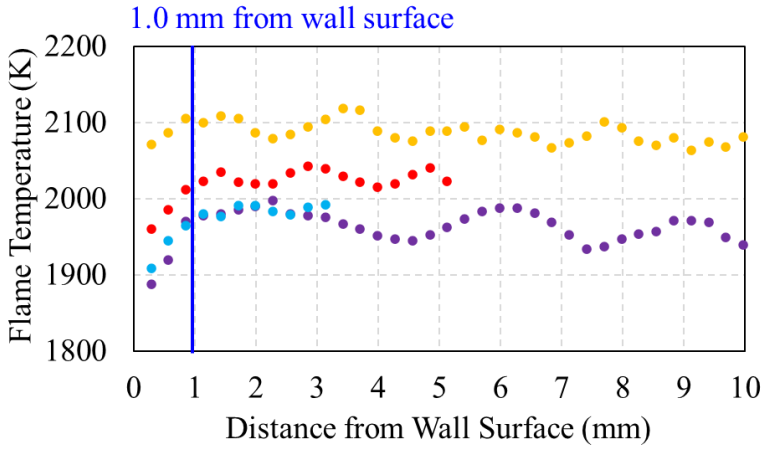

Figure 6.4 Local flame temperature distribution from cavity wall surface.

In this study, we used the same local characteristic length and various local characteristic velocities from the flame image and heat flux waveform correlation. Variations in the local characteristic velocity were used to investigate the local $Nu - Re$ correlations in diesel spray combustion. Table 6.1 lists the local characteristic length, local characteristic velocity, and flame temperature. The flame width was measured as the thickness of the temperature boundary layer. Moreover, the flame width was defined as the local characteristic length of the cavity lip and cavity bottom. The temperature boundary layer thickness on the cylinder head and cavity upper lip could not be measured because of the small space between them. Moreover, the local characteristic length of the cylinder head and cavity upper lip was defined as the clearance length between the cavity and cylinder head surface.

The local characteristic velocity was obtained from the flame image and the heat flux waveform correlation. The impinging and wall jet velocities were defined as the

characteristic velocities from the flame image correlation. The impinging jet velocity was dedicated to the cylinder head and cavity lip because the impinging flame was more dominant in this region. The wall jet velocity was used for the cavity upper lip and cavity bottom owing to flame movement, which was distributed to the cavity upper lip and cavity bottom after the spray flame impinged. The characteristic velocity from heat flux waveform correlation was only used for wall jet velocity, as this method considers the average velocity from two locations [90]. The flame temperature was determined using two-colour pyrometry. Furthermore, a distance of 1.0 mm from the wall surface at each location was used to determine the flame temperature because of the temperature boundary layer thickness, as shown in Figure 6.4.

Table 6.1 Parameters for local characteristic length, local characteristic velocity, and flame temperature.

Location	Local Characteristic Length	Local Characteristic Velocity		Flame Temperature
		Flame Image	Heat Flux Waveform	
Cylinder head	Clearance distance	Impinging jet		1.0 mm from wall surface of cylinder head
Cavity upper lip	Clearance distance	Wall jet	Wall jet	1.0 mm from wall surface of cavity upper lip
Cavity lip	Flame width	Impinging jet		1.0 mm from wall surface of cavity lip
Cavity bottom	Flame width	Wall jet	Wall jet	1.0 mm from wall surface of cavity bottom

6.2 RESULTS OF LOCAL CHARACTERISTIC LENGTH, LOCAL CHARACTERISTIC VELOCITY, AND NEAR-WALL FLAME TEMPERATURE

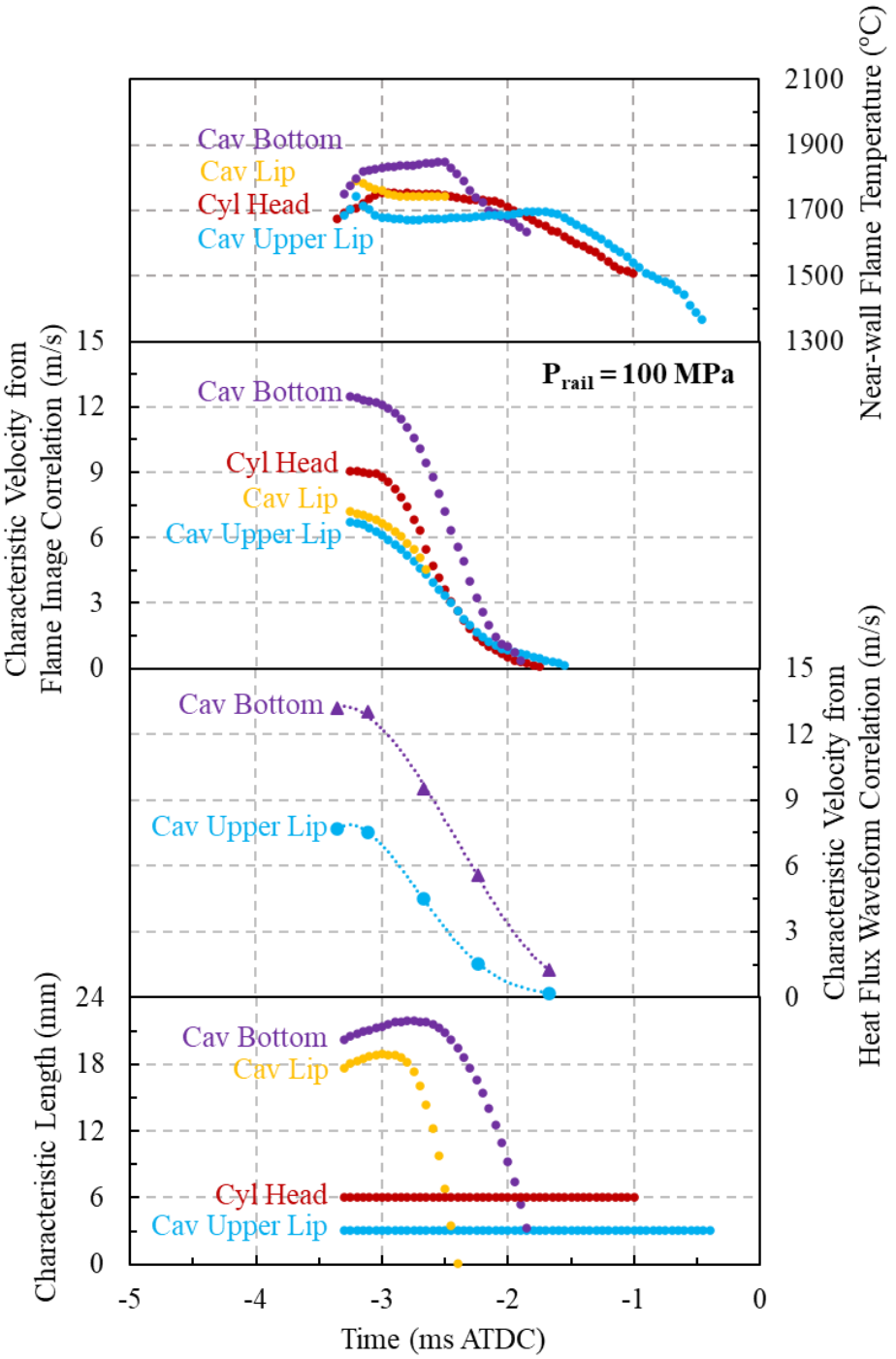

Figure 6.5 Local characteristic length, local characteristic velocity from flame image correlation and heat flux waveform correlation, and near-wall flame temperature P_{rail} = 100 MPa.

The near-wall flame temperature is related to the local flame velocity from the flame image and heat flux waveform correlation. Here, we used the same near-wall flame temperature for the local characteristic velocity from the flame image and heat flux waveform correlation. The $Nu - Re$ correlation results were compared to comprehensively observe the heat transfer phenomena in the combustion chamber. In addition, we compared our results with those of other researchers.

To investigate the heat transfer in the combustion chamber further, the near-wall flame temperature, local characteristic velocity from the flame image correlation, heat flux waveform correlation, and local characteristic length at a common rail pressure 100 MPa were obtained, as shown in Figure 6.5. Owing to space constraints, graphs at common rail pressures 75, 125, and 150 MPa were excluded. The fuel vapor was distributed on the cavity bottom and upper lip space before an intense combustion flame occurred. The local flame temperature increased to its maximum value following the combustion flame and decreased gradually following the reduction in the combustion flame. The wall flame temperature of the cavity bottom had the highest value owing to the intense flame combustion occurring in this region which, reaching 1848.5°C at the common rail pressure 100 MPa. The results showed that a higher common rail pressure increased the local flame distribution and reduced the flame residence time. Furthermore, limited local flame temperatures were reached at common rail pressures125 and 150 MPa because of the low flame luminosity that occurs at high common rail pressures.

A higher common rail pressure enhances spray atomization, fuel evaporation, and air-fuel mixture formation, which reduces the flame luminosity and flame residence timing. Moreover, the flame luminosity was used to investigate the flame movement

from the flame image correlation and to calculate the local characteristic velocity. The near-wall flame temperature tended to increase at the beginning of the combustion process and decreased later, following decrease in combustion intensity. Moreover, the local characteristic velocity tended to be constant at the beginning of the intense combustion and significantly decreases at later stages of the combustion. The near-flame temperature and local characteristic velocity were observed to be more frequently attained at low common rail pressures of 75 and 100 MPa compared to high common rail pressures of 125 and 150 MPa. Additionally, a strong luminous flame was observed at low common rail pressures of 75 and 100 MPa, while a less luminous flame was present at high common rail pressures of 125 and 150 MPa. A higher common rail pressure increased the local characteristic velocity at the local measurement locations, where the cavity bottom had the highest velocity, followed by the cylinder head. The rich mixture was distributed more in the cavity bottom space after impingement at a high velocity owing to the smoothness of the surface compared to other locations.

The local characteristic velocity from the heat flux waveform correlation was related to the wall jet velocity. From the flame image observation, the combustion flame flowing to the cavity bottom space was more dominant than that flowing to the cavity upper lip space owing to the inadequate space at the cavity upper lip. Furthermore, the local characteristic velocity at the cavity bottom was higher than that at the cavity upper lip. Moreover, the variation in common rail pressure influenced the local characteristic velocity. The local characteristic velocity was initially obtained around -3ms ATDC and tended to decrease throughout the fuel injection period, as shown in Figure 6.5. A higher common rail pressure increased the spray tip penetration, which increased the local characteristic velocity. This method is appropriate for calculating the local characteristic

velocity of high common rail pressures, which is difficult to achieve using flame image correlation.

The local characteristic length was obtained based on temperature boundary layer thickness. The injection spray/vapor distribution tended to remain in the cavity bottom space more dominantly than in the cavity upper lip space because adequate space was available. Furthermore, the flame width at the cavity bottom had the highest among all locations. The second-highest flame width was reached by the cavity lip, even though the flame residence time was short. At the cylinder head and cavity upper lip, the temperature boundary layer thickness could not be measured. Moreover, we assumed that the local characteristic length was the distance between the cylinder head and cavity upper lip. In addition, the local characteristic length of the cylinder head and cavity upper lip was constant.

6.3 LOCAL Nu-Re CORRELATIONS USING CHARACTERISTIC VELOCITY FROM FLAME IMAGE CORRELATION

To further understand the heat transfer phenomena, local $Nu - Re$ correlations are presented in this paper. Turbulent heat transfer, assumed as the local $Nu - Re$ correlation, was applied to obtain the local Nu and Re numbers during flame combustion. Moreover, Eqs. $(6.2) - (6.5)$ were used to calculate the heat transfer in the combustion chamber.

$$Nu = (Const.) \times Re^{m} \times Pr^{n} \tag{6.2}$$

$$Nu = \frac{h.L}{\lambda} \tag{6.3}$$

$$Re = \frac{\rho.v.L}{\mu} \tag{6.4}$$

$$h = \frac{q_{wall}}{T_g - T_{wall}} \tag{6.5}$$

Here, Pr indicates the Prandtl number as a constant, assuming [103] that the Nusselt number Nu and Reynolds number Re are represented in Eqs. (6) and (7), respectively. The heat transfer coefficient h is defined in Eq. (8). L refers to the characteristic length, λ indicates the thermal conductivity, ρ denotes the density, μ refers to the viscosity of the working fluid, q_{wall} indicates the heat flux, T_g denotes the gas temperature, and T_{wall} refers to the wall temperature.

6.3.1 Two-holes Injector

In the case of the two-hole injector, the ignition flame appears only on the cavity side wall after the main fuel injection. The early pilot injection forms a rich mixture in the cavity lip space which forms the rich mixture in this region. The pre-injection spray enhances the formation of a lean mixture, promoting better combustion efficiency. Furthermore, the luminous flame only appears after main injection fuel duration. The spray/vapor ignites on the cavity side wall, which leads to an increase in wall heat flux almost simultaneously at all five measurement locations. Additionally, the luminous flame persists for a longer time at the cavity upper lip and bottom space. In addition, the flame residence time has the longest at the end of combustion flame. In this study, we used the luminous flame distribution to determine the characteristic velocity and flame temperature, which influence the Nusselt number (*Nu*) and Reynolds number (*Re*) correlation. The heat transfer coefficient was obtained from the wall heat flux, flame temperature, and surface temperature. Moreover, the flame temperature distribution is used to obtain the thermal boundary layer thickness which result the local characteristic length.

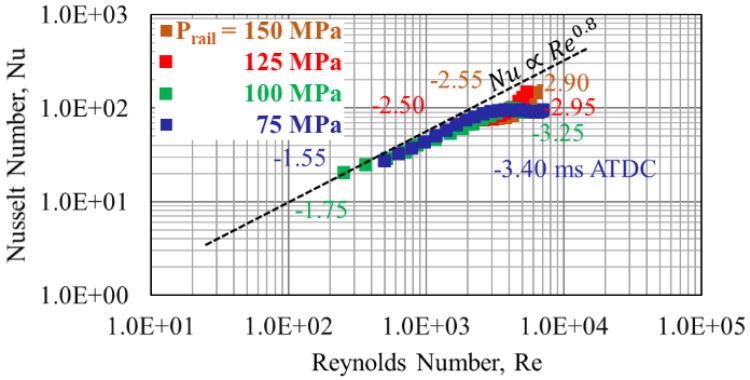

(a) Cylinder head

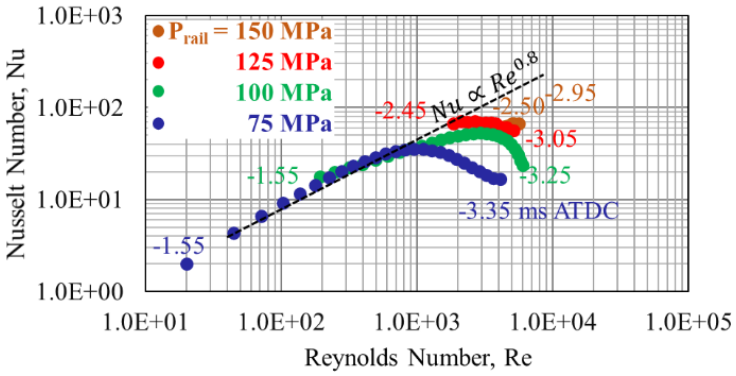

(b) Cavity upper lip

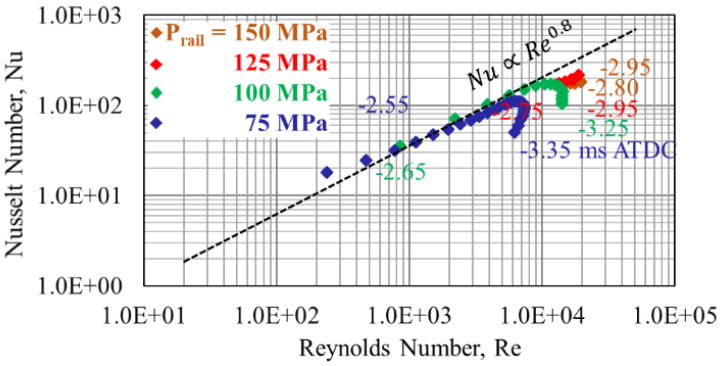

(c) Cavity lip

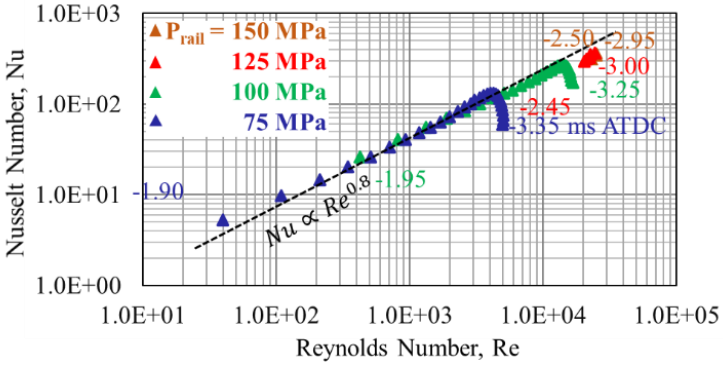

(d) Cavity bottom

Figure 6.6 Local $Nu - Re$ correlations using local characteristic length and characteristic velocity from flame image correlation under two-holes injector.

The local $Nu - Re$ correlations obtained using the local characteristic length and velocity are presented in Figure 6.6. The initial local $Nu - Re$ correlations in the cylinder head reached -3.40, -3.25, -2.95, and -2.90ms ATDC at common rail pressures of 75, 100, 125, and 150 MPa, respectively, as shown in Figure 6.6 (a). Furthermore, they disappeared -1.55, -1.75, -2.50, and -2.55ms ATDC at common rail pressures of 75, 100, 125, and 150 MPa, respectively. Meanwhile, the initial and the last value of local $Nu - Re$ correlations are different depending on the measuring location: cylinder head, cavity upper lip, and cavity bottom, as shown in figures 6.6 (b)-(d). The local $Nu - Re$ correlations increased with the common rail pressure owing to a higher heat transfer coefficient. The different decreasing luminosities in the local flame influenced the endings of the local $Nu - Re$ correlations. The results show that a strong difference in the local $Nu - Re$ values was observed, depending on different measuring locations. Meanwhile, the local $Nu - Re$ correlations were similar. At common rail pressures of 125 and 150 MPa, the flame luminosity alone was observed to be smaller than that observed at common rail pressure 75 and 100 MPa.

A higher common rail pressure forms a better air-fuel mixture and reduces the flame residence time during the combustion process. Furthermore, the local Nu number tended to increase during the early combustion process and decrease during the later stages of combustion in proportion to 0.8^{th} power of the local Re number. The rational value was obtained from related research. Rizal et al. [90] and Kuboyama et al. [103] investigated the local Nu number in proportion to the 0.8^{th} power of the local Re number, respectively. In addition, the local Nu number was proportional to the 0.8^{th} power of the local Re number in the flat plate presented by Johnson et al. in the JSME data book [118]. In conclusion, the $Nu - Re$ correlation remains consistent across

different common rail pressures at various measurement locations: the cylinder head, cavity upper lip, cavity lip, and cavity bottom. This consistency indicates that the wall heat transfer exhibits a similar relationship regardless of the common rail pressure. However, at the cylinder liner, the luminous flame could not be observed due to the limited space in this region, which impedes accurate measurement.

6.3.2 Six-holes Injectors

The use of a multiple-hole injector significantly improves the mixing of fuel with air, facilitating better fuel distribution within the combustion chamber and ensuring a more uniform combustion process. This leads to higher thermal efficiency and lower fuel consumption. In our study, we used a six-hole injector to simulate diesel spray patterns in the combustion chamber. The results show that the ignition flame appears during the fuel injection phase along the primary spray axis. The luminous flame is initially concentrated near the injector holes and the cavity side wall. After impinging on the cavity lip, the luminous flame spreads to the cavity upper lip and bottom space. The luminous flame distribution was also used to derive the $Nu - Re$ correlations.

In the six holes injector, the characteristic velocity and length were obtained using same method as two holes injector, as shown in Figure 6.7. The local Nu number has a similar correlation with proportional to the 0.8^{th} power of the local Re number. Moreover, the local $Nu - Re$ correlations are presented in the various measuring locations. In the cylinder head measuring location, the local $Nu - Re$ has similar correlations at common rail pressures 120 and 180 MPa. Meanwhile, the local $Nu - Re$ correlations at low common rail pressure 30 MPa are the highest due to the highest heat transfer coefficient as shown in Figure 6.7 (a).

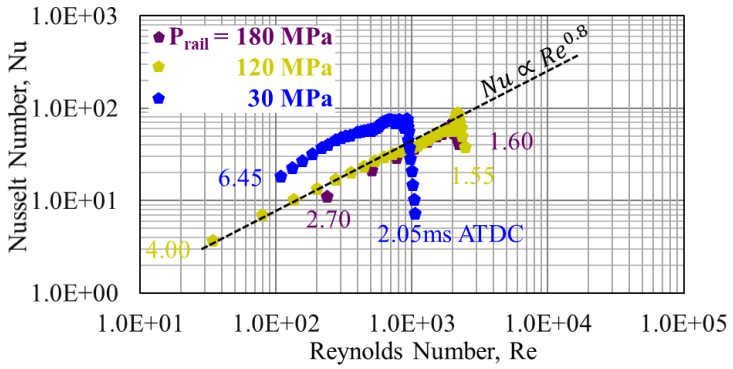

(a) Cylinder head

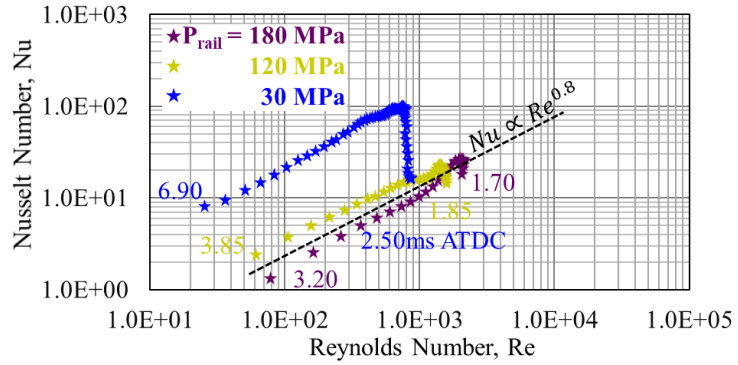

(b) Cavity upper lip

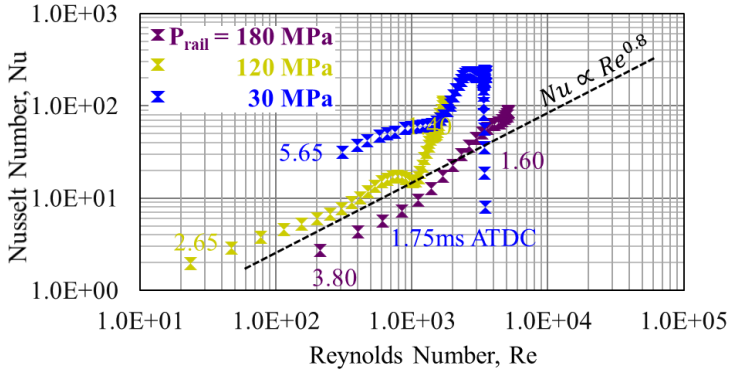

(c) Cavity lip

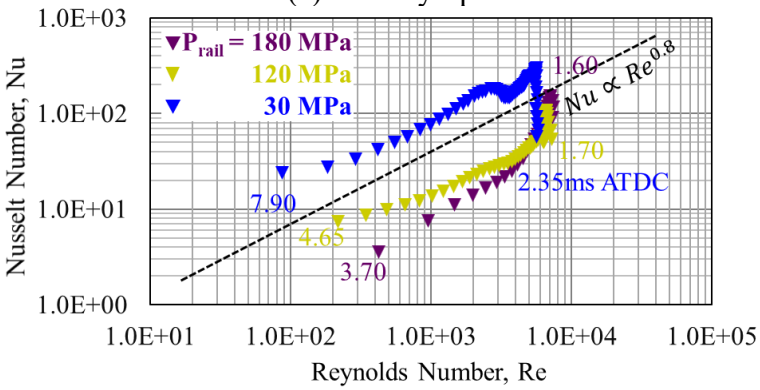

(d) Cavity bottom

Figure 6.7 Local $Nu - Re$ correlations using local characteristic length and characteristic velocity from flame image correlation under six-holes injector.

The local $Nu - Re$ in the cavity upper lip, cavity lip, and cavity bottom are also similar correlations at common rail pressures 120 and 180 MPa. Furthermore, the local $Nu - Re$ correlations at low common rail pressure 30 MPa are also highest than the other common rail pressure, as shown in Figures 6.7 (b)-(d). In the six holes injector, the local $Nu - Re$ correlations at high common rail pressures 120 and 180 MPa are obtained obviously than two holes injector because the total of the injection amount at six holes injector is bigger than the two holes injector. Furthermore, the more flame appears in six holes injector than the two holes injector. A higher common rail pressure enhances the lean mixture formation and reduce the combustion duration. In result, the local $Nu - Re$ correlations at a higher common rail pressure started later time and finished faster following the flame residence time which appear during the combustion process.

6.4 LOCAL Nu-Re CORRELATIONS USING CHARACTERISTIC VELOCITY FROM HEAT FLUX WAVEFORMS CORRELATION

6.4.1 Two-holes Injectors

The local $Nu - Re$ correlations in the cavity upper lip and bottom using the wall jet velocity and local characteristic length are shown in Figure 6.8. Here, we presented the local $Nu - Re$ correlations at the cavity upper lip and cavity bottom because the characteristic velocity from heat flux waveforms is the average velocity between two locations as the wall jet velocity. The results show that the local $Nu - Re$ correlations of the cavity bottom were higher than those of the cavity upper lip. Low common rail pressures of 75 and 100 MPa clearly show the local $Nu - Re$ correlations. Meanwhile, the low luminous flame occurring at high common rail pressures of 125 and 150 MPa was inadequate to obtain the local flame temperature. Furthermore, the local $Nu - Re$ correlations at high common rail pressures of 125 and 150 MPa could not successfully

represent the heat transfer phenomena in the combustion chamber. In addition, the local $Nu - Re$ correlations increased with common rail pressure. As a result, the local $Nu - Re$ correlations using the characteristic velocity from the heat flux waveform correlation were similar to those using the characteristic velocity from the flame image correlation.

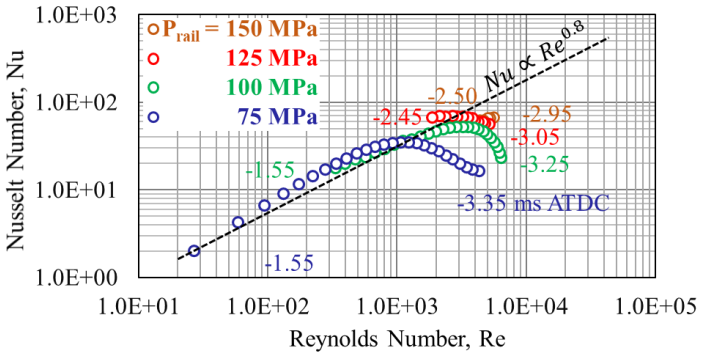

(a) Cavity upper lip

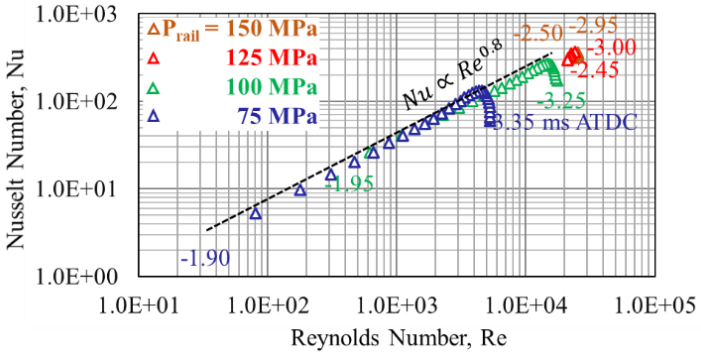

(b) Cavity bottom

Figure 6.8 Local $Nu - Re$ correlations using local characteristic length and characteristic velocity from heat flux waveform correlation under two-holes injector.

6.4.2 Six-holes Injectors

Figure 6.9 shows the local $Nu - Re$ correlations in cavity upper lip and cavity bottom by using average velocity and direct flame image velocity. From the calculation, the thermal boundary layer thickness is used as characteristic length, similar with the local $Nu - Re$ correlations using characteristic velocity from flame image correlations. In this

study, the characteristic velocity used average velocity between two locations as the wall jet velocity. The result shows that there is no significant value between the local $Nu - Re$ correlations by using heat flux waveforms and flame image correlations. The results show that the local Nu number has a similar correlation with proportional to the 0.8^{th} power of the local Re number. In result, there are not significant different between the local $Nu - Re$ correlations by using heat flux waveforms and flame image correlations. Moreover, the local $Nu - Re$ correlations are only presented in the cavity upper lip and bottom which related to the wall jet velocity. From this comparation, we can conclude that the heat flux waveform associated to the wall jet flame velocity on the cavity side.

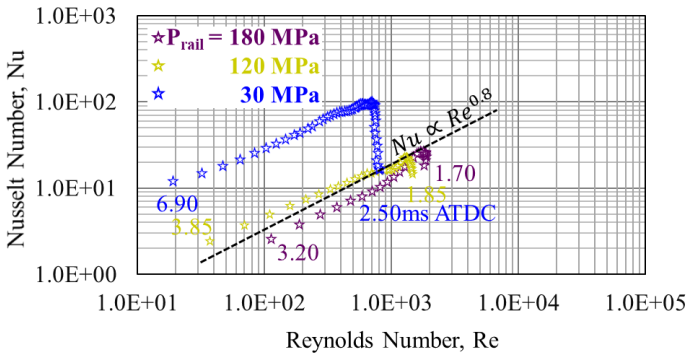

(a) Cavity upper lip

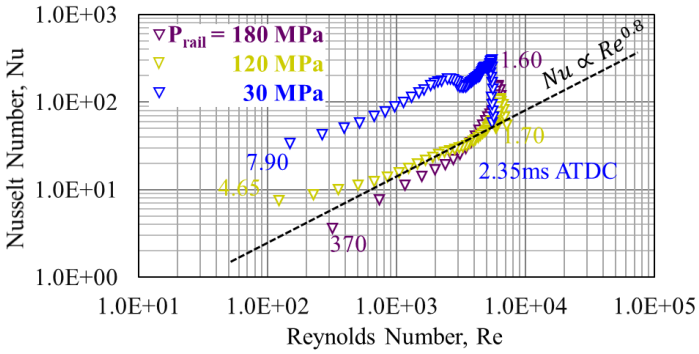

(b) Cavity bottom

Figure 6.9 Local $Nu - Re$ correlations using local characteristic length and characteristic velocity from heat flux waveform correlation under six-holes injectors.

In the six holes injectors, we decided to determine the trendline at common rail

pressure 120 and 180 MPa. Common rail pressure 30 MPa was excluded on calculating the trendline of the local $Nu - Re$ correlations. The local $Nu - Re$ correlations at common rail pressures 120 and 180 MPa is similar. At common rail pressure 30 MPa, the local $Nu - Re$ correlations are higher compared to the others, as shown in Figures 6.7 and 6.9.

6.5 COMPARISON BETWEEN LOCAL Nu-Re CORRELATIONS IN THIS STUDY AND OTHER RESEARCHES

Figure 6.10 shows that the local $Nu - Re$ correlations with various local characteristic velocities were similar. The local Nu number tended to increase to the maximum value after the intense combustion flame occurred and decreased following the reduction in the combustion flame. The local Nu number was correlated with the 0.8^{th} power of the local Re number using the local characteristic velocity from the flame image and heat flux waveform correlation, even under common rail pressure variations at different measurement locations. Furthermore, we obtained the average local $Nu - Re$ correlations, which yielded the following equation: $Nu = 0.173\, Re^{0.80}$.To investigate in more detail, we used two holes and six holes injectors in this study. The local $Nu - Re$ correlations have a similar line at $Nu = 0.173\, Re^{0.80}$ using two holes injector at different common rail pressure, as shown in Figure 6.10 (a). Furthermore, a higher common rail pressure increases the local $Nu - Re$ values. At six holes injector, the local $Nu - Re$ correlations have a different line, as shown in figure 6.10 (b). A lower common rail pressure has a higher $Nu - Re$ value, especially at common rail pressure 30 MPa which has the highest correlation. Furthermore, the local $Nu - Re$ correlations at common rail pressure 30 MPa was excluded on calculating the coefficients of local

$Nu - Re$ correlations. Furthermore, the average local $Nu - Re$ correlations were yielded the following equation: $Nu = 0.104\, Re^{0.80}$.

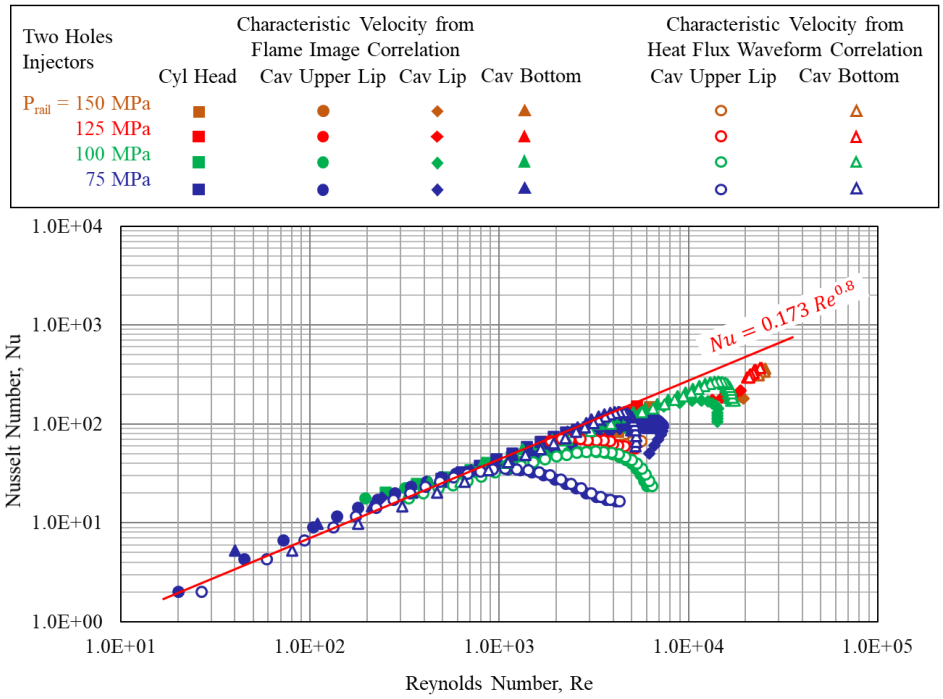

(a) Two-holes injector

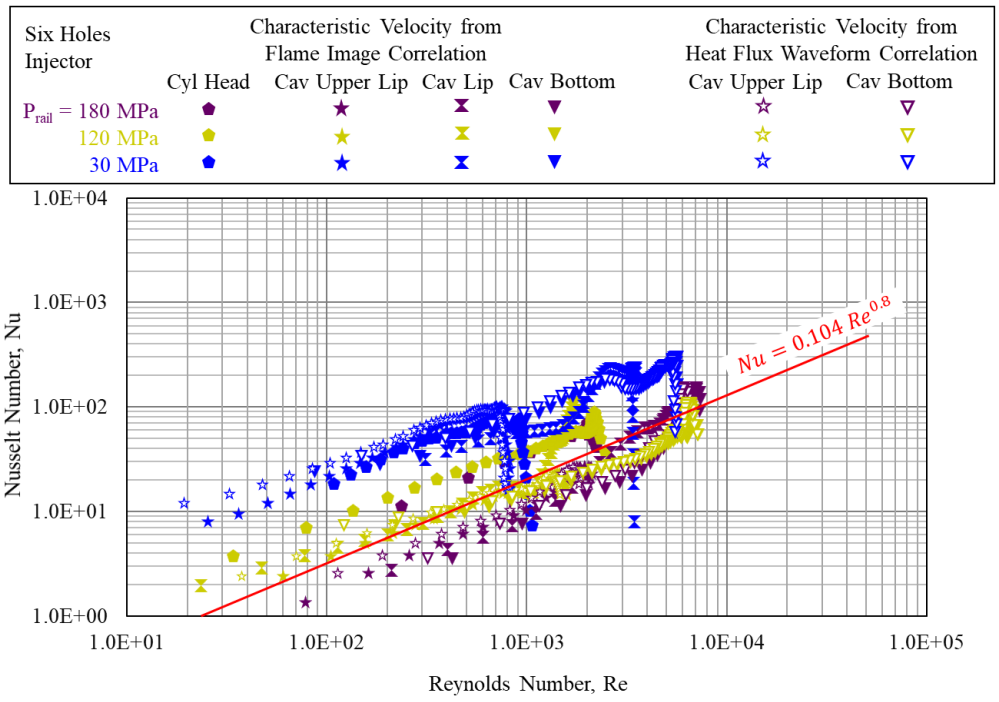

(b) Six-holes injector

Figure 6.10 Comparison of local $Nu - Re$ correlations with local characteristic length and velocity in this study.

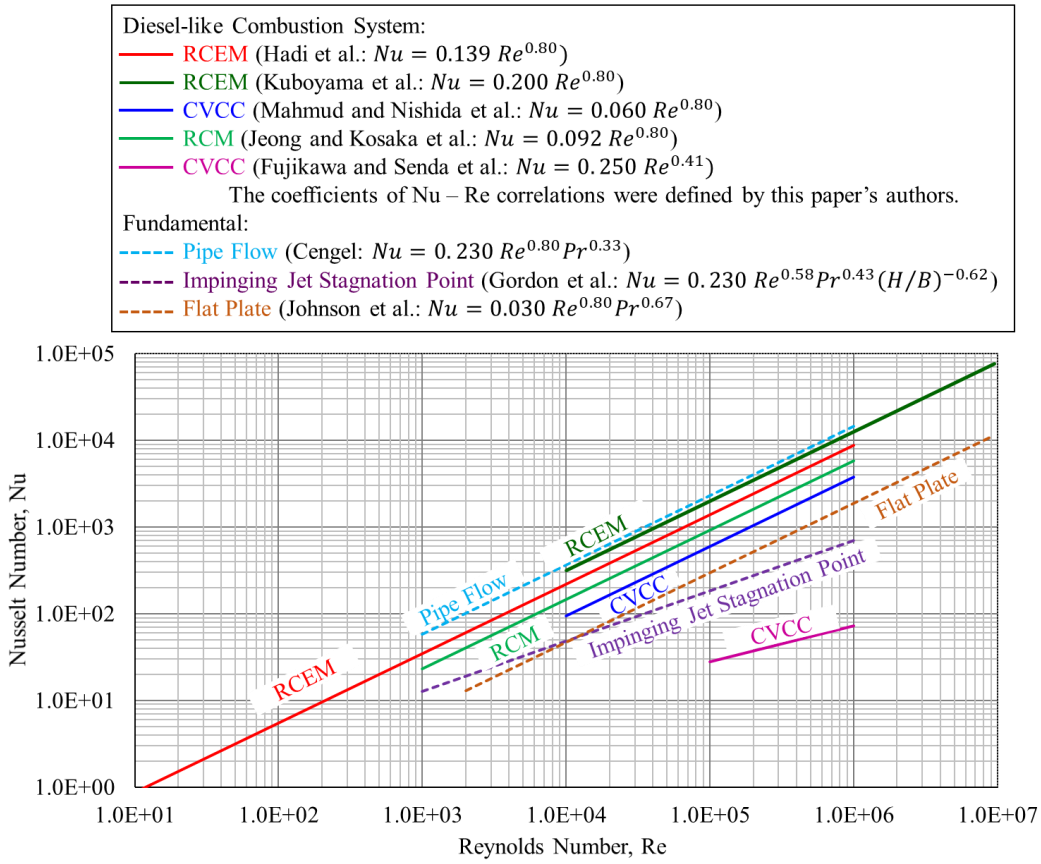

Figure 6.11 Comparison of local $Nu - Re$ correlations in other studies.

Figure 6.11 shows the results of the local $Nu - Re$ correlations in other studies. Here, the local Nu number tends to increase during the early combustion process and decrease during the later stages of combustion in proportion to the 0.8th power of the local Re number, which demonstrates a correlation similar to those observed by other researchers (Kuboyama et al. [103], Mahmud and Nishida et al. [90], Jeong and Kosaka et al. [119], Johnson et al. [118], and Cengel [120]). A previous RCEM study used the bore diameter as the characteristic length and average velocity as the characteristic velocity based on quasi-steady momentum theory and Woschni's equations [103]. The flame temperature was obtained using a two-zone combustion analysis. The heat transfer phenomena in the CVCC used the distance between the hole injector and wall impingement as the characteristic length [90]. The local velocity from the wall heat flux

waveform correlation was used as the characteristic velocity, and the flame temperature was measured using two-colour pyrometry analysis.

Table 6.2 Characteristic length, characteristic velocity, and flame temperature for local $Nu - Re$ correlations shown in Fig. 6.11.

Authors	Characteristic Length	Characteristic Velocity	Flame Temperature
Diesel-like Combustion System			
Hadi et al., RCEM [this study]	Local characteristic length: flame width and clearance distance	Local characteristic velocity: wall jet and impinging jet velocity	Two-colour pyrometry: 1.0 mm from wall surface
Kuboyama et al., RCEM [103]	Bore diameter	Quasi-steady momentum theory and Woschni's equations	Two-zone combustion: average temperature
Mahmud and Nishida et al., CVCC [90]	Impinging distance	Heat flux waveform correlation	Two-colour pyrometry: average temperature
Jeong and Kosaka et al., RCM [119]	Spray width at impinging point	Spray tip velocity using quasi-steady momentum theory	Two-colour pyrometry and CFD: local flame temperature
Fujikawa and Senda et al., CVCC [121]	Impinging distance	Average flame velocity on the wall	Two-colour pyrometry: local flame temperature
Fundamental			
Cengel, Pipe flow [120]	Pipe diameter	Average velocity	Average temperature
Gordon et al., Impinging jet stagnation point [122]	Impinging distance	Impinging jet velocity	Average temperature
Johnson et. al., Flat plate [118]	Length from leading edge	Jet plane speed	Upstream flow temperature

The spray width at the impinging point, spray tip velocity using the quasi-steady momentum theory, and local reference temperature using the two-colour method and ANSYS were used as the characteristic length, characteristic velocity, and flame temperature, respectively, to investigate the heat transfer phenomena in the RCM [119]. The upstream flow temperature was used as the flame temperature to represent the heat transfer phenomenon on the flat plate [118]. The length from the leading edge and the jet plane speed were used as the characteristic length and characteristic velocity, respectively. In addition, the heat transfer phenomena in the pipe flow were investigated [120]. The pipe diameter, average velocity, and average temperature were used as the characteristic length, characteristic velocity, and flame temperature, respectively. However, other researchers have reported different local $Nu - Re$ correlations. The rational value was compared among other researchers, such as Gordon et al. [122], and Fujikawa and Senda et al. [121], who investigated the local Nu number in proportion to the local Re number to the power of 0.58, and 0.41, respectively. The details of the characteristic length, characteristic velocity, and flame temperature from other studies are listed in Table 6.2.

6.6 SUMMARY

In this section, we present the heat transfer phenomenon in the combustion chamber using local $Nu - Re$ correlations. The wall heat flux, flame temperature, and surface temperature were used to determine the heat transfer coefficient. Wall heat flux and surface temperature were measured using a wall heat flux sensor that comprises two thermocouple sensors. The flame temperature was obtained from the luminous flame distribution, which was processed using two-color pyrometry analysis. We measured the flame temperature at 0.1 mm from the wall surface, taking this distance to represent the thermal boundary layer thickness as the characteristic length. The characteristic velocity

was derived from flame images and wall heat flux correlation. The velocity from flame image correlation included both wall jet and impinging velocities, depending on the dominant block spray flame image. On the other hand, the characteristic velocity from wall heat flux correlations was calculated as the average velocity between two heat flux measurement locations. Specifically, the average velocity between the cavity lip and the upper lip was used as the characteristic velocity for the cavity upper lip. Similarly, the average velocity between the cavity lip and the cavity bottom was used as the characteristic velocity for the cavity bottom. The velocity obtained from the wall heat flux data represented the wall jet velocity only. It is important to note that the luminous flame was not visible at the cylinder liner due to the limited space in this region, preventing the formation of a local $Nu - Re$ correlation at the cylinder liner.

In this study, we used two-hole and six-hole injectors to investigate heat transfer phenomena in the combustion chamber. The results indicate that the $Nu - Re$ correlation for the two-hole injector followed a single-line correlation. The local Nu number increased during the early combustion process and decreased during the later stages, proportional to the 0.8th power of the local Re number. Additionally, local $Nu - Re$ correlations were successfully established at lower common rail pressures 75 and 100 MPa. However, at 125 and 150 MPa, it was challenging to create these correlations due to insufficient luminous flame, making it difficult to determine the flame temperature and characteristic velocity.

In the case of the six-hole injector, the local $Nu - Re$ correlation was successfully established. The findings show that the local Nu number is also proportional to the 0.8^{th} power of the local Re number. Lower common rail pressures resulted in higher heat

transfer within the combustion chamber due to the increased radiative heat from the flame. Notably, the local Nu number at a common rail pressure 30 MPa was higher than at 120 and 180 MPa. Consequently, we used common rail pressures 120 and 180 MPa to create a trendline illustrating the heat transfer phenomena with the six-hole injector. In conclusion, the local Nu number is proportional to the 0.8^{th} power of the local Re number for both two-hole and six-hole injectors.

CHAPTER 7 CONCLUSIONS

The purpose of this study is to understand the heat transfer phenomena and spray flame behavior in the combustion chamber. We used a rapid compression and expansion machine (RCEM) to simulate single-cycle diesel engines with a multiple injection strategy. This experiment introduces a novel aspect in the form of the piston cavity model. We employed a two-dimensional (2D) piston cavity design to accurately investigate the combustion process in diesel engines. This uniquely shaped model has been utilized by only a few researchers, making our study particularly innovative. To explore the heat transfer phenomena, we installed wall heat flux sensors in both the cylinder and the cavity sides of the combustion chamber. Specifically, three wall heat flux sensors were placed on the cavity side: at the cavity upper lip, the lip, and the bottom. Additionally, two wall heat flux sensors were installed on the cylinder side: one at the cylinder head and another at the cylinder liner.

In this experiment, a two-hole injector was used to thoroughly investigate the spray flame behavior in the combustion chamber. We applied common rail pressures of 75, 100, 125, and 150 MPa to examine the impact of these variations on heat transfer and spray flame behavior. For the six-hole injector case, common rail pressures of 30, 120, and 180 MPa were used to simulate conditions similar to those in real diesel engines equipped with ten-hole injectors.

In this study, we also present the local Nusselt number and Reynolds number to elucidate the heat transfer phenomena within the combustion chamber. The heat transfer coefficient was calculated using measurements of wall heat flux, flame temperature, and

surface temperature. The wall heat flux and surface temperature were obtained using wall heat flux sensors equipped with two thermocouples. The flame temperature was determined using a two-color pyrometry analysis from flame images captured via direct photography, without a backlight. A distance of 0.1 mm from the wall surface was considered for the flame temperature measurements. The thermal boundary layer thickness was designated as the local characteristic length. Additionally, characteristic velocities were derived from flame image analysis and wall heat flux correlations. The characteristic velocity derived from flame image correlation accounted for both the wall jet and impingement velocities, depending on the dominant spray flame behavior. Meanwhile, the characteristic velocity obtained from the wall heat flux correlation was dedicated to the wall jet velocity, as the average velocity measurements were only obtained at the cavity upper lip and bottom.

7.1 MAIN FINDINGS OF THIS STUDY

The main findings of this study are divided into three parts: the effects of the two-hole injector on wall heat flux and spray flame behavior, the effects of the six-hole injector on wall heat flux and spray flame behavior, and the results of Nusselt number and Reynolds number correlations that elucidate the heat transfer phenomena within the combustion chamber. The key findings related to the impact of the two-holes injector under varying common rail pressures (75, 100, 125, and 150 MPa) are detailed as follows:

(1) Fuel injection fills the high-temperature combustion chamber and causes fuel evaporation and air-fuel mixture formation. The combustion process is significantly promoted after wall impingement. The early pilot injection tends to distribute the fuel mixing more dominantly in the upper lip space than in the cavity bottom space which contributes to forms the rich mixture formation at the cavity upper lip space. The pre-

injection successfully enhances the spray atomization and air fuel mixture formation which effectively accelerate the main combustion.

(2) The luminous flame appears only after the main injection spray duration using two-holes injector, as the lean mixture formation occurs following the pilot and pre-injection sprays. Consequently, the wall heat flux increases almost simultaneously at various locations due to the near-simultaneous appearance of the luminous flame. Meanwhile, the apparent heat release rate increases later, following the pilot and pre-injection sprays, despite the absence of a luminous flame observed in this experiment.

(3) The flame is primarily observed in the cavity side wall and persists for an extended period at the cavity upper lip and bottom space. Notably, the flame residence time is the longest at the cavity upper lip, attributed to the rich mixture resulting from the earlier pilot injection spray.

(4) Increasing the common rail pressure enhances spray atomization and fuel evaporation, reduces the combustion duration, and increases the peak value of the wall heat flux. Consequently, KL factor is reduced because of the lesser luminous flame formed during the combustion process. The maximum peak value of the wall heat flux is reached by the cylinder head owing to the intense flame combustion process occurring in this region, followed by the cavity bottom, as the highest flame temperature is achieved around this location.

(5) Increasing the common rail pressure from 75 to 125 MPa reduces the accumulated heat flux owing to the flame residence time, heat flux peak value, and combustion duration. Furthermore, a common rail pressure 150 MPa yields a higher accumulated heat flux compared to a common rail pressure 125 MPa owing to the higher impingement and turbulence resulting from a high common rail pressure, which

increase the accumulated heat flux.

The key findings related to the impact of the six-holes injector under varying common rail pressures (30, 120, and 180 MPa) are detailed as follows:

(1) Before intense combustion occurs, the air-fuel mixture fills the high-temperature combustion chamber. After the pilot injection, the air fuel mixture formation is initiated at the cavity lip, leading to increase the wall heat flux at this location. The main combustion flame occurs along the centerline of the primary spray axis and then spreads to the combustion chamber. The spreading of the flame increases the temperature and cylinder pressure, which significantly influences the AHRR and the wall heat flux distribution.

(2) High common-rail pressure promotes spray evaporation and air mixture formation after spraying and impingement more effectively than low common-rail pressure. The higher spray flame velocity and longer spray tip penetration leads to an increase in turbulence flow and reduce the duration of combustion, which in turn increases the maximum magnitude of apparent heat release rate and wall heat flux. The visualization provided illustrates that the wall heat flux increases because of both flame spread and higher spray flame velocity. Therefore, the high common-rail pressure significantly increases the maximum heat-flux magnitude and decreases the duration of ignition.

(3) The wall heat flux is affected by the nonuniformity of the spray and flame distribution, causing it to arrive at each measurement point at different moments after impingement. The wall heat flux is initially observed at the lip, subsequently at the upper lip, and finally at the bottom of the cavity. In addition, the highest wall heat

flux on the cavity side occurs at the bottom of the cavity. On the cylinder side, the spreading flame remains around the cylinder head long after impingement, inducing intense temperatures for an extended period. Therefore, the wall heat flux on the cylinder head is the highest of all the locations.

(4) From the results of the normalized flame image distribution, the luminous flame is observed predominantly at the cavity side wall and near the injector holes, owing to the rich mixture formed by spray-to-spray interaction. Subsequently, the ignition flame initiates at the primary spray axis before impingement. Following impingement, the luminous flame extends to the cavity upper lip and bottom space. Consequently, the flame resides longest at the cavity bottom compared to other locations.

(5) Compared to the common rail pressure 120 MPa, a low common rail pressure 30 MPa exhibits a more significant difference in the accumulated wall heat flux ratio, leading to longer combustion periods. The cylinder head contributes the most wall heat flux because of the longer flame residence. In contrast, the high spray flame velocity and impingement rate caused by a high common rail pressure 180 MPa induces high heat flux, while the combustion duration is shortened.

The key findings related to Nusselt number and Reynolds number correlations that elucidate the heat transfer phenomena are detailed as follows:

(1) For Reynolds number calculations, the characteristic length is defined as the thickness of the thermal boundary layer. Characteristic velocity was determined using flame images and wall heat flux waveforms correlations. And the flame temperature was obtained using two-color pyrometry analysis. Results indicate that

the characteristic velocity derived from flame image correlations shows no significant difference compared to that characteristic velocity from wall heat flux waveforms.

(2) In the case of the two-hole injector, a local $Nu - Re$ correlation was successfully established using low common rail pressures of 75 and 100 MPa. However, at higher common rail pressures of 125 and 150 MPa, establishing the local $Nu - Re$ correlations proved challenging due to the limited luminous flame, which made it difficult to obtain accurate flame temperatures and characteristic velocities. Moreover, the local $Nu - Re$ correlations exhibited a linear trend, effectively illustrating heat transfer phenomena within the combustion chamber. The local Nusselt number was found to scale with the 0.8^{th} power of the Reynolds number.

(3) In contrast, for the six-hole injector, a local Nu-Re correlation was successfully established using all common rail pressures: 30, 120, and 180 MPa. At a low common rail pressure 30 MPa, there was a significant increase in heat transfer within the combustion chamber due to the enhanced radiative heat from the flame. Notably, the local Nu number at a common rail pressure 30 MPa was higher than at 120 and 180 MPa. In conclusion, the local Nusselt number is proportional to the 0.8^{th} power of the local Reynolds number.

7.2 RECOMMENDATIONS FOR FUTURE WORKS

This study employed a Rapid Compression and Expansion Machine to simulate a single-cycle diesel engine, analyze spray flame distribution in a two-dimensional combustion chamber, and examine wall heat transfer and heat transfer phenomena during

the combustion process. To further elucidate the mechanisms of heat transfer, the following recommendations are proposed for future work:

(1) Investigate multiple injection with post-injection**:**

Future research should explore the effects of common rail pressure variations on NOx emissions and exhaust efficiency using multiple injection strategies, including post-injection. This approach could provide insights into optimizing emissions control and enhancing overall engine efficiency.

(2) Examine different injector hole diameters**:**

It is crucial to study the impact of varying injector hole diameters on heat transfer phenomena. Understanding how different diameters affect thermal efficiency could lead to better designs for diesel spray engines and improved thermal management strategies.

(3) Utilize numerical computational methods**:**

Employing numerical computational techniques can provide a deeper understanding of the physical phenomena occurring within the combustion chamber. These methods can complement experimental data and offer detailed insights into complex processes that are difficult to measure directly.

(4) Apply particle image velocimetry (PIV)**:**

Particle image velocimetry (PIV) is a valuable tool for gaining a detailed understanding of spray flame velocity during fuel injection and combustion. Future studies should consider using PIV to accurately capture velocity fields and enhance the understanding of spray dynamics and combustion behavior.

The primary goal of this study is to reduce heat loss and thereby improve the thermal efficiency of diesel engines. Future research should include real engines with ten-holes and twelve-holes injectors for comparison with the current findings. Additionally, investigating different injector hole diameters with post-injection under various conditions is essential to determine the heat transfer rates and minimize heat loss, ultimately enhancing thermal efficiency.

REFERENCES

[1] ExxonMobil, "2017 Outlook for Energy," *Outlook for Energy,* p. 52, 2018.

[2] ExxonMobil, "Our View to 2025," *2023 Global Outlook Executive Summary,* p. 6, 2023.

[3] International Energy Agency, "World Energy Outlook 2023," *World Energy Outlook 2023,* p. 29, 2023.

[4] J. C. Ge, G. Wu and N. J. Choi, "Comparative study of pilot–main injection timings and diesel/ethanol binary blends on combustion, emission and microstructure of particles emitted from diesel engines," *FUEL,* vol. 313, 2022.

[5] J. Du, B. Mohan, J. Sim, T. Fang and W. L. Roberts, "Auto-ignition characteristics of high-reactivity gasoline fuel using a gasoline multi-hole injector," *Experimental Thermal and Fluid Science,* vol. 112, 2020.

[6] D. Stock and R. Bauder, "The new Audi- 5 cylinder turbo diesel engine: the first passenger car diesel engine with second generation direct injection," *SAE Technical Paper 900648,* 1990.

[7] Y. Wang, G. He, H. Huang, X. Guo, K. Xing, S. Liu, Z. Tu and Q. Xia, "Thermodynamic and exergy analysis of high compression ratio coupled with late intake valve closing to improve thermal efficiency of two-stage turbocharged diesel engines," *Energy,* vol. 268, no. 126733, pp. 1-14, 2023.

[8] U. Asad, P. S. Divekar and M. Zheng, "High efficiency ethanol–diesel dual-fuel combustion: Analyses of performance, emissions and thermal efficiency over the engine load range," *Fuel,* vol. 310, no. 122397, pp. 1-12, 2022.

[9] M. G. Thurston, M. R. Sullivan and S. P. McConky, "Exhaust-gas temperature model and prognostic feature for diesel engines," *Applied Thermal Engineering,* vol. 229, no. 120578, pp. 1-17, 2023.

[10] Z. Ma, Y. Gu, S. Zhu, M. Yang and K. Deng, "Analysis on capability of power recovery of marine diesel engine at high backpressure conditions," *Applied Thermal Engineering,* vol. 204, no. 117933, pp. 1-12, 2022.

[11] C. Hao, Z. Lu, Y. Feng, H. Bai, M. Wen and T. Wang, "Optimization of fuel/air mixing and combustion process in a heavy-duty diesel engine using fuel split device," *Applied Thermal Engineering,* vol. 186, no. 116458, pp. 1-12, 2021.

[12] Q. Xin, Diesel Engine System Design, Woodhead Publishing Ltd, 2011.

[13] J. Kanzaki, M. Namba, K. Nakamura, T. Tadokoro, S. Kim, D. Shimo, Y. Ogata and K. Nishida, "Verification of Distribution Contlled Partially Compression Ignition

Consept Through Combustion Visualization," in *Internal Combustion Engine Symposium*, Tokyo, Japan, 2023.

[14] X. Wang, H. Li, G. Li, J. Fan, H. Bai, Y. Gao and H. Huo, "Effect of injection pressure on low-temperature fuel atomization characteristics of diesel engines under cold start conditions," *International Journal of Multiphase Flow,* vol. 172, no. 104712, pp. 1-11, 2024.

[15] C. Fan, K. Nishida and Y. Ogata, "Visualization of diesel spray and combustion from lateral side of two-dimensional piston cavity in rapid compression and expansion machine, second report: Effects of injection pressure and interval of split injection," *International Journal of Engine Research,* vol. 23, no. 3, pp. 446-459, 2021.

[16] A. O. Emiroglu, "Effect of fuel injection pressure on the characteristics of single cylinder diesel engine powered by butanol-diesel blend," *FUEL,* vol. 256, 2019.

[17] T. Han, R. Singh, G. Lavoie, M. Wooldridge and A. Boehman, "Multiple injection for improving knock, gaseous and particulate matter emissions in direct injection SI engines," *Applied Energy,* vol. 262, 2020.

[18] A. Yousefi, H. Guo and M. Birouk, "Split diesel injection effect on knocking of natural gas/diesel dual-fuel engine at high load conditions," *Applied Energy,* vol. 279, 2020.

[19] F. Chang, H. Luo, Y. Hagino, T. Tashima, K. Nishida and Y. Ogata, "Effect of split injection on fuel adhesion characteristics under non-evaporation and evaporation conditions," *FUEL,* vol. 317, 2022.

[20] X. Wen, R. Martin , W. Han, J. H. Chen and C. Hasse, "Investigation of the ignition processes of a multi-injection flame in a Diesel engine environment using the flamelet model," *Proceedings of the Combustion Institute,* vol. 38, p. 5605–5613, 2021.

[21] K. Yang, K. Nishida, Y. Ogata and H. Yamakawa, "Characteristics of fuel evaporation, mixture formation and combustion of 2D cavity impinging spray under high-pressure split injection," *Fuel,* vol. 234, pp. 746-756, 2018.

[22] K. Yang, G. Guo, Z. He, Y. Jin, Y. Shen, K. Lu and K. Nishida, "Effect of oxygen concentration on the split injection combustion process of diesel spray injected into 2D piston cavity," *Applied Thermal Engineering,* vol. 231, no. 120934, pp. 1-10, 2023.

[23] K. Yang, Z. He, Y. Zhang and K. Nishida, "Effect of single and split injection on combustion process of diesel spray injected into 2D piston cavity," *Fuel,* vol. 334, no. 126639, pp. 1-10, 2023.

[24] X. Zhao , F. Liu and C. Wang, "Effects of different piston combustion chamber heights on heat transfer and energy conversion performance enhancement of a heavy-duty truck diesel engine," *Energy,* vol. 249, no. 123732, pp. 1-15, 2022.

[25] Z. Chen, P. Zhao, T. Wang, H. He, H. Chen, P. Zhang , Y. Li, L. Geng and D. Qi,

"Visualization study the cross spray and combustion characteristics of diesel and methanol in a constant volume combustion chamber at cold and flare flash boiling regions," *Energy,* vol. 301, no. 131654, pp. 1-11, 2024.

[26] J. B. Herwood, Internal Combustion Engine Fundamentals: Second Edition, New York: McGraw-Hill Education, 2018.

[27] M. Kono, M. Basaki, M. Ito, T. Hashizume, S. Isyiyama and K. Inagaki, "Cooling Loss Reduction of Highly Dispersed Spray Combustion with Restricted In-Cylinder Swirl and Squish Flow in Diesel Engine," *SAE Int. J. Engines,* pp. 504-515, 2012.

[28] T. Aizawa, H. Kosaka and Y. Matsui, "2-D Imaging of Soot Formation Process in a Transient Spray Flame by Laser-induced Fluorescence and Incandescence Techniques," *SAE Technical Paper 2002-01-2669,* 2022.

[29] T. Kamimoto, N. Uchida, T. Aizawa, K. Kondo and T. Kuboyama, "Diesel flame imaging and quantitative analysis of in-cylinder soot oxidation," *International Journal of Engine Research,* vol. 18, no. 5-6, pp. 422-435, 2016.

[30] O. A. Kuti, J. Zhu, K. Nishida, X. Wang and Z. Huang, "Characterization of spray and combustion processes of biodiesel fuel injected by diesel engine common rail system," *Fuel,* vol. 104, pp. 838-846, 2013.

[31] K. Nishida, J. Zhu, X. Leng and Z. He, "Effects of micro-hole nozzle and ultra-high injection pressure on air entrainment, liquid penetration, flame lift-off and soot formation of diesel spray flame," *International Journal of Engine Research,* vol. 18, no. 1-2, pp. 51-65, 2017.

[32] X. Wang, Z. Huang, W. Zhang, O. A. Kuti and K. Nishida, "Effects of ultra-high injection pressure and micro-hole nozzle on flame structure and soot formation of impinging diesel spray," *Applied Energy,* vol. 88, no. 5, pp. 1620-1628, 2011.

[33] H. Kosaka, T. Aizawa and T. Kamimoto, "Two-dimensional imaging of ignition and soot formation processes in a diesel flame," *International Journal of Engine Research,* vol. 6, 2005.

[34] S. Huang, T. Li, X. Wang, R. Chen, R. Yang and Z. Qian, "Effects of various discharge strategies on ignition and combustion of lean natural gas mixture under the static and turbulent conditions," *Experimental Thermal and Fluid Science,* vol. 133, 2022.

[35] O. Samimi-Abianeh, "Line-of-Sight optical diagnostic for measuring combustion products using species' natural emissions," *Experimental Thermal and Fluid Science,* vol. 118, 2020.

[36] O. Samimi-Abianeh, M. Al-Sadoon and L. Bravo, "Gas temperature and boundary layer thickness measurements of an inert mixture using filtered broadband natural emission of species at Rapid Compression Machine conditions (Part II),"

Experimental Thermal and Fluid Science, vol. 111, 2020.

[37] J. A. Piehl and O. Samimi-Abianeh, "Dual-perspective boundary layer thickness measurements using filtered natural emissions of species," *Experimental Thermal and Fluid Science,* vol. 122, 2021.

[38] A. H. Motily, J. I. Ryu, K. Keunsoo, K. Kim, C.-B. M. Kweon and T. Lee, "High-pressure fuel spray ignition behavior with hot surface interaction," *Proceedings of the Combustion Institute,* vol. 38, p. 5665–5672, 2021.

[39] K. Yang, S. Yasaki, K. Nishida and Y. Ogata, "Injection strategy to Enhance Mixture Fortamation and Combustion of Fuel Spray in Diesel Engine," *SAE International,* 2018.

[40] D. Shimo, "Research on improvement of diesel combustion by controlling distributions of mixture concentration/temperature an ignition/heat release rate," Dissertation, Hiroshima: Hiroshima University; Japanese., 2013.

[41] S. Kim, D. Fukuyama and D. Shimo, "Simultaneous improvement of exhaust emissions and fuel consumption by optimization of combustion chamber shape of a diesel engine.," *International Journal of Engine Research,* vol. 18, no. 5-6, pp. 412-421, 2017.

[42] Y. Kato, S. Kim and D. Fukuda, "Heat balance analysis using cylinder pressure obtained by engine experiments considering the spatial heterogeneity of diesel combustion," in *JSAE/SAE Powertrains, Fuels and Lubricants*, 2019.

[43] C. Fan, D. Wang , K. Nishida and Y. Ogata , "Visualization of diesel spray and combustion from lateral side of two-dimensional piston cavity in rapid compression and expansion machine," *International Journal of Engine Research,* vol. 22, no. 10, pp. 3247-3259, 2020.

[44] T. Lind, Z. Li, R. Rajasegar, G. Roberts, Ö. Andersson and M. P. Musculus, "Diffuse back-illumination temperature imaging (DBI-TI), a novel soot thermometry technique," *Combustion and Flame,* vol. 240, no. 111949, pp. 1-12, 2022.

[45] R. Pairy, J. Gimeno, S. Cardona and S. Ayyapureddi, "Experimental study of the influence of the fuel and boundary conditions over the soot formation in multi-hole diesel injectors using high-speed color diffused back-illumination technique," *Applied Thermal Engineering,* vol. 158, no. 113746, pp. 1-16, 2019.

[46] W. Shang, J. Cao, S. Yang and Z. He, "In-flame soot quantification of N-Hexadecane droplets using diffused back-illumination extinction imaging," *Case Studies in Thermal Engineering,* vol. 30, no. 101699, pp. 1-10, 2022.

[47] P. Yi, Y. Wu, C. Meng, J. Deng, T. Li and R. Chen, "An investigation on pyrolysis characteristics of low-sulfur heavy fuel oil spray under diesel engine-like conditions," *Journal of the Energy Institute,* vol. 114, no. 101590, pp. 1-11, 2024.

[48] R. Liu, L. Huang, R. Yi, J. Xia, J. Zhang, M. Feng and X. Lu, "Visualization on spray and flame characteristics of wall-impinging spray under marine diesel engine conditions," *Applied Thermal Engineering,* vol. 244, no. 122655, pp. 1-15, 2024.

[49] D. Wang, Z. Shi, Z. Yang, H. Chen and Y. Li, "Numerical study on the wall-impinging diesel spray mixture formation, ignition, and combustion characteristics in the cylinder under cold-start conditions of a diesel engine," *Fuel,* vol. 317, no. 123518, pp. 1-10, 2022.

[50] C. Zhai, Y. Jin, Z. Feng, F. Chang, H. Luo, K. Nishida and O. Yoichi, "Characterization of diesel spray combustion under micro-hole and ultra-high injection pressure conditions-analyses of diffused back-illumination imaging and OH* chemiluminescence imaging," *Fuel Processing Technology,* vol. 252, no. 107955, pp. 1-15, 2023.

[51] M. D. Altinkurt , M. Merts and A. Turkcan, "Effects of split diesel injection strategies on combustion, knocking, cyclic variations and emissions of a natural gas-diesel dual fuel medium speed engine," *Fuel,* vol. 347, no. 128517, pp. 1-13, 2023.

[52] A. Santhoshkumar, V. Thangarasu and A. Ramanathan, "Experimental and empirical analysis of performance, combustion and emission characteristics of diesel engine fueled with pyrolysis waste engine oil under single and split injection strategy," *Sustainable Energy Technologies and Assessments ,* vol. 55, no. 102893, pp. 1-14, 2023.

[53] J. Liu, X. Zhang, Y. Liu, P. Sun, Q. Ji , X. Wang, Z. Li and H. Ma, "Experimental study on in-cylinder combustion and exhaust emissions characteristics of natural gas/diesel dual-fuel engine with single injection and split injection strategies," *Process Safety and Environmental Protection,* vol. 172, no. 172, pp. 225-240, 2023.

[54] J. Liu, Y. Liu, Q. Ji, P. Sun, X. Zhang, X. Wang and H. Ma, "Effects of split injection strategy on combustion stability and GHG emissions characteristics of natural gas/diesel RCCI engine under high load," *Energy,* vol. 266, no. 126542, pp. 1-13, 2023.

[55] A. Yousefi, H. Guo and M. Birouk, "Split diesel injection effect on knocking of natural gas/diesel dual-fuel engine at high load conditions," *Applied Energy,* vol. 279, no. 115828, p. 2022, 1-14.

[56] C. Fan, D. Wang, K. Nishida and Y. Ogata, "Visualization of diesel spray and combustion from lateral side of two-dimensional piston cavity in rapid compression and expansion machine," *International Journal of Engine Research,* vol. 22, no. 10, pp. 1-13, 2020.

[57] T. Aizawa, T. Kinoshita, S. Akiyama, K. Shinohara and Y. Miyagawa, "Infrared high-

speed thermography of combustion chamber wall impinged by diesel spray flame," *International Journal of Engine Research,* vol. 23, no. 7, pp. 1116-1130, 2021.

[58] R. Payri, J. M. Garcia-Oliver, V. Mendoza and A. Vierra, "Analysis of the Influence of Diesel Spray Injection on the Ignition and Soot Formation in Multiple Injection Strategy," *Energies,* vol. 13, no. 3505, 2020.

[59] C. Windarto, A. Setiawan, N. H. X. Duy and O. Lim, "Investigation of propane direct injection performance in a rapid compression and expansion machine: Pathways to diesel marine engine efficiency parity with spark discharge duration strategies," *International Journal of Hydrogen Energy,* pp. 1-21, 2023.

[60] G. Xu, M. Kotzagianni, P. Kyrtatos, Y. M. Wright and K. Boulouchos, "Experimental and numerical investigations of the unscavenged prechamber combustion in a rapid compression and expansion machine under engine-like conditions," *Combustion and Flame,* vol. 204, pp. 68-84, 2019.

[61] D. K. Dasrath, R. Biwalkar , S. Singh and W. F. Northrop, "Bowl piston geometry as an alternative to enlarged crevice pistons for rapid compression machines," *Proceedings of the Combustion Institute,* vol. 38, no. 4, pp. 5723-5731, 2021.

[62] A. I. El-Seesy, H. Kosaka, H. Hassan and S. Sato, "Combustion and emission characteristics of a common rail diesel engine and RCEM fueled by n-heptanol-diesel blends and carbon nanomaterial additives," *Energy Conversion and Management,* vol. 196, pp. 370-394, 2019.

[63] L. Zhou, K. Yang, Z. Ping, T. Nie, X. Biao and L. Huang, "Experimental study on the effect of post-injection parameters on performance of extra-high pressure common-rail diesel engine," *Energy Reports,* vol. 8, no. 7, pp. 152-160, 2022.

[64] A. Pacino, C. L. Porta, A. L. Rocca and A. Cairns, "Copper leaching effects on combustion characteristics and particulate emissions of a direct injection high pressure common rail diesel engine," *Fuel,* vol. 340, no. 127536, pp. 1-9, 2023.

[65] A. Hadadpour, M. Jangi, K. M. Pang and X. S. Bai, "The role of a split injection strategy in the mixture formation and combustion of diesel spray: A large-eddy simulation," *Proceedings of the Combustion Institute,* vol. 37, no. 4, pp. 4709-4716, 2019.

[66] M. Pucilowski, M. Jangi, H. Fatehi, K. M. Pang and X.-S. Bai, "LES study of diesel flame/wall interaction and mixing mechanisms at different wall distances," *Proceedings of the Combustion Institute,* vol. 38, no. 4, pp. 5597-5604, 2021.

[67] W. Zhang, C. Fan, G. Lyu, Y. Li, Y. Liu, C. Wang and C. Song, "An analysis of the in-cylinder soots generated from the main- and post-injection combustion in diesel engines," *Proceedings of the Combustion Institute,* vol. 39, no. 1, pp. 939-947, 2023.

[68] L. Rao, Y. Zhang, S. Kook, K. S. Kim and C.-B. Kweon, "Understanding in-cylinder

soot reduction in the use of high pressure fuel injection in a small-bore diesel engine," *Proceedings of the Combustion Institute,* vol. 37, no. 4, pp. 4839-4846, 2019.

[69] Y. Wang, G. Wang, G. Yao, Q. Shen, X. Yu and S. He, "Combining GA-SVM and NSGA-Ⅲ multi-objective optimization to reduce the emission and fuel consumption of high-pressure common-rail diesel engine," *Energy,* vol. 278, no. 127965, pp. 1-14, 2023.

[70] H. Wu, L. Sun, Z. Shi, H. Li, L. Zhang, Y. Bo, W. Cao and X. Li, "Effect of wall parameters on impinging combustion and soot emission characteristics of heavy-duty diesel engine at low temperature," *Chemosphere,* vol. 306, no. 135568, pp. 1-10, 2022.

[71] J. Zhang, W. Jing and T. Fang, "High speed imaging of OH* chemiluminescence and natural luminosity of low temperature diesel spray combustion," *Fuel,* vol. 99, pp. 226-234, 2012.

[72] R. Payri, F. J. Salvador, J. Gimeno and J. d. l. Morena, "Effects of nozzle geometry on direct injection diesel engine combustion process," *Applied Thermal Engineering,* vol. 29, no. 10, pp. 2051-2060, 2009.

[73] L. Feng, Y. Wang, Chen B. and et l., "OH, soot and temperature distributions of wall-impinging diesel fuel spray under different wall temperature," in *2019 JSAE/SAE Powertrains. Fuels and Lubricants*, 2019.

[74] M. Choi and S. Park, "Optimization of multiple-stage fuel injection and optical analysis of the combustion process in a heavy-duty diesel engine," *Fuel Processing Technology,* vol. 228, 2022.

[75] D. Kim, S. Kook, R. Kusakari, K. Shinohara, K. Iijima and T. Aizawa, "Soot particles in piston-top pool fires and exhaust at 5 and 15 MPa injection pressure in a gasoline direct-injection engine," *Proceedings of the Combustion Institute,* vol. 38, p. 5761–5768, 2021.

[76] M. Pucilowski, M. Jangi, H. Fatehi, K. M. Pang and X.-S. Bai, "LES study of diesel flame/wall interaction and mixing mechanisms at different wall distances," *Proceedings of the Combustion Institute ,* vol. 38, p. 5597–5604, 2021.

[77] G. M. Bianchi, P. Pelloni, F. E. Corcione and Luppino, "Numerical analysis of passenger car HSDI diesel engines with the 2nd generation of common rail injection systems: the effect of multiple injections on emissions," *SAE Paper 2001-01-1068,* 2001.

[78] T. Aizawa, T. Kinoshita and S. Akiyama, "Infrared high-speed thermography of combustion chamber wall impinged by diesel spray flame," *International Journal of Engine Research,* 2021.

[79] R. Payri, J. M. Garcia-Oliver and V. Mendoza, "Analysis of the influence of diesel spray

injection on the ignition and soot formation in multiple injection strategy," *Energies,* vol. 13, p. 3505, 2020.

[80] L. Wang, K. N. Vinod and T. Fang, "Spark effects on compression ignition of PRF95 direct injection spray in a constant volume combustion chamber," *Experimental Thermal and Fluid Science,* vol. 129, 2021.

[81] X. Bai, P. Cheng, Q. Li, L. Sheng and Z. Kang, "Effects of self-pulsation on combustion instability in a liquid rocket engine," *Experimental Thermal and Fluid Science,* vol. 114, 2020.

[82] H. Li, R. Verschaeren, T. Beji and S. Verhelst, "Investigation of evaporating sprays in a medium speed marine engine," *Experimental Thermal and Fluid Science,* vol. 121, 2021.

[83] Y. Liu, J. Tian, F. Li and L. Bao, "Experiment and analysis on the spray characteristics of diesel/polyoxymethylene dimethyl ethers (PODE)/ethanol blends in non-reacting environment," *Experimental Thermal and Fluid Science,* vol. 131, 2022.

[84] K. Shen, Z. Xu, H. Chen and J. Du, "Combined effects of high energy ignition and tumble enhancement on performance of lean combustion for GDI engine," *Experimental Thermal and Fluid Science,* vol. 129, 2021.

[85] S. Zeraati-Rezaei, Y. Al-Qahtani, J. M. Herreros and H. Xu, "Investigation of the effects of split-injection on particle emissions from a Dieseline CI engine," *Applied Energy,* vol. 262, 2020.

[86] H. K. T. A. Y. M. Tatsuya Kuboyama, "A study on Heat Loss in DI Diesel Engine," in *Combustion in Internal Combustion Engine (COMODIA)*, Yokohama, Japan, 2004.

[87] C. Zhai, Y. Jin, K. Nishida and Y. Ogata, "Diesel spray and combustion of multi-hole injectors with micro-hole under ultra-high injection pressure – Non-evaporating spray characteristics," *FUEL,* vol. 283, pp. 1-15, 2021.

[88] C. Zhai, Y. Jin, Q. Wu, K. Nishida and Y. Ogata, "Diesel spray and combustion of multi-hole injectors with micro-hole under ultra-high injection pressure – Combustion characteristics," *FUEL,* vol. 300, pp. 1-12, 2021.

[89] R. Mahmud, T. Kurisu, K. Nishida, Y. Ogata, J. Kanzaki and T. Tadokoro, "Experimental study on flat-wall impinging spray flame and its heat flux on wall under diesel engine–like condition: First report—effect of impingement distance," *Proceedings of the Institution of Mechanical Engineers, Part D: Journal of Automobile Engineering,* vol. 233, no. 8, 2019.

[90] R. Mahmud, T. Kurisu, K. Nishida, Y. Ogata, J. Kanzaki and O. Akgol , "Effects of injection pressure and impingement distance on flat-wall impinging spray flame and its heat flux under diesel engine-like condition," *Advances in Mechanical Engineering,*

vol. 11, no. 7, pp. 1-15, 2019.

[91] G. Borman and K. Nishiwaki, "Internal-combustion engine heat transfer," *Prog. Energy Combust. Sci.,* vol. 13, pp. 1-46, 1987.

[92] T. Lefeuvre, P. S. Myers and O. A. Uyehara, "Experimental Instantaneous Heat Fluxes in a Diesel Engine and Their Correlation," 1969.

[93] G. Eichelberg, "Some New Investigations on Old Combustion Engine Problems," *Engineering,* vol. 148, pp. 436-446, 547-560, 1939.

[94] G. Sitkei and G. Ramanaiah, "A Rational Approach for Calculation of Heat Transfer in Diesel Engines," *SAE Tech. Pap.,* no. 720027, p. 165–174, 1972.

[95] T. Morel and R. Keribar, "A Model for Predicting Spatially and Time Resolved Convective Heat Transfer in Bowl-in-Piston Combustion Chambers," *SAE Tech. Pap.,* no. 850204, 1985.

[96] T. Morel, C. I. Rackmil, R. Keribar and M. J. Jen, "Model for Heat Transfer and Combustion In Spark Ignited Engines and its Comparison with Experiments," *SAE Tech. Pap.,* no. 880198, 1988.

[97] G. F. Hohenberg, "Advanced Approaches for Heat Transfer Calculations," *SAE Tech. Pap.,* no. 790825, p. 19, 1979.

[98] S. Bin Han, Y. J. Chung, Y. J. Kwon and S. Lee, "Empirical Formula for Instantaneous Heat Transfer Coefficient in Spark Ignition Engine," *SAE Tech. Pap.,* no. 972995, p. 1997.

[99] C. A. Finol and K. Robinson, "Thermal modelling of modern engines: A review of empirical correlations to estimate the in-cylinder heat transfer coefficient," *Proc. Inst. Mech. Eng. Part D J. Automob. Eng.,* vol. 220, no. 12, p. 1765–1781, 2006.

[100] W. J. D. Annand, "Heat Transfer in the Cylinder of Reciprocating Internal Engines," *Proc. Instn Mech. Enginers,* vol. 36, p. 973–990, 1963.

[101] G. Woschni, "A Universally Applicable Equation for the Instantaneous Heat Transfer Coefficient in the Internal Combustion Engine," 1967.

[102] J. Chang, O. Güralp and Z. Filipi, D. N. Assanis, and et al, "New heat transfer correlation for an HCCI engine derived from measurements of instantaneous surface heat flux," *SAE Tech. Pap.,* no. 2004-01-2996, 2004.

[103] T. Kuboyama, Y. Moriyoshi and H. Kosaka, "Heat transfer analysis in a diesel engine based on a heat flux measurement using a rapid compression and expansion machine," *SAE Technical paper,* vol. 32, no. 0115, 2017.

[104] T. Lind, Z. Li, R. Rajasegar, G. Roberts, Ö. Andersson and M. P. Musculus, "Diffuse back-illumination temperature imaging (DBI-TI), a novel soot thermometry

technique," *Combustion and Flame,* vol. 240, no. 111949, pp. 1-12, 2022.

[105] T. Lo, M. Sciemann, K. Jan, A. Dreizler and B. Böhm, "Experimental investigations of single particle and particle group combustion in a laminar flow reactor using simultaneous volumetric OH-LIF imaging and diffuse backlight-illumination," *Renewable and Sustainable Energy Reviews,* vol. 136, no. 110377, pp. 1-12, 2021.

[106] T. Li, C. Geschwindner , J. Köser, M. Schiemann, A. Dreizler and B. Böhm, "Investigation of the transition from single to group coal particle combustion using high-speed scanning OH-LIF and diffuse backlight-illumination," *Proceedings of the Combustion Institute,* vol. 38, no. 3, pp. 4101-4109, 2021.

[107] T. Tatsumi, S. Maeda, M. Nakata, Y. Kobashi, K. Kuwahara, E. Matsumura and J. Senda, "A Study on the Wall Heat Loss from Diesel Spray Flame (Second Report) - Effect of Pilot Injection on Heat Flux-," *Transactions of Society of Automotive Engineers of Japan,* vol. 48, no. 5, pp. 969-974, 2017.

[108] Y. An, V. Raman, Q. Tang, H. Shi, J. Sim, J. Chang, G. Magnotti and B. Johansson, "Combustion stability study of partially premixed combustion with low-octane fuel at low engine load conditions," *Applied Energy,* vol. 235, pp. 56-67, 2019.

[109] Y. An, Q. Tang, R. Vallinayagam, H. Shi, J. Sim, J. Chang, G. Magnotti and B. Johansson, "Combustion stability study of partially premixed combustion by high - pressure multiple injections with low-octane fuel," *Applied Energy,* vol. 248, pp. 626-639, 2019.

[110] A. Jena, . A. P. Singh and A. K. Agarwal, "Optical and computational investigations of the effect of Spray-Swirl interactions on autoignition and soot formation in a compression ignition engine fuelled by Diesel, dieseline and diesohol," *Applied Energy,* vol. 324, no. 119677, pp. 1-15, 2022.

[111] C. Fan, K. Nishida, Y. Liu, T. Zheng and Y. Sun, "Experimental study on diesel spray combustion and heat transfer characteristics with multiple injection strategies by means of rapid compression and expansion machine," *Journal of the Energy Institute,* vol. 108, no. 101232, pp. 1-8, 2023.

[112] F. Jaliliantabar, B. Ghobadian, A. P. Carlucci , G. Najafi, R. Mamat, A. Ficarella, L. Strafella, A. Santino and S. D. Domenico, "A comprehensive study on the effect of pilot injection, EGR rate, IMEP and biodiesel characteristics on a CRDI diesel engine," *Energy,* vol. 194, no. 116860, 2020.

[113] C. Park and S. Busch, "The influence of pilot injection on high-temperature ignition processes and early flame structure in a high-speed direct injection diesel engine," *International Journal of Engine Research,* vol. 19, no. 6, pp. 668-681, 2017.

[114] A. Torregrosa, A. Broatch, . A. García and . L. Mónico, "Sensitivity of combustion

noise and NOx and soot emissions to pilot injection in PCCI Diesel engines," *Applied Energy,* vol. 104, pp. 149-157, 2013.

[115] S. Moon, J. Gao, Y. Zhang, K. Nishida and Y. Matsumoto, "Ignition and Combustion Characteristics of Wall-Impinging Sprays Injected by Group-Hole Nozzles for Direct-Injection Diesel Engines," in *SAE Tecnical Paper*, 2008.

[116] J. Gao, Y. Matsumoto, M. Namba and K. Nishida, "Group-Hole Nozzle Effects on Mixture Formation and In-cylinder Combustion Processes in Direct-Injection Diesel Engines," in *SAE Technical Paper*, 2007.

[117] H. S. Hadi, C. Fan, A. Takayama, K. Nishida, Y. Ogata and R. Mahmud, "Experimental Study on Diesel Spray Combustion and Wall Heat Transfer with Multiple Fuel Injection Strategies - Results of Rapid Compression and Expansion Machine Experiment-," in *Small Powertrains and Energy Systems Technology Conference*, Minneapolis, Minnesota, 2023.

[118] H. A. Johnson and M. W. Rubesin, "Data book (in Japanese)," in *JSME Heat Transfer*, JSME, 1949.

[119] J. Jeong, S. Sato and H. Kosaka, "Effect of in-cylinder flow on local heat transfer to chamber wall in diesel engine," *Transaction of the JSME (in Japanese),* vol. 85, no. 875, pp. 1-15, 2019.

[120] Y. A. Cengel, "Heat and Mass Transfer," in *A Practical Approach*, Mc Graw Hill, 2006.

[121] S. Fujikawa, M. Nakata, S. Maeda, N. Arai and et al., "Proposal of Wall Heat Transfer Coefficient Applicable to Spray-wall Interaction Process in Diesel Engines," *Trans. Soc. Automot. Eng. Japan,* pp. 1120-1125, 2018.

[122] R. Gordon and J. C. Akfirat, "Data book," in *JSME Heat Transfer*, JSME, 1965.

[123] A. I. EL-Seesy, Z. Kayatas, M. Hawi, H. Kosaka and Z. He, "Combustion and emission characteristics of a rapid compression-expansion machine operated with N-heptanol-methyl oleate biodiesel blends," *Renewable Energy,* vol. 147, no. 1, pp. 2064-2076, 2020.

ACKNOWLEDGEMENTS

This dissertation was completed at the Fluid Engineering Laboratory, Mechanical Engineering Program, Graduate School of Advanced Science and Engineering, Hiroshima University. I am deeply grateful to everyone who assisted me during the preparation of this dissertation.

First and foremost, I would like to extend my deepest gratitude to Professor Yoichi Ogata, my academic supervisor, for his unwavering encouragement, thoughtful guidance, constructive feedback, and invaluable discussions throughout my time in the Fluid Engineering Laboratory.

I also wish to express my heartfelt thanks to Professor Keiya Nishida for the extremely valuable comments, supervises, and helpful suggestions regarding this research. Additionally, I am sincerely appreciative of the dissertation committee members, Professors Akira Miyoshi, Professor Yasuhiro Suzuki, and Professor Yuki Kato.

Special thanks are due to the team at Mazda Co: Mr. Jun Kanzaki, Mr. Makoto Namba, Mr. Sangkyu Kim, and Mr. Daisuke Shimo, for their support with the measurements in this study; to Mr. Atsushi Takayama as my partner for experiment; Dr. Chengyuan Fan and Dr. Rizal Mahmud, for their helps in supervise me; and to the fluid engineering Lab: Mr. Pengua Shi, Mr. Liu Erwei , and the fluid engineering lab members, for their useful discussions and advice.

I would also like to express my appreciation to the Ministry of Education, Japan (Monbukagakusho), for sponsoring my studies by providing a scholarship and covering tuition fees. Additionally, I extend my gratitude to the Institut Teknologi Sepuluh Nopember, Surabaya, Indonesia for their financial and moral support during my time at the Hiroshima University.

Lastly, my deepest gratitude goes to my parents and family, especially to my wife, Adys Aprilia, for her unwavering love, encouragement, and support.